Investigation of Biological Systems Using Synchrotron X-ray Light Sources

by

Matthew J. Kidd

A dissertation submitted in partial fulfillment
of the requirements for the degree of
Doctor of Philosophy
(Chemistry)
in The University of Michigan
2007

Doctoral Committee:

Professor James E. Penner-Hahn, Chair
Professor James Bardwell
Professor Marc J.A. Johnson
Professor Vincent L. Pecoraro

TABLE OF CONTENTS

List of Figures

Figure

List of Tables

Table

Chapter 1

Introduction

Metals in biology

Metal ions play important roles in biological systems. Bulk metal ions like sodium, potassium, magnesium and calcium constitute 1-2% of human body weight, and while trace metals such as iron, selenium, manganese, cobalt, nickel, copper, and zinc each are present in less than 0.005% of body weight, each is required to sustain life [1]. A substantial fraction of proteins contain a metal cofactor, and these metalloproteins play a variety of catalytic and structural roles. These protein-bound cofactors are used as structural motifs, as catalytic active sites in many different enzymes, and as acceptors and donors of electrons in biological redox reactions [2]. The roles of these protein-bound metals has been elucidated by using tools like spectroscopy of isolated metalloproteins and synthesized model compounds, kinetic studies of enzymes with transition metal cofactors, and studies of how metal content of organisms changes under varying conditions of nutrition and genetic factors.

The three transition metals with the most prominent biological roles are zinc, copper and iron. All three of these metals are essential to life in addition to being toxic to the cell in excessive amounts, and so the cell has evolved complex mechanisms

for maintaining sufficient levels of these essential metals while minimizing the exposure the cell to the toxic effects of excess unbound copper, zinc and iron.

Iron and copper are both redox-active transition metals that can participate in electron transfer reactions, and both can catalyze Fenton-type reactions [18]. Thus, if a cell is subjected to excessive amounts of either free iron or copper, oxidative stress in the cell is increased, resulting in damage to DNA and membranes. On the other hand, iron plays an essential role in the cell, serving as a heme cofactor in proteins like catalase and cytochrome P450, and playing an important role in the electron transfer system and other redox reactions in the iron-sulfur clusters of various proteins. Additionally, iron plays a central role in dioxygen storage and transport two of the most-studied metalloproteins, hemoglobin and myoglobin. Copper plays an important role in the active sites of proteins like copper-zinc superoxide dismutase and cytochrome c oxidase, among other proteins. The cell balances the toxicity of these metals against the crucial role they play by tightly controlling iron and copper metabolism *in vivo*. In yeast, for example, copper is delivered to various metalloproteins by metal chaperones like CCS, which delivers copper to copper-zinc superoxide dismutase [3], and ATX1, which delivers copper to secretory vesicle copper transporter CCC2, which in turn delivers copper to the multicopper oxidase Fet3, which is required for high-affinity iron uptake [4]. These copper chaperones bind copper quite tightly, and it is thought by some that little or no free copper is present in the cell under normal conditions [5]. In higher organisms, iron is solubilized by transferrins, which then transport Fe(III) into the cell via transferrin receptors on the surface of the cell, where it is stored by ferritin as an iron oxyhydroxide similar to ferrihydrite [6].

Zinc, unlike copper and iron, has a full d shell and cannot carry out redox chemistry. It is tightly bound to may proteins in the cell, and serves both catalytic and structural roles. In the active site of many enzymes, zinc acts as a Lewis acid, facilitating the hydrolysis of chemical bonds in enzymes like carbonic anhydrase or alcohol dehydrogenase [7]. In active sites where zinc plays a catalytic role, one ligand of the zinc is typically a water molecule, which may be labile, allowing for the binding of the substrate to the zinc, or which may itself be reactive, typically as a nucleophilic hydroxide. In proteins where zinc plays a structural role, on the other hand, there is no water ligand, and the zinc atom plays an important role in stabilizing the structure of the protein. Zinc finger domains, for example, consist of two antiparallel β sheets and an α helix; the zinc ion is crucial in the stability of this type of domain. The zinc ligation in a zinc finger domain is typically two to four cysteines, with the balance of the four ligands to zinc being histidine residues [8]. Some zinc-finger-like proteins contain clusters of two or more zincs.

While zinc is not redox-active and cannot initiate Fenton-type reactions, it is toxic in excess; in yeast, zinc is mildly toxic and begins to retard growth in concentrations in excess of 1 mM [11]. In yeast, zinc is imported by the transmembrane zinc-transporters Zrt1p and Zrt2p [9]. The expression of these zinc transporters is regulated by the free-zinc sensing transcriptional activator Zap1p; when the yeast cell needs additional zinc, triggered by low intracellular zinc concentration, Zap1p induces its own upregulation, as well as that of the zinc transporters Zrt1p and Zrt2p [9,10]. In the cytoplasm, the free zinc is buffered by metallothionein and glutathione, which are thought to serve as sinks for other potentially harmful metal ions like cadmium, lead, and copper. An additional

mechanism that the yeast cell employs to control increased intracellular zinc concentration is to sequester zinc in the vacuole via the zinc transporters Zrc1 and Cot1, which are localized on the vacuolar membrane [11]. Other transporters similar to Zrc1 and Cot1 transport zinc from the cytosol to other cellular compartments [12]. This system of zinc regulation in the cell ensures a sufficient, but not toxic, level of zinc in the cell.

In contrast to these essential metals ions, metals like lead, cadmium, arsenic and mercury do not have an established biological role. In humans, exposure to these metals results in acute illness in cases of sudden heavy exposure, and cancer and other chronic illness in individuals who are exposed to these toxins over a prolonged period of time [13]. For example, cadmium and lead are taken up by the cell by the same transporters as take up copper or zinc, and have been observed to cause both oxidative stress and DNA damage [14,15].

Techniques used in this thesis

X-ray fluorescence microscopy

When an X-ray of sufficient energy to ionize a core electron of an atom is absorbed, the electron will be ejected from the atom, resulting in an empty 1s orbital. An electron from a higher-energy orbital will relax into this core electron hole, and a photon will be emitted with energy equal to the difference between the higher-energy orbital and the 1s orbital. This emitted photon is of a characteristic energy, specific to each element. If a mixed sample of elements is illuminated by X-rays that are energetic enough to ionize the core electrons of each element in the mixture, it is possible to quantitate the amounts of each element by monitoring the characteristic fluorescence of each element.

A typical X-ray fluorescence (XRF) spectrum is shown in Figure 1.1. With XRF microscopy, a brilliant X-ray beam, most commonly from a synchrotron, is focused to a small spot size, and then rastered across the sample. At each pixel, the fluorescence of each element is measured by an energy resolving detector, typically a solid-state germanium or silicon detector. For normalization, the incident X-ray beam is measured using nitrogen-filled ion chambers. A schematic diagram of an XRF microscopy beamline is shown in Figure 1.2

The size of the focused X-ray beam depends on the size of the sample that is being studied. The X-ray beam size can simply be cut down by slits to an appropriate size, but since there is no focusing involved, the flux will be decreased in proportion to the beam size, so this method is limited to a spot size of about 50×50 μm^2, and even then the flux is cut down significantly compared to the full beam. Another method is to use Kirkpatrick-Baez mirrors to focus the beam. By this focusing technique, the spot size is typically 2-10 μm in diameter. This spot size is appropriate for imaging large cells or tissue sections [16]. Focusing the X-ray beam using Kirkpatrick-Baez mirrors does not decrease the flux appreciably, which is unique among focusing methods for XRF microscopy. A microprobe that uses Kirkpatric-Baez mirrors at a beamline with an undulator at a third-generation synchrotron source – like the Advance Photon Source, at which we measured data for this thesis – might have a flux of 10^{13} photons/second. Also, the Kirkpatrick-Baez mirrors are "chromatic," meaning that the focus of the X-rays is independent of X-ray energy. This allows energy scans, allowing for spatially-resolved spectroscopic measurements of the samples. In contrast, Frensel zone plates are capable of focusing X-rays to 150 nm or smaller [17]. Zone plates are circular diffraction

gratings; when the X-ray beam passes through the zone plate, different orders of diffraction are produced, one of which converges to a small spot in the plane of the sample. The other orders of diffraction – which would not focus on the sample, but would rather be defocused – are blocked by an order-sorting aperture, which is a pinhole positioned to only allow though the appropriate order of diffraction. Much of the incident beam is diffracted into unproductive orders of diffraction, and the incident beam must be cut further cut down to the size of the zone plates themselves, which are typically half a millimeter in diameter. These facts result in a substantially lower flux than a microprobe equipped with Kirkpatrick-Baez optics; a typical hard X-ray microprobe equipped with Frensel zone plates has a flux between 10^8-10^9 photons/second, with a spot size ranging from 150-400 nm. This very small spot size provides resolution comparable to that of visible light microscopy, making these beamlines appropriate for imaging even small cells. Additionally, since the distance between the zone plate and the plane of focus changes in proportion to the incident energy, energy scans larger than 30-40 eV are not feasible. In this work, we did XRF microscopy at three beamlines: beamlines 2-ID-D and 2-ID-E, and 18-ID-D at the Advanced Photon Source, Argonne National Laboratory. Beamlines 2-ID-D and 2-ID-E are X-ray microprobes using Frensel Zone plates with spot sizes of 150 nm and 350 nm, respectively. At beamline 18-ID-D we used Kirkpatrick-Baez mirrors to focus the beam, and the spot size used was typically 5-15 μm in diameter.

The limit of the resolution of XRF microscopy is roughly the size of the beam used to illuminate the sample. Thus, in the single-cell images presented in this work, the resolution of the images are between 150-300 nm; this is, as mentioned above,

comparable to the resolution of conventional light microscopy. XRF microscopy images of cells presented in this work are sampled with the frequency slightly smaller than the width of the X-ray beam – for example, if a 300 nm beam was used, 250 nm pixels would be measured. When data of this sort are rendered into an image, it results in a very pixilated-looking image, with cells typically around ten pixels across (Fig. 1.3a). When compared to a visible light micrograph of the same cell (Fig 1.3b), the resolution looks far worse. It is important to recognize that the number of pixels of an image do not determine the resolution of the image if the image is over sampled, as visible light micrographs typically are. The resolution of conventional light microscopy is limited by the wavelength of visible light used, effectively limiting the resolution of the technique to 200 nm. Because it takes no more time or effort to measure pixels 1 nm in width rather than 150 nm, light micrographs of cells are heavily over sampled; it is important to note that much of this over sampling is unnecessary and adds no information to the image. XRF microscopy, on the other hand, requires 2-3 seconds to measure a pixel; since oversampling an XRF microscopy image would waste large amounts of time, images are measured using pixels comparable in size to the fundamental limit of the technique's resolution.

When collecting the data, there are two different ways to record the X-ray fluorescence signal. One is to record an entire XRF spectrum at each pixel, which can later be filtered or fit in order to determine the elemental content at that location in the sample. This method has the advantage of being able to sort out any overlapping of signals by carefully fitting the data. There are two disadvantages to this method of data collection: it takes a short period of time to record the XRF spectrum at each pixel (this

overhead time is typically 0.2-0.5 seconds), and the resulting data files are quite large. While the former can add a significant amount of time to the acquisition of an image, in the days of increasing hard drive size the latter is becoming more and more irrelevant. This is the way that data was collected at beamlines 2-ID-D and 2-ID-E. The way that one can record the X-ray fluorescence signal at each data point is to set single-channel analyzers (SCAs) for each element of interest. This will sum the counts from each SCA, but will not record the entire spectrum. While this is a disadvantage in that it is difficult to correct for overlapping signals and other artifacts, this method has the advantage of speed; there is no overhead time associated with this method, so it is possible to spend only a fraction of a second at each pixel. This is the method of data collection that we used at beamline 18-ID-D.

X-ray absorption spectroscopy

X-ray absorption spectroscopy (XAS) is a useful structural probe to examine the coordination environment of metal sites in metalloproteins and model compounds. As the energy of the incident X-ray beam is scanned across the core electron binding energy of the element being measured, a sudden increase in the absorption coefficient is observed as the incident X-rays become energetic enough to eject the core electron. This increase in absorption is known as the "edge" of the element. A typical XAS spectrum is shown in Figure 1.4. The peak with the highest absorption coefficient (the principal absorption peak) is due to an electron in a 1s orbital being excited to a 4p orbital, and the intensity of the principal absorption peak – and other characteristics of this region of the spectrum – is highly dependent on the coordination of the metal. This region of the XAS spectrum is referred to as X-ray Absorption Near Edge Structure (XANES), and it is

sensitive to the metal's geometry and oxidation state. This XANES region of an XAS spectrum generally refers to the region within about 50 eV of the edge.

After the XANES region ends, the region called the Extended X-ray Absorption Fine Structure (EXAFS) begins. As one can see in Figure 1.4, the main feature in this region above the edge is a series of oscillations. As the incident X-rays become energetic enough to eject a core electron, a photoelectron is generated with energy equal to the difference between the electron's binding energy and the energy of the incident X-ray. This photoelectron is emitted from the absorber of the X-ray, and interacts with other atoms. The photoelectron is backscattered by the surrounding atoms; if the incoming and outgoing photoelectron waves are in phase at that specific energy, then one observes a local maximum in absorption, and if the waves are out of phase, a local minimum will be observed in the spectrum. This is the origin of the oscillations in the EXAFS spectrum, and these oscillations contain information about the arrangement of scatterers around the absorbing atoms. The frequency of the oscillations gives information about the distance between the absorber and scatter atoms, the amplitude of the oscillations give information about the number of scatterer atoms, and the phase and shape of the oscillations give information about the identity of the scatterer atoms. The theoretical underpinnings of these oscillations is well-understood, and the oscillations arising from a single scatterer-absorber pair can be described as a function of the energy of the photoelectron. The excitation energy is converted to the frequency domain (*k* space), using the equation:

$$k=[2m_e(E-E_0)/h^2]^{1/2} \qquad (1.1)$$

Where m_e is the mass of the electron, E_0 is the binding energy of the core electron, and *h* is Planck's constant. The EXAFS oscillations of a single absorber-scatterer pairs can then be explained by the following equation:

$$X(k) = \sum_S \frac{N_S . S_0^2 . f_S(k) . e^{(-2k^2\sigma^2)}}{k . r^2} \sin(2kr + \alpha_S(k)) \quad (1.2)$$

Where χ is the fraction modulation in the X-ray absorption cross section due to the scattering from an absorber-scatterer pair, N is the number of scattering atoms, A(*k*) is the the effective back-scattering amplitude, σ^2 is the Debye-Waller factor, which is a measure of disorder, and R is the absorber-scatterer distance, and $\phi(k)$ is the total phase shift experienced by the photoelectron. If there are more than one type of scatterers that contribute to the EXAFS signal, the signal is given by the sum of all the individual absorber-scatterer interactions.

Overview of this thesis

In this thesis, I have used the above tools to study metals in several biological systems using XRF microscopy and XAS spectroscopy, with the aims of asking specific questions about the systems being studied, in addition to developing methodology which could be applied more broadly in the future by ours and other groups. In chapter two, I examined the budding yeast *Sacchromyces cerevisiae* using XRF microscopy. The primary aim of this chapter was to establish a baseline level of knowledge about the subcellular elemental distribution of yeast grown in normal media, in order to provide a basis of comparison to yeast grown under other conditions. Using fluorescent stains to identify the vacuole and the nucleus, we were able to determine which elements localized

where. We found that phosphorus fluorescence was a reasonable surrogate for the nucleus of the cell. Zinc and iron localized to both the vacuole and the nucleus. Sulfur and potassium typically have smooth distributions, and calcium and manganese localized in the vacuole. These results allow for the examination of if and how these localizations change under varying conditions, such as cadmium treatment described in chapter three.

In chapter three, we examined the effects of cadmium treatment on yeast, in order to better understand the mechanism by which cadmium causes cellular damage. The cadmium-treated yeast showed dramatic localizations of copper in the bud and bud neck. The other elements did not show any significant changes in localization compared to the yeast that had not been exposed to cadmium. While iron and zinc did not change their localizations, they did show a significant increase in concentration. X-ray absorption spectroscopy of zinc in yeast cell paste treated with cadmium shows a shift towards sulfur ligation compared to cell paste that was not treated with cadmium. The dramatic effect that cadmium treatment has on iron concentrations and copper localizations suggest that cadmium indirectly causes cellular damage by increasing the free concentration of these toxic metals.

Chapter 4 uses XRF microscopy to examine human erythrocytes that have been infected with the malaria parasite. These studies were undertaken in order to compare the increase in fluorescence found by zinc-sensitive fluorophore to the amount of zinc found associated with the parasite by XRF microscopy, as well as to simply examine the subcellular distribution of the malaria-infected parasite. Infected erythrocytes were found to accumulate zinc 3-6 fold in excess when compared to uninfected cells. This zinc localization was found to be localized close to, but not overlapping with, the iron

localization of the hemozoin crystal. In addition to the increase in zinc, phosphorus, sulfur and potassium were found to substantially increase, while iron showed a small but likely significant increase upon infection.

In Chapter 5, we examined the zinc and iron distribution in rat brain hippocampus using XRF microscopy and XAS. We found that the distribution of bulk zinc was similar to that determined by zinc-sensitive fluorescent probes, with zinc levels substantially increased in the regions of, and that the iron distribution was localized to the cell bodies of the neurons. Spatially-resolved XAS suggest that the average zinc environment of the histologically-stainable zinc pool is four-coordinate oxygen, with a short Zn-O distance of 1.97 Å.

This is a collaborative work; my role in these projects was mainly measuring and analyzing the X-ray fluorescence microscopy and X-ray absorption data measured at the synchrotrons. In Chapters 2 and 3, Nathan Zahler and Andrea Stoddard of the Fierke lab at the University of Michigan developed the growth protocols for the yeast, in addition to coming to the beamline to assist with the XRF microscopy measurements. In Chapter 4, Janet Wolford of the O'Halloran lab at Northwestern University preformed the zinc-sensing fluorophore measurements on the malaria-infected red blood cells, as well as developing the protocols for growth and isolation of the malaria-infected erythrocytes. In Chapter 5, Janet Wolford dissected the rats and prepared the hippocampus sections for examination by XRF microscopy.

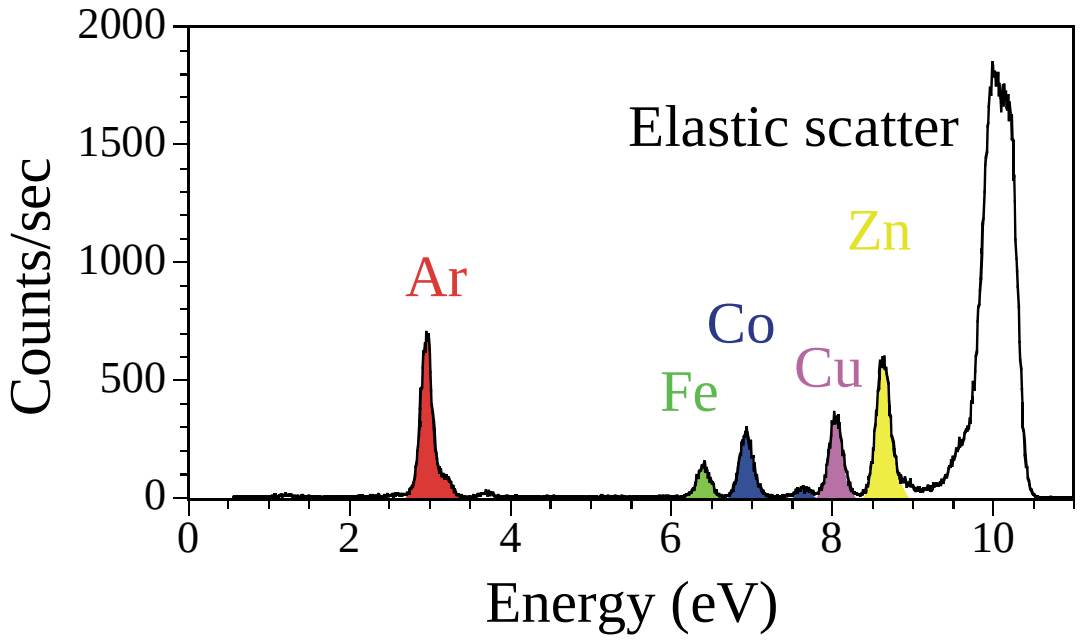

Figure 1.1. Typical X-ray fluorescence spectrum

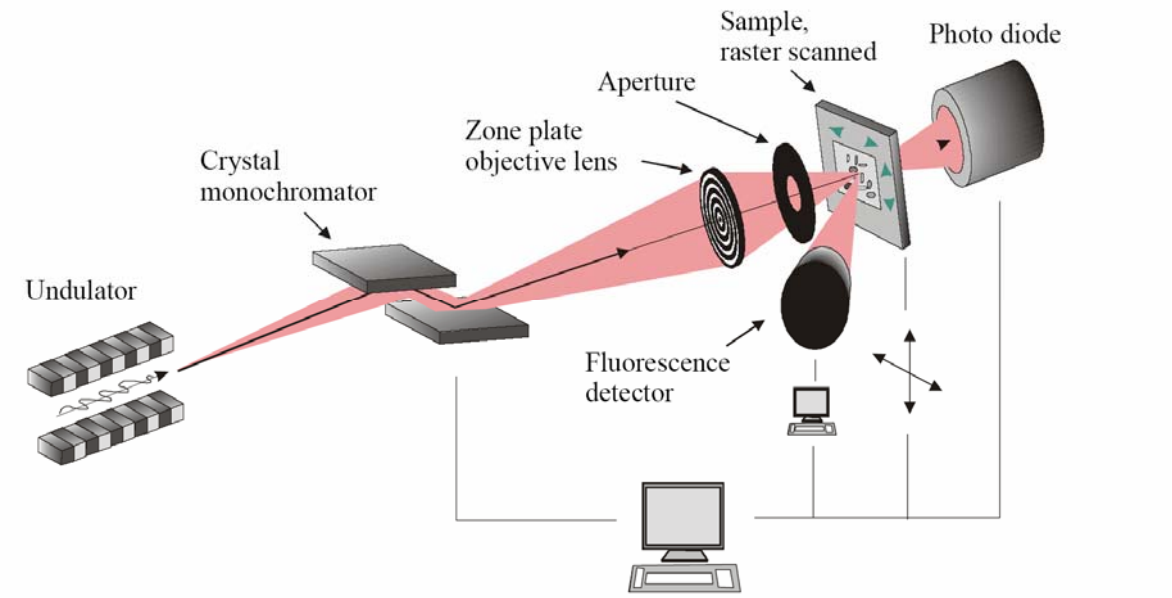

Figure 1.2. Schematic diagram of a typical XRF microprobe beamline

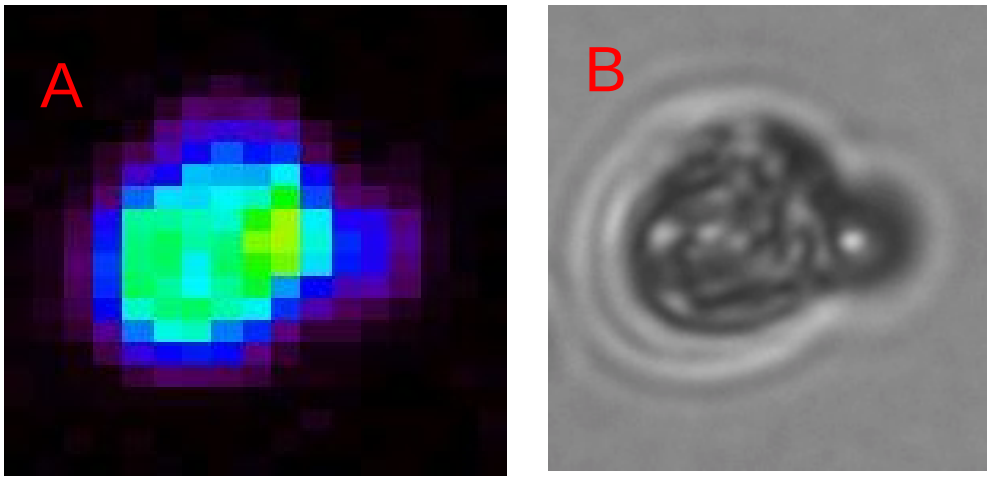

Figure 1.3. Figure 1.3a, left, is an XRF image image of a yeast cell. The pixels in this image are 200 nm in width. Figure 1.3b, right, is a visible light micrograph of the same cell.

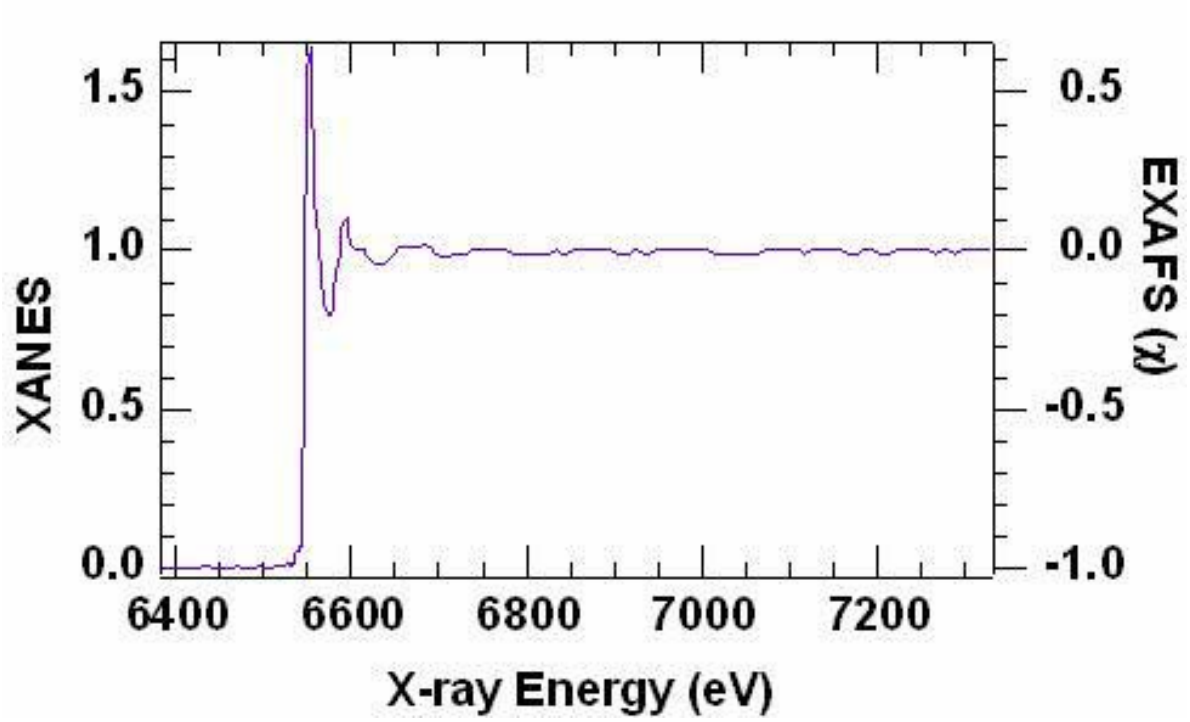

Figure 1.4. Typical X-ray absorption spectrum of the iron K-edge.

References

1. Chang, R. (2007). Chemistry, Ninth Edition. McGraw-Hill
2. Holm, R.H., Kennepohl, P., and Solomon, E.I. (1996). Structural and Functional Aspects of Metal Sites in Biology. Chemical Reviews 96, 2239-2314.
3. Brown, N.M., Torres, A.S., Doan, P.E., and O'Halloran, T.V. (2004). Oxygen and the copper chaperone CCS regulate posttranslational activation of Cu,Zn superoxide dismutase. Proceedings of the National Academy of Sciences of the United States of America 101, 5518-5523.
4. Lin, S.J., Pufahl, R.A., Dancis, A., O'Halloran, T.V., and Culotta, V.C. (1997). A role for the Saccharomyces cerevisiae ATX1 gene in copper trafficking and iron transport. Journal of Biological Chemistry 272, 9215-20.
5. Rae, T.D., Schmidt, P.J., Pufahl, R.A., Culotta, V.C., and O'Halloran, T.V. (1999). Undetectable Intracellular Free Copper: The Requirement of a Copper Chaperone for Superoxide Dismutase. Science 284, 805-808.
6. Dunn, L.L., Rahmanto, Y.S., and Richardson, D.R. (2006). Iron uptake and metabolism in the new millennium. Trends in Cell Biology 17, 94-100.
7. McCall, K.A., Huang, C.C., and fierce, C.A. (2000). Function and mechanism of zinc metalloenzymes. Journal of Nutrition 130, 1437S-1446S.
8. Matthews, J.M., and Sunde, M. (2002). Zinc Fingers – Folds for Many Occasions. IUBMB Life 54, 351-355.
9. Guerinot, M.L., and Eide, D., (1999). Zeroing in on zinc uptake in yeast and plants. Current Opinion in Plant Biology 2, 244-249.
10. Zhao, H., and Eide, D.J. (1997). Zap1p, a metalloregulatory protein involved in zinc-responsive transcriptional regulation in Saccharomyces cerevisiae. Molecular and Cellular Biology 17, 5044-5052.
11. MacDiarmid, C.W., Milanick, M.A., and eide, D.J. (2004). Induction of the ZRC1 metal tolerance gene in zinc-limited yeast confers resistance to zinc shock. Journal of Biological Chemistry 278, 15065-15072.
12. Palmiter, R.D., and Huang, L. (2004). Efflux anc compartmentalization of zinc by members of the SLC30 family of solute carriers. Pfluegers Archiv 447, 744-751.
13. Ibrahim, D., Froberg, B., Wolf, A., and Rusyniak, D.E. (2006). Heavy Metal Poisoning: Clinical Presentations and Pathophysiology. Clinics in Laboratory Medicine 26, 67-97.
14. Jin, T., Lu, J., and Nordberg, M. (1998) Toxicokinetics and biochemistry of cadmium with special emphasis on the role of metallothioneins. Neurotoxicology 19, 529-535.
15. Sharma, R.K., Agrawal, M. (2005). Biological effects of heavy metals: an overview. Journal of Environmental Biology 26, 301-313.
16. Hignette, O., Cloetens, P., Lee. W.K., Ludwig, W., and Rostaing, G. (2004). Hard X-ray microscopy with reflecting mirror status and perspectives of the ESRF technology. Journal de Physique IV 104, 231-234.
17. Twinning, B.S., Baines, S.B., Fisher, N.S., Jacobsen, C., and Maser, J. (2003). Quantification and localization of trace metals in natural plankton cells using a

synchrotron X-ray fluorescence microprobe. Journal de Physique IV 104, 435-438.
18. Urbanski, N.K., and Beresewicz, A. (2000). "Generation of ·OH initiated by interaction of Fe^{2+} and Cu^{+} with dioxygen; comparison with the Fenton chemistry." Acta Biochimica Polonica 47, 951-962.

Chapter 2

Determination of metal distributions in yeast using X-ray Fluorescence microscopy

Introduction

Living cells are composed of 20 different chemical elements; the bulk of the dry weight of a typical organism consists of organic matter composed of H, C, N, and O. Typical concentrations of mineral elements such as Na, Mg, P, S, K, Cl, and Ca are parts per thousand, and micronutrients such as Fe, Co, Cu, Zn, I, F, Mn, and Se each make up less than 0.05% of the dry weight of the cell [1]. The intracellular localization and compartmentalization of these mineral elements and micronutrients, and how they change under varying conditions, is of interest because such changes can give insight into how the cell changes its chemical composition in response to a changing environment. These insights may provide a launching point for the development of an entirely new set of tools for examining yeast metal homeostasis.

The budding yeast *Saccharomyces cerevisiae* is one of the most heavily-studied organisms; the fact that it is so well-characterized makes it an attractive candidate for study of metal distributions. The yeast genome has been published for over a decade, and overexpression and deletion libraries – consisting of roughly 6 thousand yeast

strains that span the entire genome – are commercially available, making examination of the role of various genes in metal homeostasis easier for yeast than for other organisms which do not have such libraries.

Eide and coworkers have recently examined the yeast "ionome," monitoring by inductively coupled plasma atomic emission spectroscopy (ICP-AES, which incinerates samples and thus excites characteristic fluorescence lines, allowing for the quantization of various elements) how the levels of Ca, Co, Cu, Fe, Mg, Mn, Ni, P, K, Se, Na, S, and Zn change for each of 4,000 different yeast mutants, each of which has a single gene deletion [2]. This study showed that deletion of 212 yeast genes caused reproducible effects on the levels in these minerals when the yeast were grown in rich media; most of these genes were involved in vacuolar or mitochondrial functions. While a similar study by XRF microscopy cannot hope to examine the same quantity of conditions that Eide's study covered as I discuss below, it can provide information that bulk methods cannot access.

Methods like ICP-MS and ICP-AES are able to rapidly quantify changes of the mineral composition of cells: both methods have good detection limits and a dynamic range that makes quantifying elements in biological samples fast and easy [3]. While ICP-MS and ICP-AES can determine the average mineral composition of millions of cells in a matter of minutes, XRF microscopy requires about an hour to quantify the elemental content of a single cell. Given that bulk methods allow for the accurate and rapid quantification of the average elemental content of a population of cells, why would one want to take the time and expense of quantifying the cellular content of yeast with XRF fluorescence?

There are several reasons to undertake such a study. Firstly, since XRF microscopy examines the elemental content of a population one cell at a time, one is able to gather information about the standard deviation of a population, rather than just the mean. This information could, for example, give information about how tightly an organism controls a given element – if the cellular Zn concentration of a population was found to have a larger standard deviation than, say, Cu or Fe, it would be evidence that the cell can tolerate a wider range of concentrations of Zn. Since bulk methods do not have the sensitivity to measure samples consisting of a single cell, XRF microscopy is the only way to gather such information.

XRF microscopy has not yet been used for the purpose of analyzing the breadth of the distribution of a population of cells. Much interesting information might result from such analysis, in addition to the specific case mentioned above. It could be that single cell elemental analysis could be analogous to single-molecule spectroscopy in that the single component of the population behaves differently than one might expect from examining the more easily-measured mean of the population [19]. For example, two populations could have the same mean as measured by bulk analysis, and would appear to be identical populations. XRF microscopy, however, could distinguish between the three populations – all of which have the same mean – shown in Figure 2.1. The distribution of each population tells a different story: the first shows a population of cells with tightly-regulated distributions, the second shows what could be a biphasic distribution and the third a widely-scattered distribution. Only single-cell analysis can distinguish between these populations, and presently XRF microscopy is the only technique that allows for analysis of the elemental content of single cells.

Finally, the X-ray beam of an X-ray microprobe equipped with Frenzel zone plates is between 150-400 nanometers in diameter [4]; with sub-micron resolution, it is feasible to resolve the nucleus and the vacuole, each of which is typically a bit less than a micron in size [5]. Yeast mitochondria are significantly smaller than the vacuole or the nucleus and are probably not resolvable from the rest of the cell by XRF microscopy using current methods, although this may be possible in the future.

A previous attempt to image single yeast cells by XRF microscopy was made by Ortega and coworkers [6]. They found that P, S, K, Fe, and Zn all had the same, uniform distribution. The microprobe that these researchers used had an X-ray spot size of 1.5 by 3.2 microns; given that the cells they are looking at are between 2-3 microns, it is unsurprising that the distributions do not show subcellular localization of elements – the X-ray beam size is of comparable size to the target. In this study, we are examining cells with a beam of between 150 and 400 nm, which provide resolution comparable to or better than optical microscopy.

In this chapter I have examined yeast cells by XRF microscopy. Cells were grown under normal laboratory conditions in defined synthetic media. Our goal was to determine what sorts of variability are present in such a population, as well as to determine what elements localized to the nucleus and what elements localized to the vacuole. With this information, we will then be able to examine yeast under varying conditions to see how different growth conditions or mutations effect the elemental distribution of yeast.

Experimental

Yeast were grown in a synthetic defined medium [18] to mid-log phase and harvested by filtration. The cells were washed with a calcium chloride solution to remove any ions that might be adventiously-bound to the exterior of the yeast cell, and then washed several times with deionized water. One microliter of the cell suspension was then pipetted onto a 200 nm thick silicon nitride slide. The cells were allowed to settle for several minutes and then were then rapidly plunge-frozen in liquid ethane using a commercially-available plunge freezer (Leica model KF 80). The frozen slides were then lyophilized overnight, slowly bringing the sample to room temperature until the slides were completely dry. Yeast suitable for XRF imaging (cells that were not clumped together and did not appear to have burst were given preference over cells that were grouped together or appeared abnormal) were identified by visible light microscopy. The strain of yeast used expressed GFP-labeled PRC1, a carboxypeptidase which localizes to the vacuole [7]. Prior to freezing, the yeast were stained with 4',6-diamidino-2-phenylindole (DAPI), a fluorescent stain that binds strongly to DNA. Using these two fluorescent probes, we were able to identify the nucleus and vacuole of each cell (Figure 2.2 shows a typical cell).

X-ray fluorescence images were collected at beamlines 2-ID-D and 2-ID-E at the Advance Photon Source at Argonne National Laboratory. The X-ray beam was focused using Frensel zone plates to size were roughly 200 nm^2 at beamline 2-ID-D and 350 nm^2 at beamline 2-ID-E; step sizes were 150 nm and 300 nm, respectively. Incident X-ray energy was 10 keV, and integration time per pixel was typically 2-3 seconds. Fluorescence data were measured using a germanium or silicon solid state detector, and

the x-ray flux was measured before the zone plates, after focusing but before the sample, and after the sample using three nitrogen-filled ion chambers. Samples were mounted in a helium-filled chamber in order to reduce absorption of low-energy fluorescent X-rays by the atmosphere. Data were collected at room temperature.

X-ray fluorescence images were processed with MAPS, a software package written by Stefan Vogt [8]. Using the MAPS software package, a region of interest was drawn around each cell; in budding cells separate regions were defined for the mother cell and the budding cell. Integral XRF spectra were generated and fit using the spectrum for each pixel which was fit with the fitting routine included in the MAPS package; a typical spectrum and fit is shown in Figure 2.3. Elements were quantified by comparing the counts at each pixel to the metal levels in NIST X-ray standards 1832 and 1833, which contain a known amount of element per square centimeter.

Results and Discussion

False color plots for a typical budding and nonbudding yeast cell are shown in Figure 2.4a and 2.4b, respectively. In contrast to previous XRF microprobe measurements using a larger X-ray beam [6], it is clear that the distribution of elements is not homogenous throughout a yeast cell. The elements P, Fe, and Zn in particular seem to have non-uniform distributions. Figures 2.5a, 2.5b, 2.5c, 2.5d, 2.5e, and 2.5f show surface plots of P, S, K, Fe, Zn, and Cu, respectively, as well as visible light micrographs of transmitted light, and an overlay of the GFP fluorescence (green, indicating vacuole) and DAPI fluorescence (blue, indicating nucleus). These plots were prepared by Nathan Zahler.

Figure 2.5a shows a typical localization of phosphorus in a cell; the highest level of phosphorus is in the vacuole; the nucleus shows no increase in the concentration of phosphorus compared to surrounding regions. While one might expect increased levels of P in the nucleus due to the localization of DNA in the chromosomes, the percent dry weight of DNA in yeast is only 0.2%, while the dry weight of RNA is 4.8% [10]. Given this low level of DNA compared to RNA (which should be relatively evenly distributed throughout the cell, mostly in the cell's ribosomes but also in tRNA and mRNA), it is reasonable that the nucleus would contain relatively low amounts of phosphorus. Other phosphorus-containing molecules like ATP and phospholipids should not show any substantial localization, since they should be spread uniformly in the cytosol and cell membrane, respectively. Yeast are known to accumulate polyphosphate in the vacuole; this pool of phosphate can account for as much as 10% of a yeast cell's dry weight [11]. Since it is unlikely that the phosphorus content is due to the abundance of DNA in the nucleus or a localization of RNA or other phosphorus-containing molecules, the most likely candidate for P localization in a yeast cell would be the polyphosphate accumulated in the cell's vacuole. Consistent with this, cells that showed a localized increase in GFP fluorescence typically had colocalized maxima in the phosphorus concentration.

The elemental distribution of sulfur for a typical yeast cell, present in the cell as cysteine, methionine, and homocysteine, is shown in Figure 2.5b. Sulfur typically has an even distribution in yeast cells, without significant localizations to either the nucleus or vacuole. Figure 2.5c shows a similar distribution for potassium; both results are consistent with expectations. The only localizations one might expect for sulfur would be

due to membrane proteins, mitochondrial proteins, or nuclear proteins; it is not surprising that all none of these local concentrations is high enough above or below the cell average to have a significant effect on bulk distribution. Potassium's even distribution can be easily explained, since its role in the cell is one of charge balance.

As Figures 2.5d and 2.5e illustrate, iron and zinc show localization to both the vacuole and the nucleus. The yeast vacuole has been shown to store zinc under a variety of conditions, including both zinc-limiting and zinc abundant conditions [12, 13]. Iron's localization in the yeast vacuole is less well established; yeast have not been shown to hyperaccumulate iron in the same manner as zinc, but there is evidence for the vacuole having a role in iron metabolism [14]. The abundance of zinc in the nucleus is not surprising, given the common appearance of zinc finger motifs present in many nuclear transcription factors. The localization of iron in the nucleus is surprising. Iron's role in the cell is typically electron transfer, either in an iron-sulfur cluster or heme motif [15]. Most Fe-S proteins localize to the mitochondria or the cytosol, but a few do localize to the nucleus [16]. It seems unlikely that the relatively few Fe-S proteins found in the nucleus account for such a large pool of iron; either there is some systematic overlap with a region of high iron, such as the mitochondria, or there are unexpected iron proteins in the cell's nucleus.

A typical copper distribution is shown in Figure 2.5f. This is a uniform distribution, much like sulfur or potassium. It should be noted that the average number of counts per pixel is rather low for copper, at 8.3 counts. Assuming a Poisson distribution, we could expect an uncertainty of 2.9 counts for each individual pixel. With such a large uncertainty, it seems unlikely that we would be able to detect even a significant

localization. Iron, on the other hand, has even fewer counts per pixel, at 5.6 counts, and thus an even larger uncertainty in each pixel. Nevertheless, nearly all cells measured, we saw evidence of localization in iron, so it seems probable that we would be able to measure a similarly inhomogeneous distribution for copper. This observed iron inhomogeneity can be reconciled with the low counting statistics by recognizing that the areas of higher iron are 6-8 pixels in area. While the uncertainty in a single pixel might by 40%, the uncertainty in the whole region of seven pixels would be 15%. Thus, we can be reasonably confident that no significant copper localization exists in yeast, within the limits of the resolution of the technique. Given that most copper will be in either SOD1, which should be distributed throughout the cytosol, or in mitochondrial electron transfer-proteins, which may not be able to be resolved by this technique, an even distribution is to be expected.

Table 2.1 shows the average elemental content of the population of yeast in terms of atoms per cell, the percent standard deviations of the population (n=23) for each element, the standard deviation of each element divided by the elastic scatter, and the ratio of these two numbers. The average number of atoms per cell for each element measured is quite close to the values measured by Eide in the “yeast ionome” work discussed above, even though the strain of yeast and growth conditions were quite different. The largest difference was found for zinc, which Eide found to be roughly double our value; this was likely due to our media containing fivefold less zinc [2]. The significance of the statistics compiled in Table 2.1, and how these numbers are calculated warrant some explanation. The average elastic scatter (the photons that interact with the sample but are scattered without losing any energy) is shown in the last column of the

chart. The elastic scatter is proportional to the amount of matter that obstructs the X-ray beam; scatter increases proportionally to both density and atomic number. Given that most of a yeast cell is composed of carbon, oxygen, hydrogen, and nitrogen and that the C:O:N ratio is approximately constant, one can expect the amount of scatter detected to be proportional to the mass of the cell. There could be small variations depending on concentration, but given that C, O, and N have similar scattering cross-sections (and that H has a negligible scattering cross-section), biologically reasonable variations in the C:O:N ratio should have negligible effect on the proportionality between scattering intensity and mass. Although most of the elastic scatter can be attributed to these bulk elements, it is possible that variations in phosphorus composition could slightly affect the apparent density. Phosphorus scatters 10 keV photons 2.3 times as strongly as oxygen [17] and as noted above, can make up ten percent of the dry weight as polyphosphate stored in the vacuole. If one assumes that all of the P is contained in the vacuole and that the vacuole occupies half of the cell volume, then the relative P concentrations are 20% of the mass and 0% of the mass. This would give an apparent thickness that would be $0.8+0.2\times2.3 = 1.26$ higher in the vacuolar region. This is probably an upper limit for the error in apparent thickness within a single cell due to compositional variation. For comparisons of total mass between cells, the uncertainty will be even smaller. Since elastic scatter can be used as a reliable indicator of cell size, we can divide the total number of atoms in a given cell by the cell's scatter, giving a reasonable surrogate of concentration of each element in each portion of the cell, and an even better measure of the average concentration per cell. The associated standard deviations of the total atoms

per cell and the surrogate concentration values can provide interesting information about how much variation in the concentration of specific elements a cell can tolerate.

The standard deviations of the surrogate concentration of the micronutrients potassium, sulfur, and phosphorus show a substantial decrease in variability when cell size is taken into account. This implies a positive correlation of these elementals with cell size. Calcium, iron, copper, and zinc all showed less of a decrease in variability when comparing the surrogate concentrations with the total amounts of metal, implying less of a correlation between amount of metal and cell size. However, as Figure 2.6 shows, all elements have a generally linear correlation with scatter. The larger standard deviation in the surrogate concentration for the transition metals is generally due to a few outliers.

Specifically, there is one outlier for both copper and iron; in both cases, the concentration of metal is about 3 times higher than the average of the populations. While it would obviously be hasty to draw conclusions from such scant data, these outliers may hint at how yeast cells regulate their internal iron and copper concentrations. The high outliers could be cells that recently imported large amounts of copper or iron by upregulating import proteins in response to low levels of intracellular iron or copper. The cell would then quickly upregulate the efflux pumps in order to bring the metal levels to a lower level. This would result in an asymmetrical distribution skewed towards the higher range of concentrations.

Figure 2.7 shows the correlation of various elements with scatter for a typical yeast cell. Like the scatter plots for the whole cells, most elements are correlated with scatter. The plot of phosphorus and scatter is typical for yeast cells; the region of highest

scatter has a slightly lower level of scatter than one would expect given the relationship between scatter and phosphorus in the rest of the cell. Figure 2.8 shows these data points with an anomalous phosphorus/scatter ratio, and their localization within the cell. As can be seen, these points localize in a cohesive group; as discussed above, this localization of high phosphorus localization is likely to be the polyphosphate-rich vacuole. The fact that phosphate-rich regions can be readily identified using such scatter plots can be used to identify the vacuole can be used to track vacuolar content under varying conditions.

Work recently done by Nathan Zahler, Andrea Stoddard, and Gundog Yucesan of the Fierke lab recently demonstrated the value of phosphate as a marker of the vacuole. [unpublished result] They measured XRF images of yeast cells grown under zinc-limited conditions and compared the cells to the population described in this chapter. They found that the zinc-starved yeast seemed to have a higher amount of iron in the nucleus than did the cells grown under zinc-replete conditions. They then expressed and purified nuclear zinc-finger proteins under anaerobic conditions and measured the metal content of the purified proteins. Surprisingly, several of the "zinc finger" proteins bound stochiometric amounts of iron, which suggests that these proteins could use zinc or iron interchangeably, depending on the conditions the cell faces. Similar XRF microscopy studies examining how elemental localizations change under various conditions done in yeast or other organisms might yield equally important insights on these systems.

While the significance of the elemental localization to subcellular compartments is more easily justified, future work will have to be done in order to demonstrate that important information is contained in the distributions of the populations themselves. For example, in order to test the hypothesis described above where the population of yeast

might have an asymmetrical distribution skewed towards the higher concentrations, far more cells would have to be measured than the 25 or so measured in this work. It is important to note that quantifying the elemental content of only 25 images of cells is a major effort that uses several days of scarce instrument time. It would be impossible to get an accurate picture of the distribution using XRF microscopy as described in this technique – in order to do so, the experiment would have to be modified in one of two ways.

First, the amount of time spent measuring each cell could be reduced. Generally, it takes about an hour and a half to locate and measure the image of each cell. If resolution is sacrificed for the sake of speed, accurate quantification of each cell could be done in as little as 30 minutes per cell. However, given that the dataneeded to accurately describe the population's distribution is likely roughly 10-100 times the 25 cells measured, a threefold increase in speed is not likely to be a sufficient increase in throughput. The other method, which would allow for the analysis of many more cells, would involve coupling a flow cytometer or similar device to an X-ray microprobe. Flow cytometers are capable of organizing a stream of single cells that are passed in front of a laser, which stimulates a fluorophore, the fluorescence of which is quantified by a detector [20]. The cells can then be sorted based on the intensity of the fluorescence and then further analyzed; these machines can sort thousands of cells per second. While such a project would be difficult and expensive, if a flow cytometer could be coupled to an XRF microprobe, then distributions of populations could then be quickly analyzed. If successful, this would provide a means to quickly and thoroughly examine the

distribution of populations of cells, which would allow for many experiments to be done examining how these distributions change with cell cycle or growth conditions.

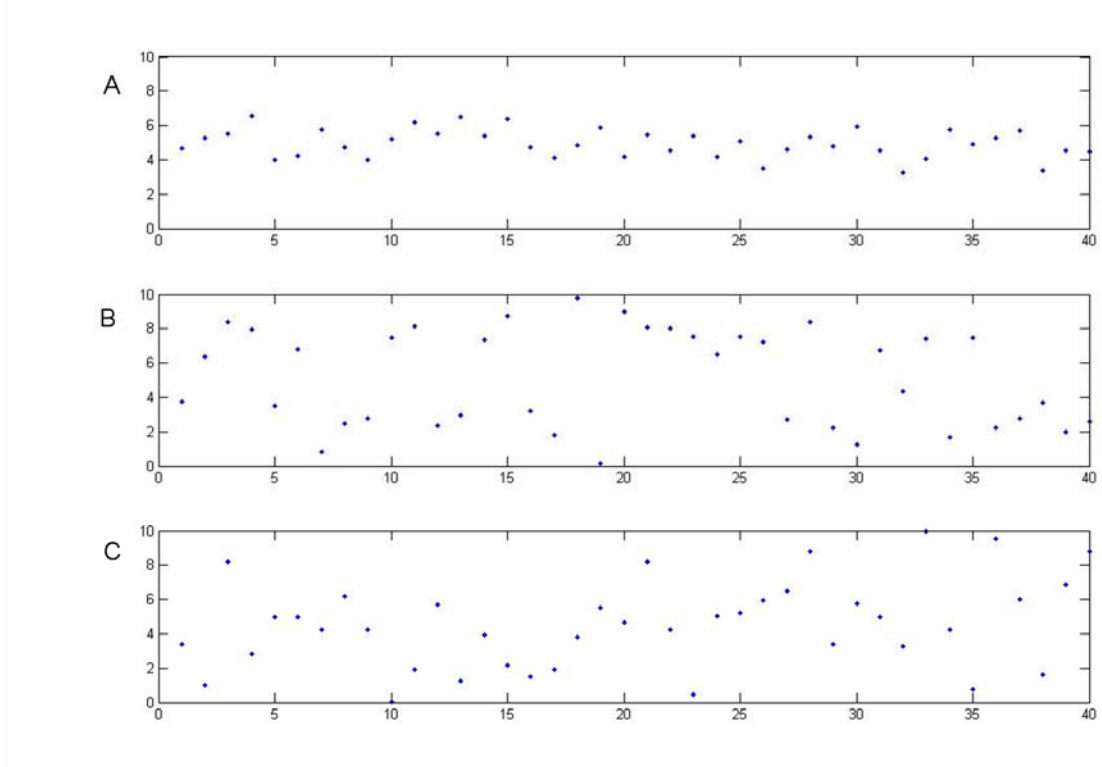

Figure 2.1. Hypothetical data, all with the same mean, but with very different distributions

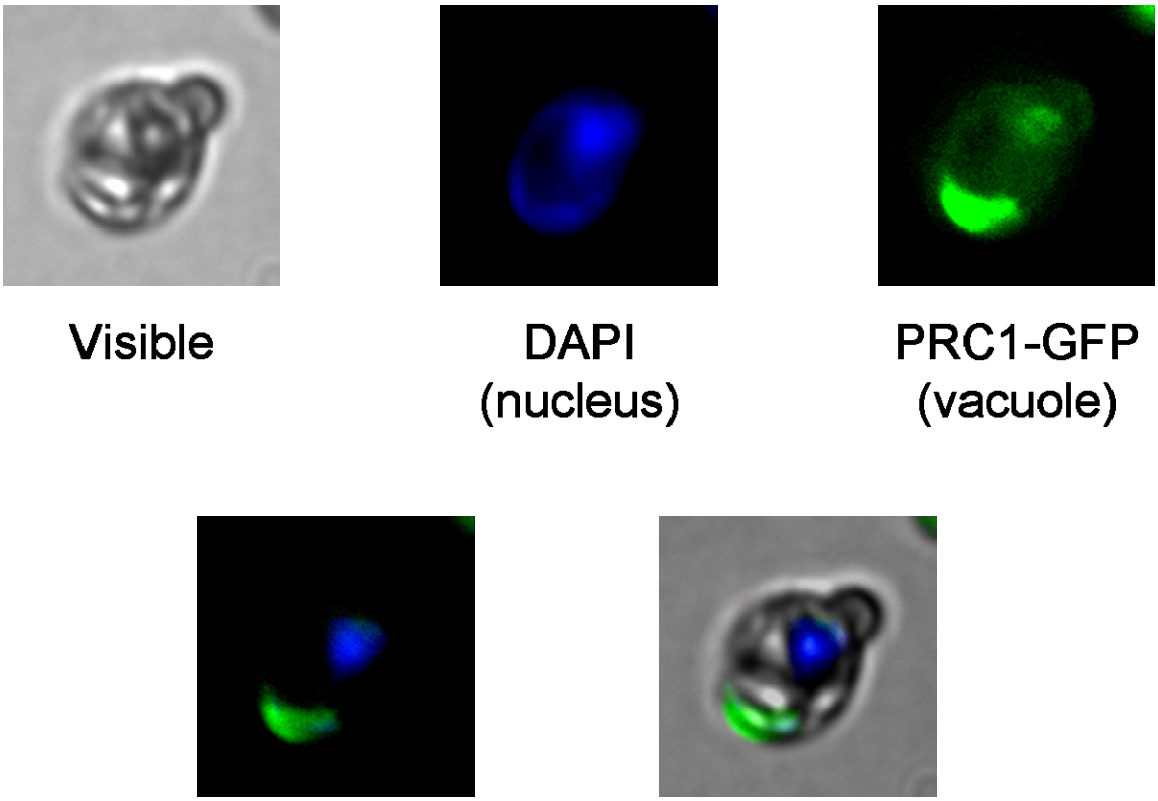

Figure 2.2. Visible light micrographs of a typical yeast cell. The blue DAPI stains mark the nucleus and the green GFP fluorescence marks the vacuole. The overlays of these images clearly show the localizations of vacuole and nucleus in this cell

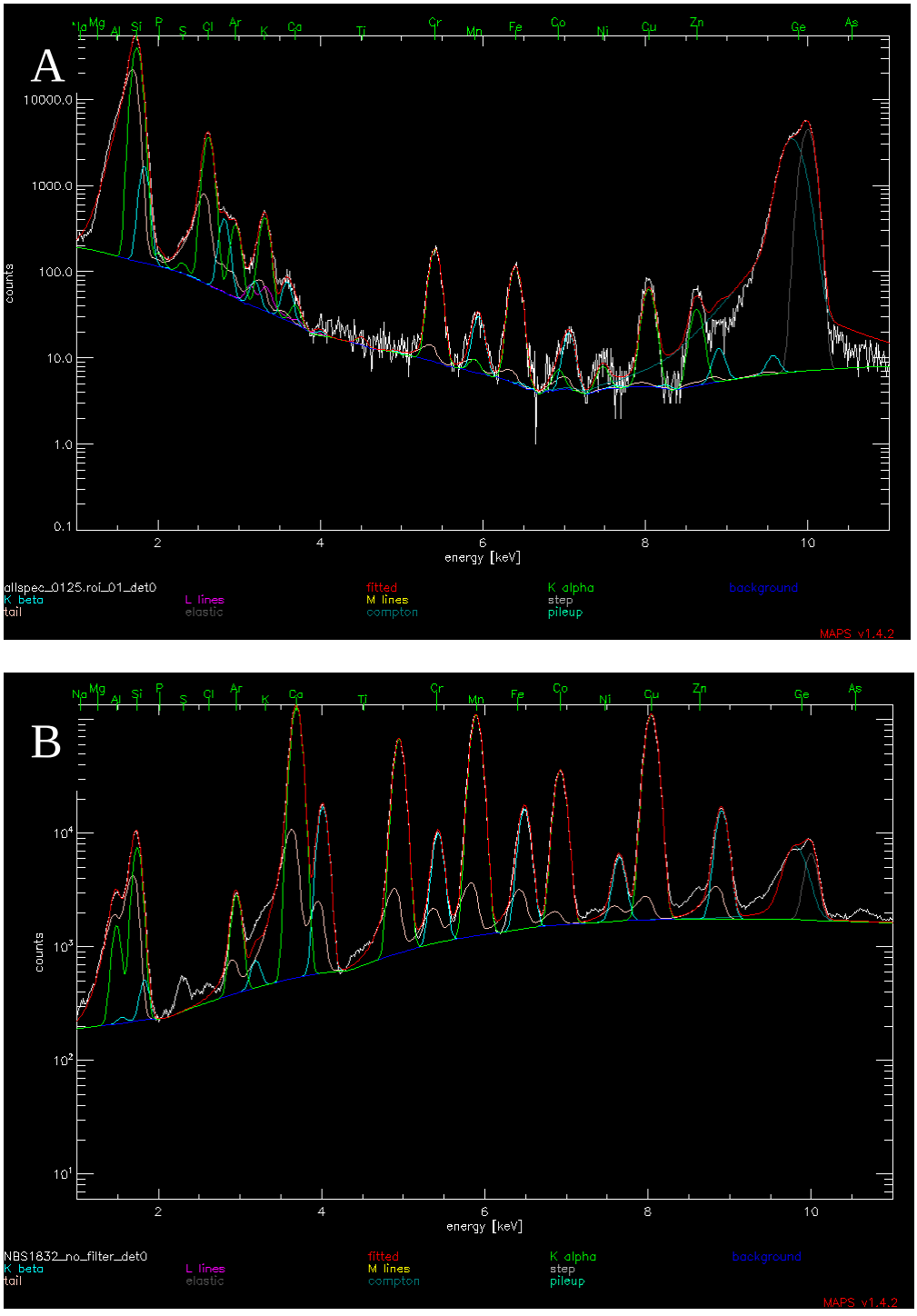

Figure 2.3. Figure 2.3a, top, shows the typical XRF spectrum and fit of the sum of all the pixels of a cell. Figure 2.3b, bottom, is a typical spectrum of NIST XRF standard 1832.

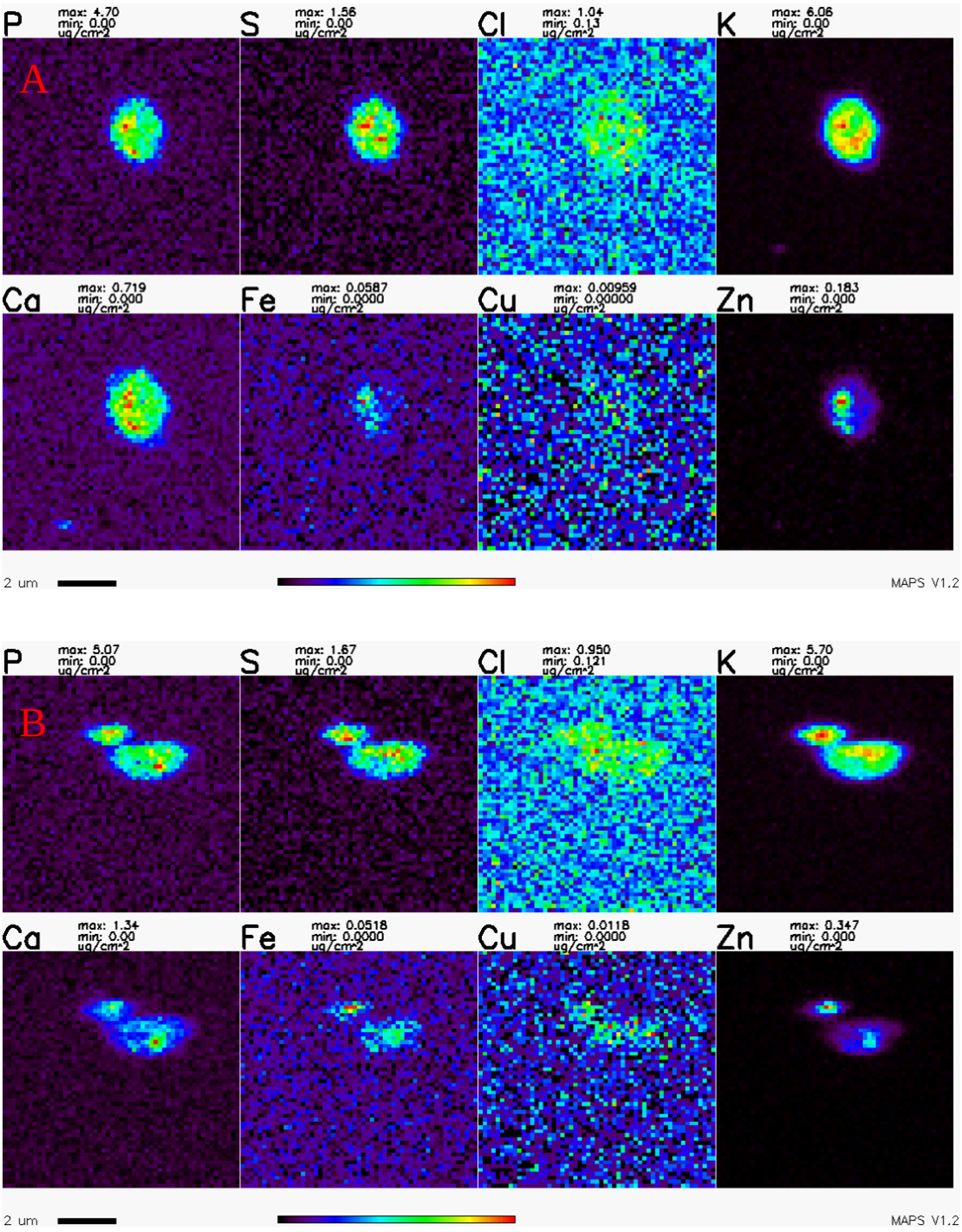

Figure 2.4. Figure 2.4a, top, shows a false-color plot of an XRF micrograph of typical yeast cell. Figure 2.4b, bottom, is a false-color plot of a typical budding yeast.

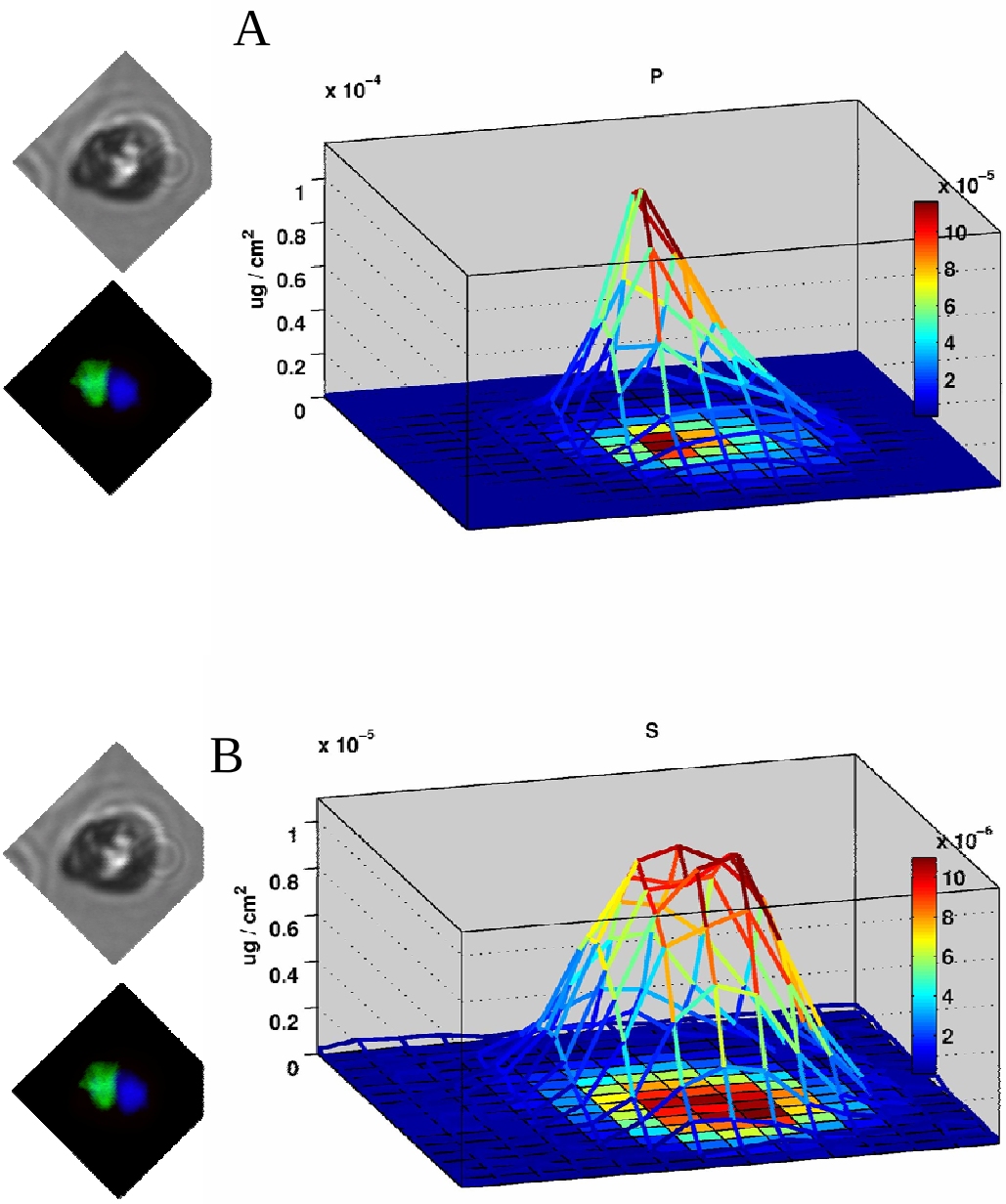

Figure 2.5. Figure 2.5a, top, shows the typical phosphorous distribution of a yeast cell, as determined by XRF microscopy. Figure 2.5b, bottom, shows the sulfur distribution of a yeast cell. The images alongside the cell are the DAPI/GFP overlays indicating vacuole and nucleus localization (blue for nucleus, green for vacuole)

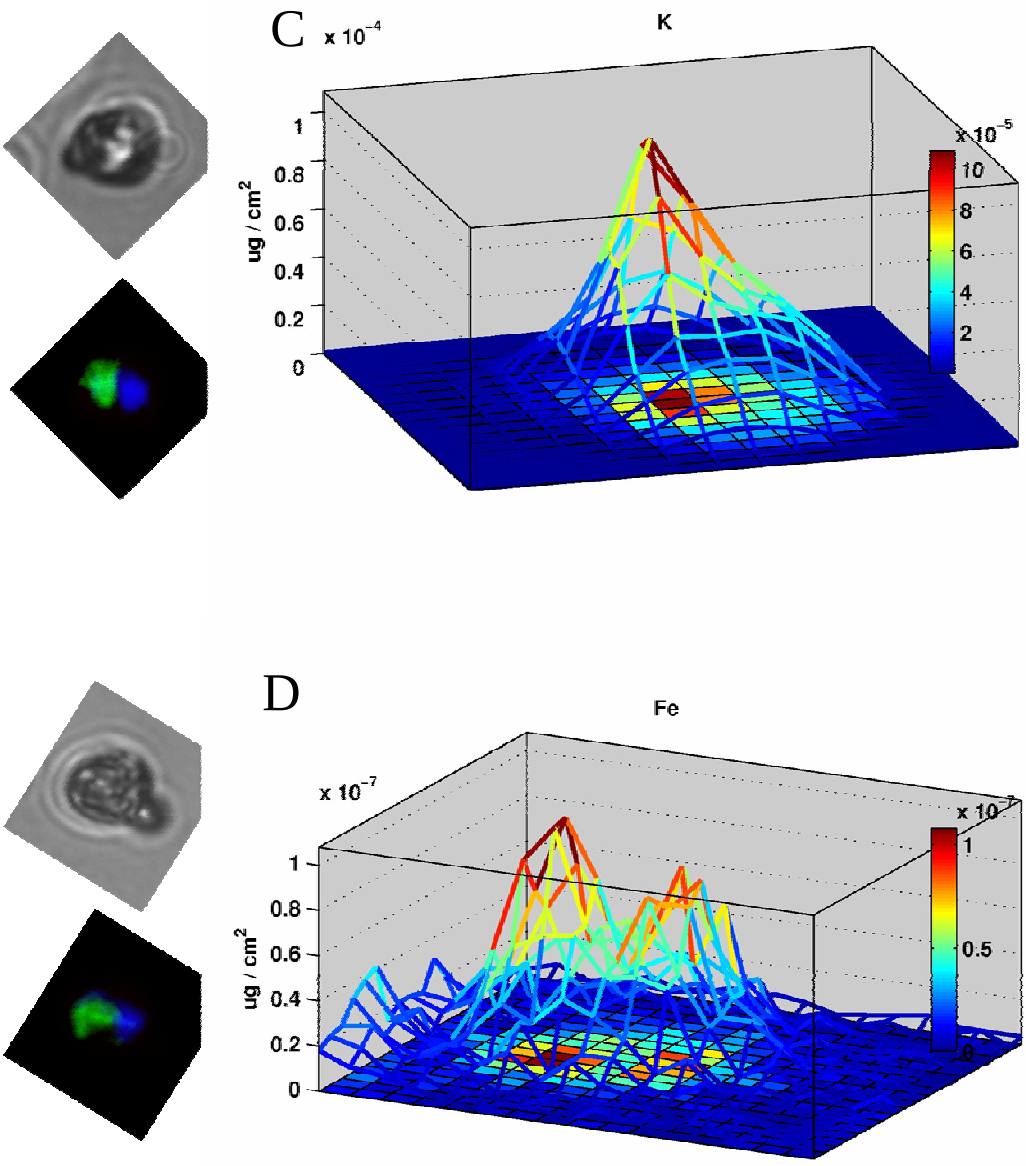

Figure 2.5 (cont). Figure 2.5c, top, shows the potassium distribution of a yeast cell, 2.5d, bottom, shows the iron distribution.

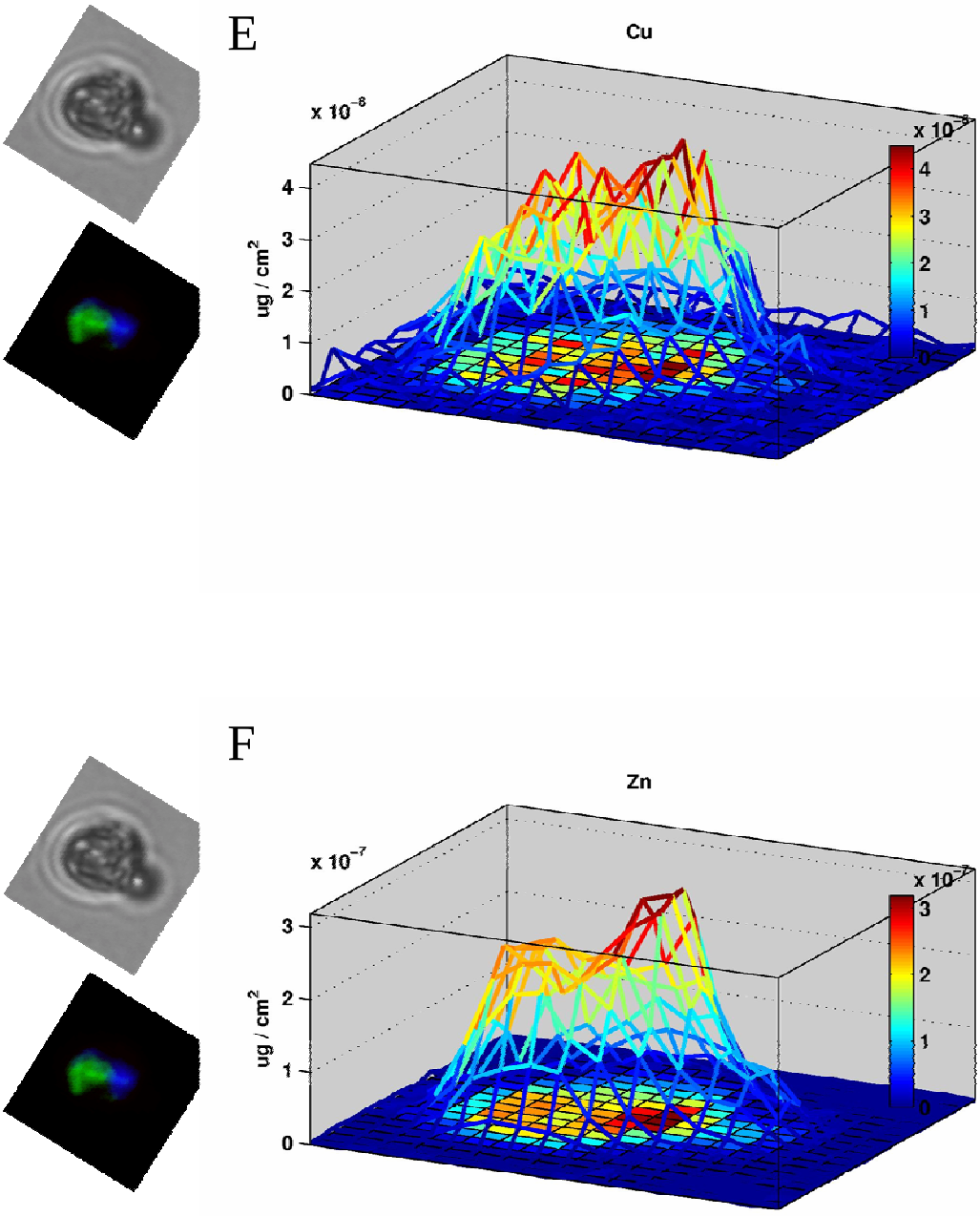

Figure 2.5 (cont). Figure 2.5e, top shows the copper distribution of copper in a typical yeast cell, while Figure 2.5f show the distribution of zinc in a typical yeast.

Table 2.1. Average number of atoms per cell, as measured by XRF microscopy, and the associated standard deviations. These statistics were calculated based on a sample of 23 yeast cells.

	Atoms per cell (counts for scatter)	Standard deviation	Percent standard deviation	Surrogate concentration standard deviation	ratio
P	3.6E+09	1.6E+09	0.44	0.22	0.51
S	1.1E+09	3.6E+08	0.33	0.21	0.65
K	4.3E+09	1.6E+09	0.36	0.19	0.52
Ca	2.2E+08	9.6E+07	0.45	0.41	0.91
Mn	2.2E+06	1.0E+06	0.46	0.37	0.80
Fe	2.0E+06	9.4E+05	0.49	0.39	0.85
Cu	1.8E+06	8.6E+05	0.34	0.47	0.96
Zn	1.3E+07	4.3E+06	0.34	0.23	0.67
scatter	1.3E+04	4.5E+03	0.33		

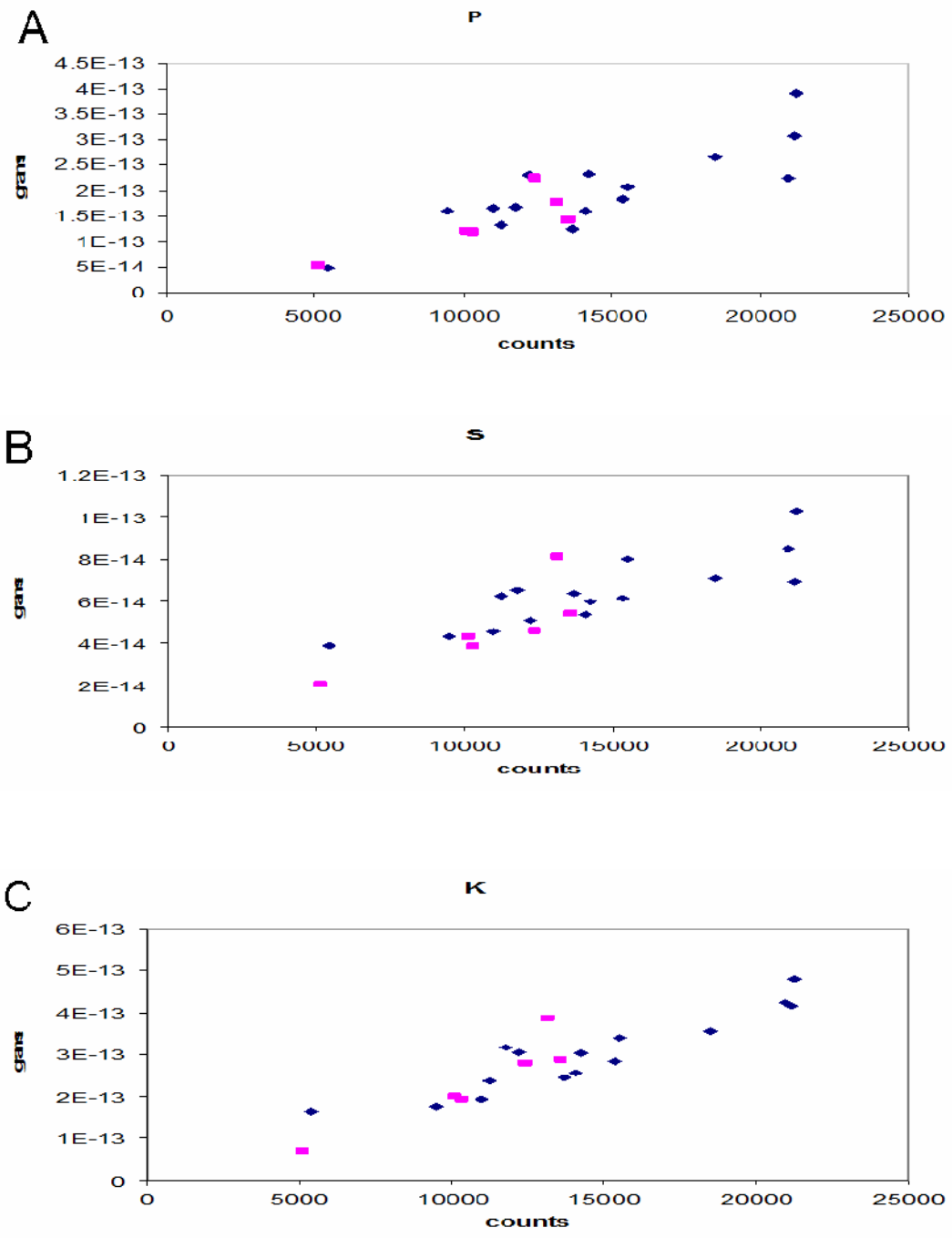

Figure 2.6. Scatter plots of the total elemental content versus the total scatter for all yeast measured by XRF microscopy. Figure 2.6a is a plot of phosphorous, 2.6b plots sulfur, and 2.6c plots potassium. The uncertainty in each data point is less than 2 percent for all three elements. The uncertainty in scatter is less than 2 percent. The y axis is the total elemental content of the cell in grams, and the x axis is the total elastic scatter of measured for the cell. Both elemental content and scatter have been background subtracted. Blue data points are budding yeast, pink are yeast with no apparent bud.

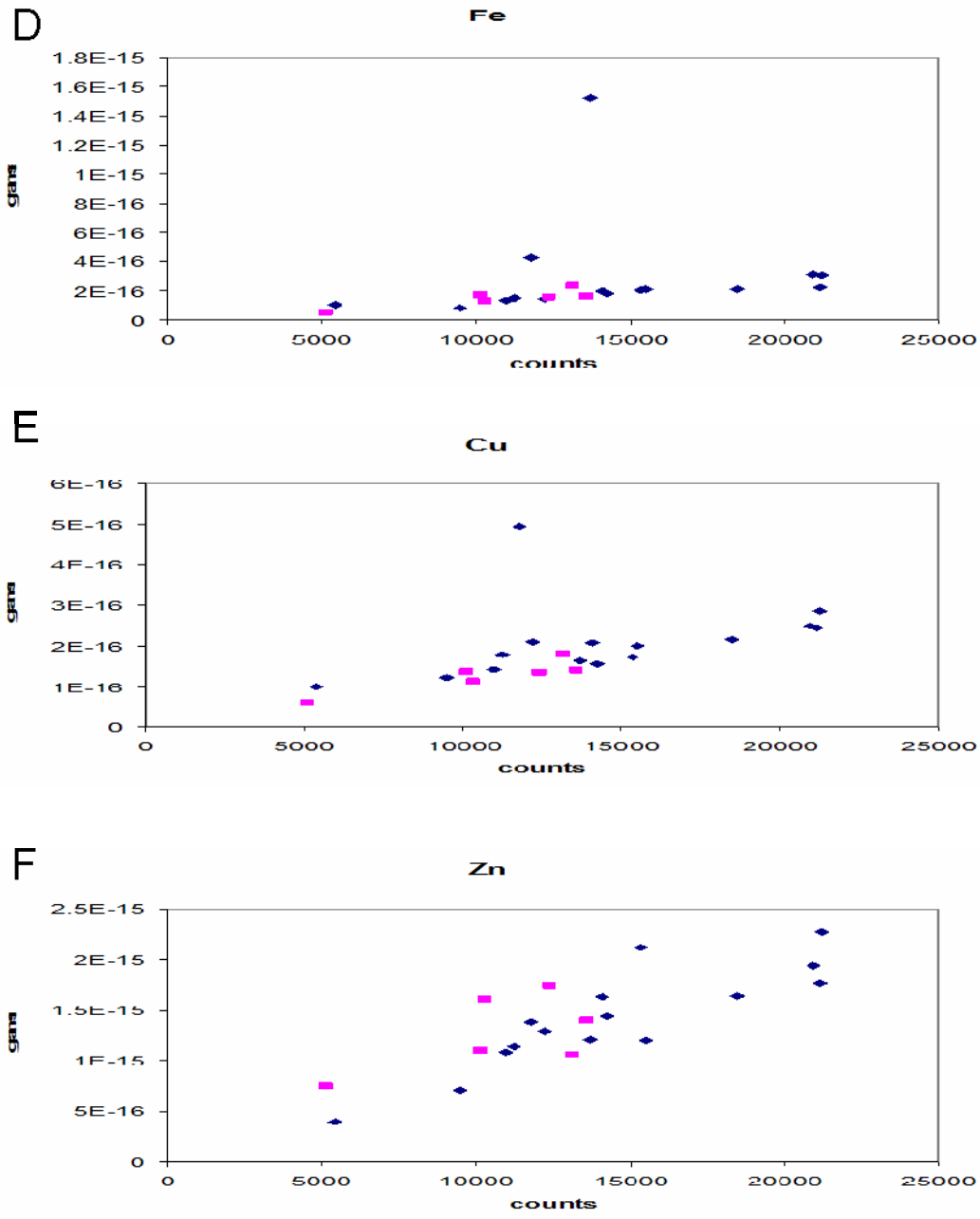

Figure 2.6 (cont). Scatter plots of the total elemental content versus the total scatter for all yeast measured by XRF microscopy. Figure 2.6d is a plot of iron, 2.6e plots copper, and 2.6c plots zinc. The uncertainty in each iron and copper data point is ~5-6%; the uncertainty in zinc is ~3%. The uncertainty in scatter is less than 2% for each point. The y axis is the total elemental content of the cell in grams, and the x axis is the total elastic scatter of measured for the cell. Both elemental content and scatter have been background subtracted. Blue data points are budding yeast, pink are yeast with no apparent bud.

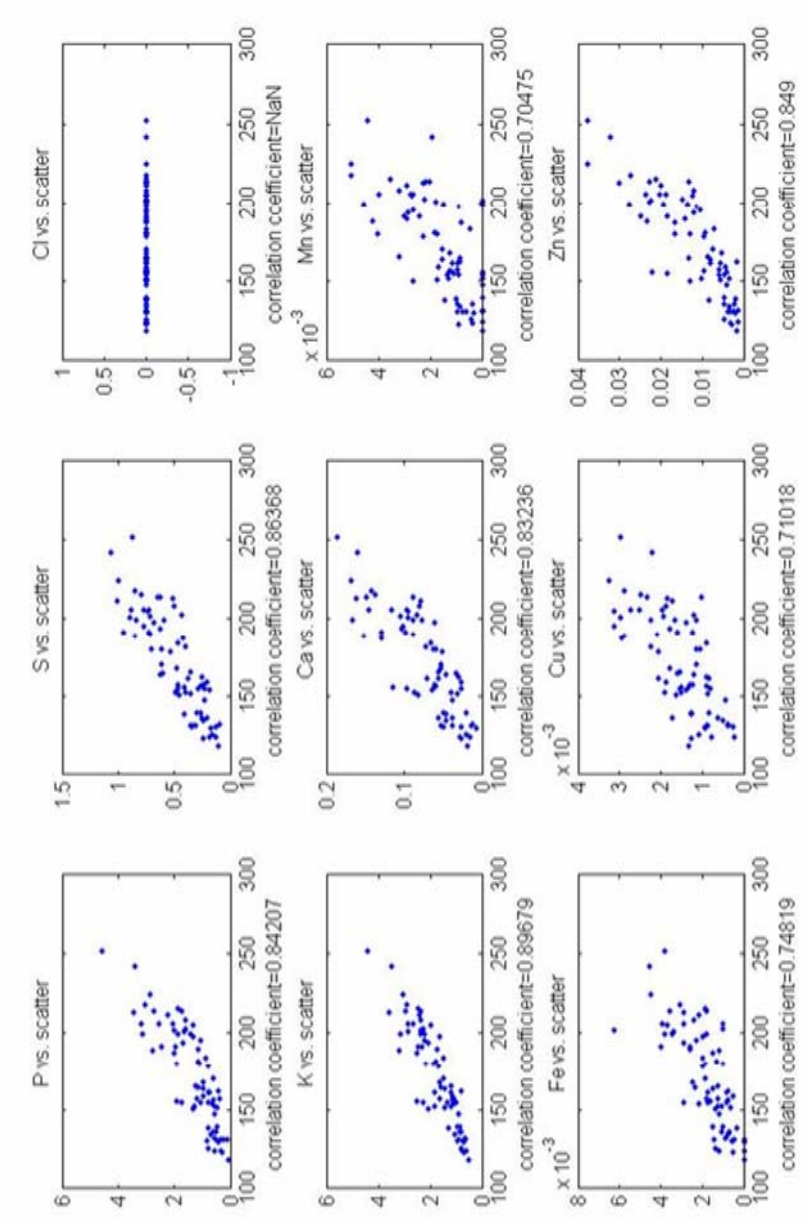

Figure 2.7. This is a tyical scatter plot of each individual pixel of a yeast cell versus scatter. The x axis is the scatter, in counts, and the y axis is the elemental fluorescence, calibrated to μg/cm^2 using NIST standards. The uncertainty of the scatter in each point ranges from 6-10%. The elemental uncertainty of each point for the elements ranges from ~30% for iron and copper to ~5% for potassium.

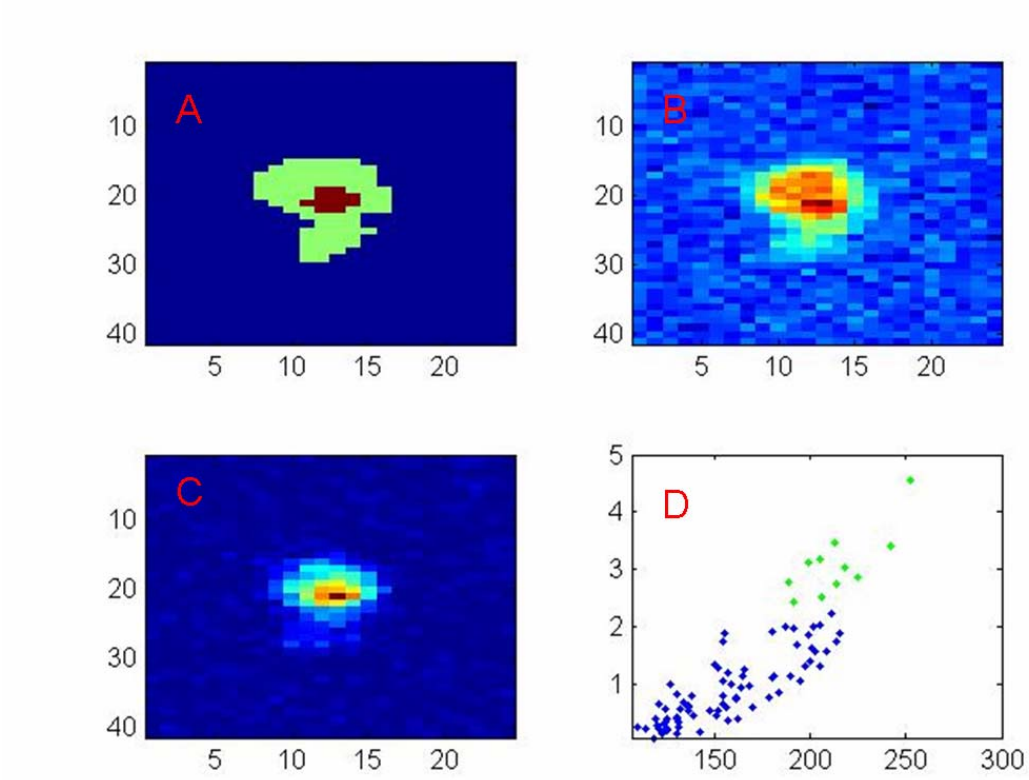

Figure 2.8. The cell depicted in this figure is a typical budding yeast. 2.6b is a false-color image of elastic scatter, while 2.6c is an false-color image of phosphorous. 2.6a shows two regions of interest, the smaller of which is the area of high phosphorous, and the other is the remainder of the cell. 2.6d is a scatter plot of phosphorus on the y axis, in units of $\mu g/cm^2$, and scatter, in units of counts, on the x axis.

References

1. Campbell, M.K., and Farrel, S.O. (2006). Biochemistry. Thompson Brooks.
2. Eide, D.J., Clark, S., Nair, T.M., Gehl, M., Gribskov, M., Guerinot, M.L., and Harper, J.F. (2005). Characterization of the yeast ionome: a genome-wide analysis of nutrient mineral and trace element homeostasis in Saccharomyces cerevisiae. Genome Biology 6, art no. R77.
3. Komarmy-Hiller G. (1999) Flame, flameless, and plasma spectroscopy. Analytical Chemistry 71, 338R-342R.
4. Twinning, B.S., Baines, S.B., Fisher, N.S., Maser, J., Vogt, S., Jacobsen, C., Tovar-Sanchez, T. and Sanudo-Wilhelmy, S.A. (2003). Quantifying trace elements in individual aquatic protest cells with a synchrotron x-ray fluorescence microprobe. Analytical Chemistry 75, 3806-3816.
5. Shapiron, D., Thibault, P., Beetz, T., and Sayre, D. (2005). Biological imaging by soft x-ray diffraction microscopy. *PNAS* 102 ,15343-6
6. Ortega, R., Bohic, S., Tucoulou, R., Somogyi, A., and Deves, G. (2004). Michrochemical Element Imaging of Yeast and Human Cells Using Synchrotron X-ray Microprobe with Kirkpatrick-Baes Optics. Analytical Chemistry 76, 309-314.
7. Van Den Hazel, H.B., Keilland-Brandt, M.C., and Winther, J.R. (1996). Review: biosynthesis and function of yeast vacuolar proteases. Yeast 12, 1-16.
8. Vogt, S. (2003). MAPS: a set of software tools for analysis and visualization of 3D X-ray fluorescence data sets. Journal de Physique IV 104, 635-638.
9. Waters, B.M., and Eide, D.J. (2002). Combinatorial control of yeast FET4 gene expression by iron, zinc and oxygen. Journal of Biological Chemistry 277, 33749-33757.
10. Polakis, E.S., and Bartley, W. (1966). Changes in dry, weight protein, ribonucleic acid, deoxyribonucleic acid, and reserve and structural charbohydrate during aerobic growth cycle of yeast. Biochemical Journal 98, 883-886.
11. Beeler, T., Bruce, K., and Dunn, T. (1997). Regulation of cellular Mg2+ by Saccharomyces cerevisiae. Biochimica et Biophysica Acta-Biomembranes. 1323,310-318.
12. Ramsay, L.M, and Gadd, G.M. (1997). Mutants of Saccharomyces cerevisiae defective in vacuolar function confirm a role for the vacuole in toxic metal ion detoxification. FEMS Microbiology Letters 152, 293-298.
13. MacDiarmid, C.W., Milanick, M.A., and Eide, D.J. (2002). Biochemical properties of vacuolar zinc transport systems of Saccharomyces cerevisiae. Journal of Biological Chemistry 277, 39187-39194.
14. Li, L., Chen, O. S., Ward, D., and Kaplan, J. (2001). "CCC1 Is a Transporter That Mediates Vacuolar Iron Storage in Yeast." Journal of Biological Chemistry, 276 29515-29519.
15. Holm, R.H., Kennepohl, P., Solomon, E. (1996). Structural and functional aspects of metal sites in biology. Chemical Reviews 96 2239-2314.
16. Lill, R., Dutkiewicz, R., Elsasser, H.P., Hausmann, A., Netz, D., Pierik, A., Stehling, O., Urzica, E., Muhlenhoff, U. (2006). Mechanisms of iron-sulfur

protein maturation in mitochondria, cytosol, and nucleus of eukaryotes. Biochimica et Biophysica Acta 1763, 652-667
17. McMaster, W.H., Kerr Del Grande, N., Mallett, J.H., and Hubbel, J.H. (1969). Compilation of X-ray Cross Sections. N.B.O. Standards, Editor. Lawrence Livermore National Laboratory: Livermore, CA.
18. Gitan, R.S., Luo, H., Rodger, J., Broderius, M., and Eide, D. (1998). Zinc-induced Inactivation of the Yeast ZRT1 Zinc Transporter Occurs through Endocytosis and Vacuolar Degradation. The Journal of Biological Chemistry 44, 28617-28624.
19. Xie, X., Lu, H. (1999). Single-Molecule Enzymology. Journal of Biological Chemistry 274, 15967.
20. Melamed, M.R., Lindmo, T., and Mendelsohn, M.L. (1990). Flow Cytometry and Sorting.

Chapter 3

Determination of Effects of Cadmium Toxicity on Yeast by X-ray Fluorescence Microscopy

Introduction

Cadmium toxicity in humans was first described in Japan in 1955, as a result of run-off from a zinc mine contaminating a river and affecting those living downstream [1]. Currently, cadmium is released into the environment due to mining, metallurgy, and industrial use in the production of nickel-cadmium batteries, pigments, plastic stabilizers and anti-corrosive products [1]. Human exposure to cadmium is primarily due to cigarette smoking, since tobacco plants – like other plants – accumulate cadmium when it is found in the surrounding soil, and inhalation of tobacco smoke is an efficient means of ingesting cadmium [2,3]. Less commonly, cadmium toxicity is due to ingestion of tainted food – particularly rice – water, or air contamination [4]. Chronic exposure of cadmium at doses commonly ingested by cigarette smokers can lead to bone demineralization and lead to an increased risk of cancer, diabetes and damage to the kidneys, testis, and lungs [5,6]. Cadmium is slowly excreted by humans, with a half-life of 15-20 years, leading to increasing toxicity as the cadmium is accumulated [7].

Cadmium is taken up by yeast in competition with divalent cations such as calcium, magnesium, or zinc, implying that cadmium enters the cell via divalent cation

pumps [8]. For example, deletion of Zrt1p, a gene that expresses a zinc import pump, decreases cadmium uptake by yeast [9]. Once cadmium enters the cell it causes oxidative stress and DNA damage [1]. Cadmium has a full d orbital shell, it is not redox-active and thus cannot initiate Fenton type reactions, so this increase in oxidative stress must be due to indirect effects. And while cadmium does bind to DNA, it does so rather weakly and competitively with magnesium; at biologically relevant concentrations of magnesium and cadmium, binding of cadmium to DNA should be negligible [10]. Along those lines, it has been shown that cadmium inhibits mismatch repair *in vitro,* leading to increased mutagenesis [11]. The separate effects of increasing oxidative stress – which can increase DNA damage – and decreased capacity to correct defects in DNA seem likely to be the cause of cadmium's toxicity.

The origins of both of these effects are unclear. It has been shown in yeast and other organisms that cadmium binding to glutathione is one of the primary pathways for detoxifying cadmium and other heavy metals [12,13]; additionally, cadmium is known to bind to metallothionein, another sink for transition metals *in vivo* [14]. Since both metallothionein and glutathione are both involved in detoxifing reactive oxidative species (ROS), it is possible that the increased oxidative stress is simply due to a decreased availability of these important species [1]. Indeed, it has been shown in yeast that cadmium binds to either glutathione or glutathione derivatives in the cytosol, forming bis-glutathienato cadmium ($CdGSH_2$) or similar complexes, which are then transported into the vacuole by the vacuolar glutathione S-conjugate pump YCF1 [15]. While introduction of cadmium to the cell causes an increase in GSH synthesis [16], it is possible that a significant fraction of the GSH in the cell is tied up binding cadmium in

the cytosol and vacuole, which might easily result in increased oxidative stress. Typical concentrations of GSH in the cell are between 1-10 μM [32], so the amount of cadmium imported into the cell would have to be rather substantial in order to directly affect the antioxidant capacity of the cell.

While an increase in the cell's oxidative stress could be solely responsible for the mutagenesis associated with cadmium, *in vivo* studies in yeast by Gordenin and coworkers suggests otherwise. Grodenin showed that low dose – in the range of 1-10 micromolar – treatment with cadmium results in an increase in mutability of long homonucleotide runs in the gene LYS2 [11]. Other agents that cause similar amounts of oxidative stress did not cause comparable damage, and cadmium caused only a slight increase in recombination, suggesting that the damage was caused by an inhibition of DNA repair, rather than by an increase in DNA damage. Grodenin suggests that a possible mechanism for this decreased proofreading ability is cadmium binding to the cysteine-containing active sites of zinc finger proteins, displacing the metal and causing the protein to lose functionality. Additionally, cadmium is known to displace copper from metallothionein [33], which binds copper in the cell. So, cadmium might increase the oxidative stress in the cell further by displacing copper from metallothionein and iron and copper from other metalloproteins; since these metals are redox-active even a small increase in free copper or iron concentration would increase the amount of oxidative stress in the cell.

In this chapter we examine the effects of cadmium toxicity on the metal distribution of the cell, and how it effects localization and speciation. We can then use

tools such as XRF microscopy and XAS to gain insight into if and how cadmium affects metal homeostasis in yeast.

Experimental Procedures

These measurements were done in collaboration with Nathan Zahler and Andrea Stoddard of the Fierke lab; they developed the protocols for growing and harvesting yeast, and assisted with sample preparation and data collection at the beamline . Yeast were grown in a defined synthetic medium to mid-log phase. Cadmium was then added to the medium and the cells were incubated for 6 hours. Two different cadmium concentrations were used, the lower of which decreased the doubling rate of the yeast by approximately one half (75 micromolar $CdCl_2$); the higher concentration of 250 micromolar $CdCl_2$ decreased the doubling rate by 90%. The cells remained viable; if they were washed and placed in fresh media, they resumed growth. Cells were washed with deionized water and imaged by XRF microscopy on beamlines 2-ID-D and 2-ID-E at the Advanced Photon Source at Argonne National Lab in the same manner as described in Chapter 2.

Zinc and cadmium X-ray absorption spectra were collected at the Stanford Synchrotron Radiation Laboratory at beamline 9-3 for intact cadmium-treated yeast. Spectra were collected in fluorescence mode using a Si[111] double crystal monochromator and a Canberra 30-element germanium solid-state fluorescence detector. Sample temperature was kept at 10-12 K using an Oxford Instruments continuous-flow liquid-helium cryostat. Three nitrogen-filled ion chambers were used to measure the intensity of the incident X-rays: the first before the sample (I_0), and the other two after the sample (I_1 and I_2). Either a cadmium or zinc foil was placed between I_1 and I_2 to

measure the spectrum of the metal for energy calibration purposes. All spectra were measured using 10 eV steps in the pre-edge region with one second integration times, 0.4 eV steps with an integration time of 1 second in the edge region, and 0.05 $Å^{-1}$ in the EXAFS region with k^3-weighted integration times from 1-20 seconds. Three or four spectra were measured for each sample, and EXAFS spectra were measured out to k=13 $Å^{-1}$. Each fluorescence channel was checked for glitches; after bad channels were removed, spectra were averaged using the EXAFSPAK suite of programs [18] and then background subtracted and normalized to give the final spectra [19]. The spectra were converted to k space (E_0=9675 for zinc and E_0=26720 for cadmium) and were fitted with the EXAFSPAK suite of programs.

Results

Figures 3.1 and 3.2 show false color images of XRF microscopy data taken of a typical single cell (Fig. 3.1) and budding yeast (Fig. 3.2) treated with 250 μM $CdCl_2$. Likewise, Figures 3.3 and 3.4 are false color images of XRF data taken of a single cell (Fig. 3.3) and a budding yeast (Fig. 3.4) treated with 75 μM $CdCl_2$. The elemental distribution of these cells shows little difference compared to that of the untreated yeast, apart from the striking localization of copper to the bud and bud neck. Table 3.1 (prepared by Nathan Zahler, who examined each image measured and determined by eye if there was significant copper localization and where the localization occurs) shows the frequency of the localization to bud and to the bud neck (Cu Ring) in two different strains of yeast, EJG1117 and ATCC201389. This localization does not occur in the yeast that were not treated with $CdCl_2$, and seems to occur more frequently at the higher

concentration of cadmium. While the localization to the bud neck is striking, it covers a relatively small area of the cell, and has a concentration that is typically only 2-3 times higher than the rest of the cell. Five such localizations were found to contain 6×10^4 copper atoms ($\pm1.8\times10^4$); an average yeast cell contains 1.8×10^6 copper atoms, making the copper atoms localized to the bud neck a relatively small fraction of the total cellular copper pool. The localization of copper to the bud is more variable and can range from a 2-10 fold increase in copper concentration compared to the rest of the cell. Since the localization to the bud covers a larger area in addition to being more intense, this pool can represent a substantial fraction of the cell's copper, often in excess of half the cell's copper.

While copper is the only element to show a noticeable change in distribution, treatment of yeast by cadmium does affect other elements. Figure 3.5 shows the average elemental content of yeast (both budding and single yeast are combined in this figure) for 250 μM $CdCl_2$, 75 μM $CdCl_2$, and no cadmium. Figure 3.6 shows the same data, with the elemental averages of the high and low cadmium groups normalized to the cells not treated with cadmium. Figure 3.6A shows total cellular content of each element, while 3.6B gives the average two dimensional concentration ($\mu g/cm^2$). The latter is important because the cadmium-treated cells have a slightly larger area (implying a larger volume) than the untreated cells.

Most elements – even bulk elements such as potassium – show increases on cadmium treatment; however, the average scatter for each cell also increases from (1.3 +/- 0.1)$\times10^4$ counts/cell for the untreated cells to (2.0 +/- 0.2)$\times10^4$ counts/cell for the

cells treated with 250 μM $CdCl_2$, indicating that treatment of cells with cadmium results in a nearly 50% increase in cell size. Because of this increase in cell size, it is possible that the two-dimensional "concentration" (expressed in $\mu g/cm^2$) that is measured with XRF will not reflect the true concentration of the cell, since volume increases in proportion to the cube of the radius while area increases by the square of the radius. Figure 3.7 shows total average elemental content normalized to scatter, which should be a reasonable surrogate for average cellular concentration. In Figure 3.7A, the data for all yeast are shown, while in figure 3.7B, the data are shown for only those yeast with noticeable buds. Once this normalization is done, the changes in concentration for most of the bulk elements disappear.

It is interesting to note that while many cells in the low cadmium condition show unusual localization of copper, the concentration of copper does not appreciably increase. This is consistent with calculations (above) showing that only a few percent of this total cellular copper is localized to the bud neck in the low cadmium cells. While the amount of the localized copper is small, it is potentially an important finding, given that the copper is tightly regulated in the cell and such localization is not easily explainable.

Figure 3.8 shows the elemental concentrations of budding yeast under all three cadmium concentrations with the data segregated by mother and daughter cells. For these calculations, the bud area was defined by drawing a region of interest around the daughter cell, which was assumed to be the smaller of the two cells. The bud region shows small and mostly insignificant increases in K ($p=0.23$ for uninhibited and $p=0.01$ for high cadmium) and Ca ($p=0.13$ for uninhibited and $p=0.07$ for high cadmium). While

these differences are not highly significant, they may reflect the need for the calcium-rich cytoskeleton to build up the bud prior to enlargement. Interestingly, there appears to be a small decrease in phosphorous concentration in the bud ($p=0.08$). This could occur if the vacuole, which accounts for most of the cellular phosphorus (see chapter 2), has not yet been formed in the cell.

Both iron and zinc show small dose-dependent increases in concentration on cadmium treatment. At 75 μM cadmium, only the mother cells show a significant increase, while at 250 μM cadmium both mother and daughter show an increase. In contrast, copper shows a very different behavior. At 75 μM cadmium there is no significant change in copper concentration in either the mother or the daughter cell, consistent with the data in Figure 3.7. In contrast, at 250 μM cadmium there is a nearly five-fold increase in copper concentration, but only in the bud.

None of the previous results have addressed cadmium concentration or localization; this is because cadmium's fluorescence peak overlaps with the much more abundant – often two orders of magnitude in a typical cadmium-treated cell – potassium fluorescence peak (3.13 eV for Cd, 3.31 eV of K) , making quantification of cadmium difficult. The results discussed above were measured with a detector with relatively poor energy resolution, making quantification of cadmium impossible. More recently, we measured cadmium-treated cells with a detector with better energy resolution, and we were able to quantify the cadmium content of the cells. Figure 3.9a is a false-color plot showing distributions of various elements, including cadmium, in a typical cell treated with 250 μM $CdCl_2$. The most intense region of cadmium fluorescence corresponds with

the area of high phosphorus, which is typically the vacuole of the cell. Figure 3.9b is a surface plot of the cadmium fluorescence; this clearly shows that while cadmium is slightly more concentrated in the vacuole, this concentration is only roughly twofold higher than elsewhere, and that there is consequently a significant amount of cadmium in the rest of the cell. In fact, the localization of cadmium to the vacuole of this cell is less significant than the localization of zinc to the vacuole. This implies that there is a substantial amount of cadmium in the cytoplasm of the cell, and that cadmium is not quickly shunted into the vacuole where it can do little damage.

In an effort to quantitate the heterogeneity in elemental distribution, we have prepared scatter plots of elemental fluorescence versus scatter for each cell (data not shown). If an element was uniformly distributed, the correlation coefficient of such a plot should be 1 for noise-free data. Given the statistical uncertainties in our data based on the count rate per pixel, the highest value we could expect ranges from 0.92 for iron to greater than 0.99 for potassium. These estimates were generated by taking the average slope of fluorescence versus scatter for several cells. Noiseless data were generated by simply applying values of the scatter of a cell to that linear function, and Poisson noise was added to both the scatter and the idealized fluorescence, and the correlation coefficients were calculated for each element. Plots of the average correlation coefficients for yeast (both single and budding cells) are shown in Figure 3.10. Most elements show the expected correlation coefficients, and show little variation in correlation coefficient as a function of cadmium treatment. The exceptions are sulfur and zinc, which shows a minor decrease in correlation coefficient, and copper, which shows a dramatic decrease. The latter reflects the copper localization that was seen in Figure 3.3

and Table 3.1. The former suggests that there may also be more subtle variation in zinc and sulfur distribution upon cadmium treatment. Given the finding (see Chapter 2) that phosphorous is an approximate marker for the vacuole, scatter plots of each element versus phosphorous gives a measure of the extent to which an element colocalizing with phosphorous, and therefore the vacuole. The correlation coefficients for the plots (Fig. 3.10) are generally unsurprising, with little change in correlation coefficient in response to changing cadmium dose, aside from the previously noted localization of copper. One intriguing exception is that the correlation of iron with phosphorous significantly increases with cadmium treatment. Since the cadmium causes a 2-3 fold increase in iron, the correlation coefficients suggest that much of this added iron is localized to the vacuole.

Figure 3.11 shows scatter plots for each data point over the entire populations of cells (yeast that have not been treated with cadmium are red, those treated with the high dose are blue). The plot of phosphorous versus scatter (Fig 11a) shows a similar distribution for both populations. As mentioned in the previous chapter, the region of high phosphorous and comparatively low scatter is a marker for the vacuole; while both populations have such data points, the cadmium-treated cells have more of these points, and they extend to higher concentrations of phosphorous. The plots of iron and zinc versus phosphorous are consistent with the excess iron and zinc in the cell being stored in the vacuole, since the areas of high metal are typically also high in phosphorous. Copper, on the other hand, does not show this pattern. The pixels of abnormally high copper do not typically have a higher amount of phosphorous; this result is unsurprising given that

we typically saw areas of high copper concentration in the bud and bud neck, rather than the vacuole.

Figure 3.12 shows the results for whole-cell zinc XANES measured at 0, 75, 250 μM $CdCl_2$. The decrease in intensity of the principal absorption peak from 340 g/cm^2 for the yeast not treated with cadmium to 310 for the yeast treated with 250 μM cadmium represents a significant change in the average zinc environment; the smallest value possible for the principal absorption peak would be around 250 g/cm^2. Figure 3.13a shows the EXAFS and fits for the yeast treated with 0 and 250 μM $CdCl_2$; Figure 3.13b shows the Fourier transform of these data. While both sets of data fit well with one shell of O/N at 2.04Å and a sulfur shell at 2.33 Å, the high cadmium sample has increased sulfur ligation and decreased O/N ligation compared to the untreated yeast (Table 2). Figure 3.14 shows the cadmium EXAFS and fit and Fourier transforms for the yeast treated with 250 μM $CdCl_2$. There is no difference between the spectrum of the yeast treated with 75 μM $CdCl_2$ (not shown) and those treated with 250 μM $CdCl_2$; the two sets of data are identical, fitting well with one shell of sulfur at 2.52 Å (table 2).

Discussion

The localization of copper to the bud and bud neck is the most visually dramatic result of cadmium treatment. The bud neck consists mostly of chitin, actin, and septins that serve as a diffusion barrier between the mother and daughter cells [20]; none these proteins are known to bind copper. Additionally, when the response of the yeast proteome to cadmium stress was determined, none of the proteins that were found in increased amounts are known to contain copper [21]. Localization of GFP-labeled actin,

however, shows remarkably similar patterns in localization when compared to the localization of copper shown by XRF microscopy (Figure 3.15) [22]. And, while actin is not known to bind copper, it has recently been hypothesized that two cysteines, C285 and C374, act as sensors of oxidative stress, forming a disulfide bond when the cell is exposed to increased concentrations of ROS [23]. Given that these two residues are exposed enough to serve as a sensor for oxidative stress and in close enough proximity to form a disulfide bond, it seems possible that free cellular copper binding to C285 and C374 is responsible for the observed localization. Given how tightly copper is thought to be regulated *in vivo*, this would be a remarkable result. In addition to causing localization of copper, cadmium also increases the concentration of zinc, copper, and iron.

The amount of cadmium in the cytosol is significant, roughly comparable to that of zinc. This shows that the cadmium is not quickly sequestered into the vacuole, but rather is free in the cell, or at least bound to metallothionein or GSH, possibly reducing the antioxidant capacity of the cell. The cadmium EXAFS results of the cadmium-treated yeast show no change in the average ligation of the cadmium as the cadmium concentration increases, and the Debye-Waller factor for the fit is relatively low, suggesting a homogenous population. The cadmium environment is consistent with metallothionein [24], although these data are unable to distinguish between metallothionein and another four-coordinate set of sulfur ligands, including GSH.

The zinc XAS data show that cadmium treatment has a large effect on the average zinc environment in a yeast cell. There is a roughly 1.5 fold increase in zinc concentration upon treatment with 250 μM cadmium, and the large change in the

XANES spectrum upon cadmium treatment indicates a change in the zinc environment of close to that size of increase. The decrease in intensity of the principal absorption peak is from 340 to 310 g/cm^2. Given that the lowest value possible is around 250 g/cm^2 and not zero, this covers about one third of the available range, suggesting that at least one-third of the zinc in the cell changes chemical environment on cadmium treatment. That is, if all of the excess zinc that is taken up on cadmium treatment has an edge jump of 250 g/cm^2 and none of the other zinc environments change, this would account for the observed XANES. Published spectra for zinc-metallothionien give a peak height of around 275, in reasonable agreement with this estimate [26]. It is important to note that one-third of the zinc being in a new environment is the minimum required – the amount of zinc that changes environment could be higher. Upon treatment with 250 μM cadmium, the zinc EXAFS shows an increase in sulfur ligation from 2 to 3.2, with a corresponding decrease in O/N ligation from 3.3 to 2.4. If all of the increase in zinc concentration were put into a four-coordinate sulfur site with a low-intensity principal absorption peak, such as metallothionien, it would explain the changes in both the zinc EXAFS and XANES. Interestingly, while zinc/phosphorous scatter plots suggest that much of this excess zinc is stored in the vacuole, previous EXAFS of zinc stored in the yeast vacuole show the zinc environment to be uniformly O/N ligation at 1.98 Å [25]. Thus, our results are consistent with the zinc being pumped into the vacuole with sulfur ligation, perhaps bound to glutathione.

The increase in copper and iron concentration are likely to be the most important consequence of cadmium treatment, at least as far as growth inhibition is concerned,since these are redox-active metals. The increase in iron concentration is already apparent at

75 μM cadmium, while there is still little increase in copper. This suggests that the initial growth inhibition may be caused by excess iron, which is known to cause oxidative stress. There is no obvious reason that increased cadmium should cause an increase in iron. Waters and Eide [27] have shown that the low affinity iron transporter FET4 is regulated both by Aft1 and Zap1, proteins which regulate iron and zinc, respectively. If cadmium treatment was to interfere with the Zap1 structure, this could up-regulate Fet4 and then increase the concentration of both iron and zinc. However, since zinc should be much more available under our growth conditions, this seems unlikely to explain the fact that iron increases more than zinc on treatment with 75 μM cadmium. The increase in both copper and iron on treatment with 250 μM cadmium appears on the surface to be even more perplexing. However, a link between copper and iron metabolism is well established, since the high affinity iron uptake protein Fet3 is a multicopper oxidase [28]. If cadmium interfered with iron sensing so that cadmium-treated cells behaved as though they were iron-starved, induction of Fet3 could account for the increase in both iron and copper. In this model, the yeast treated with 75 μM cadmium may have enough copper to fully load Fet3 by redistribution of copper. At higher cadmium, as more Fet3 is made, there could be an increase in total copper. The weakness to this model is that no link between cadmium and Aft1 (the iron regulatory protein) has been established, although there is an essential zinc in the analogous bacterial iron regulatory protein fur.

Although the present data do not allow a detailed molecular description of why cadmium causes yeast cells to take up iron, copper, and to a lesser extent zinc, they do suggest a new model for thinking about cadmium-induced oxidative stress. Complex interactions between iron and zinc [29,30] and between iron and copper [31] have been

shown previously. The present data extends this to cadmium, which affect the concentration of all three metals.

Similarly, while these data are not able to conclusively show why cadmium causes cellular damage, they do provide hints about how cadmium might increase a cell's level of oxidative stress. As noted above, cadmium treatment increases concentrations of iron and copper in the cell; this increase in cellular concentration alone could cause the increase in oxidative stress. However, given the dramatic change in copper distribution in the cadmium cells, it seems possible that one of the origins of the oxidative stress caused by cadmium poisoning is due to an increase in free copper, rather than just an increase in total amount. This hypothesis could be further tested by using copper-sensing fluorophores to measure the concentrations of free copper changes in the cell. If free copper was found to increase upon cadmium treatment in yeast, then that result combined with the data presented in this chapter would provide a convincing mechanism for how cadmium causes cellular damage.

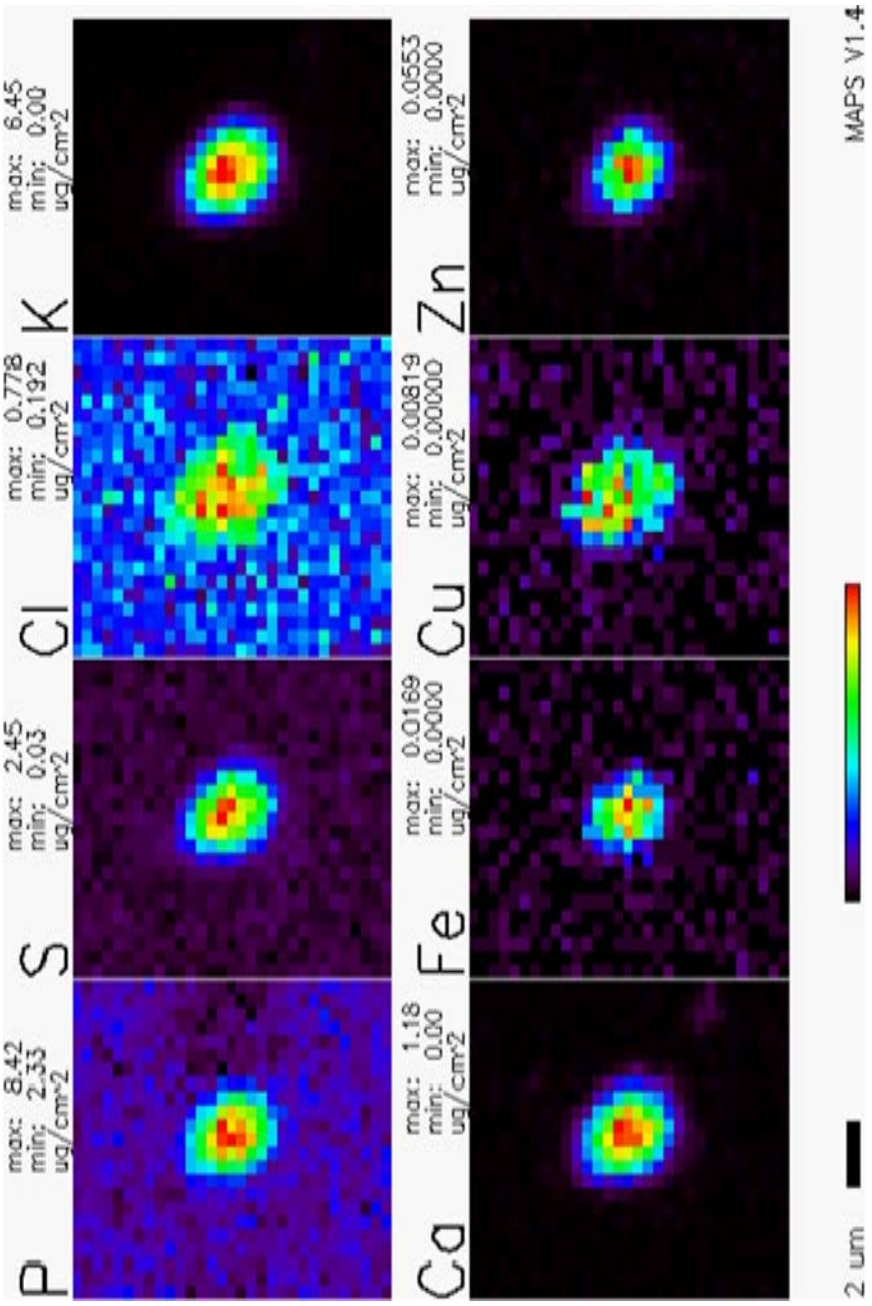

Figure 3.1. False-color XRF image of a typical single yeast treated with 250 μM $CdCl_2$

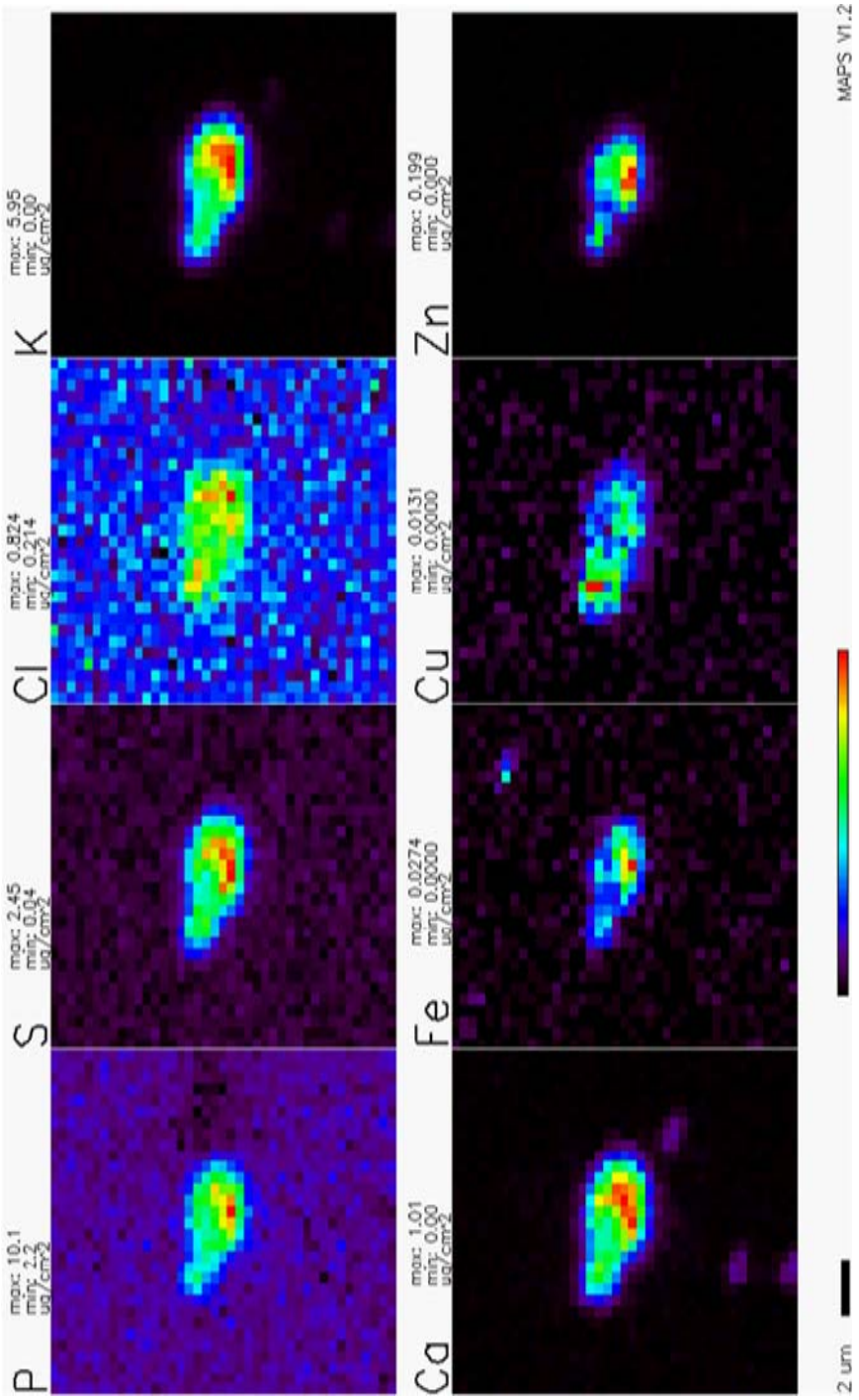

Figure 3.2. False-color XRF image of a typical budding yeast treated with 250 μM $CdCl_2$.

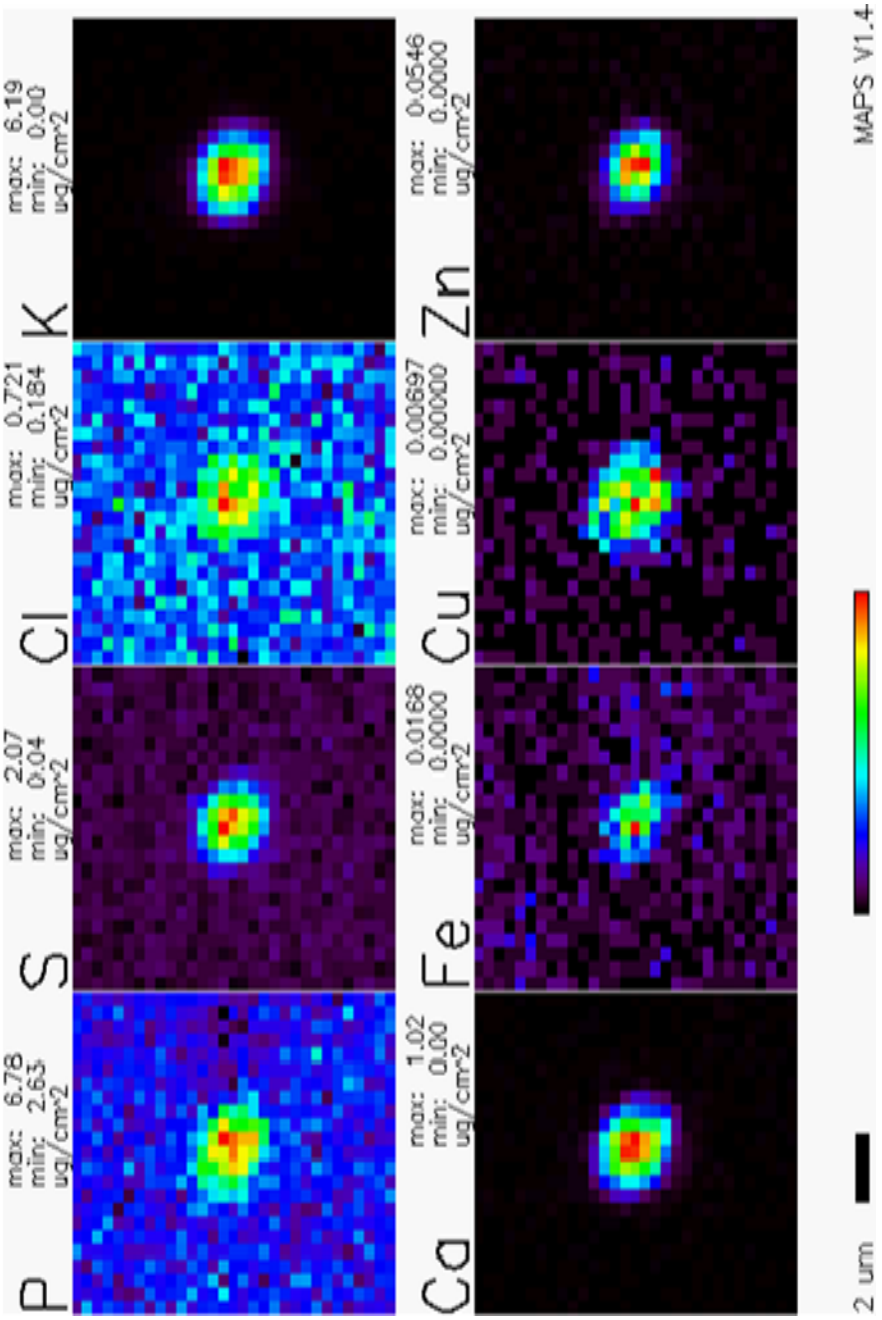

Figure 3.3. False-color XRF image of a typical single yeast treated with75 μM $CdCl_2$

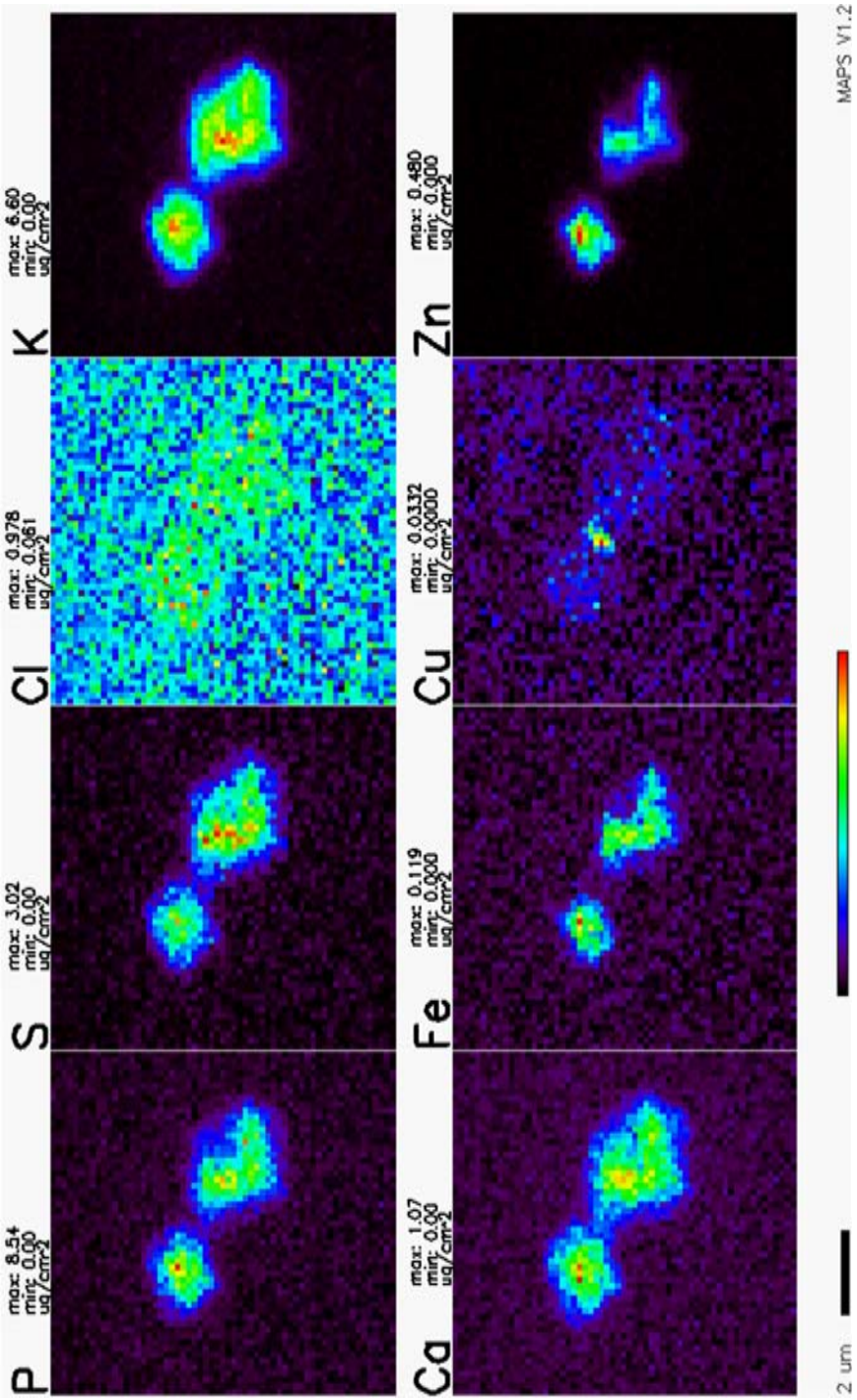

Figure 3.4. False-color XRF image of a typical budding yeast treated with 75 μM $CdCl_2$.

Cd concentration	Strain	Budding yeast	Frequency of Cu ring	Frequency of Cu in Bud
No Cd	EJG1117	22	0	0
	ATCC 201389	15	0	0
75 μM	ATCC 201389	15	5 (33%)	4 (27%)
250 μM	EJG1117	19	4 (21%)	6 (32%)
	ATCC 201389	21	17 (80%)	11 (56%)

Table 3.1. This chart shows the frequency of significant copper localization in two different strains of yeast. The "Cu ring" refers to specific localization to the bud neck, an example of which is seen in Figure 3.4. An example of the copper localization in the bud is shown in Figure 3.2.

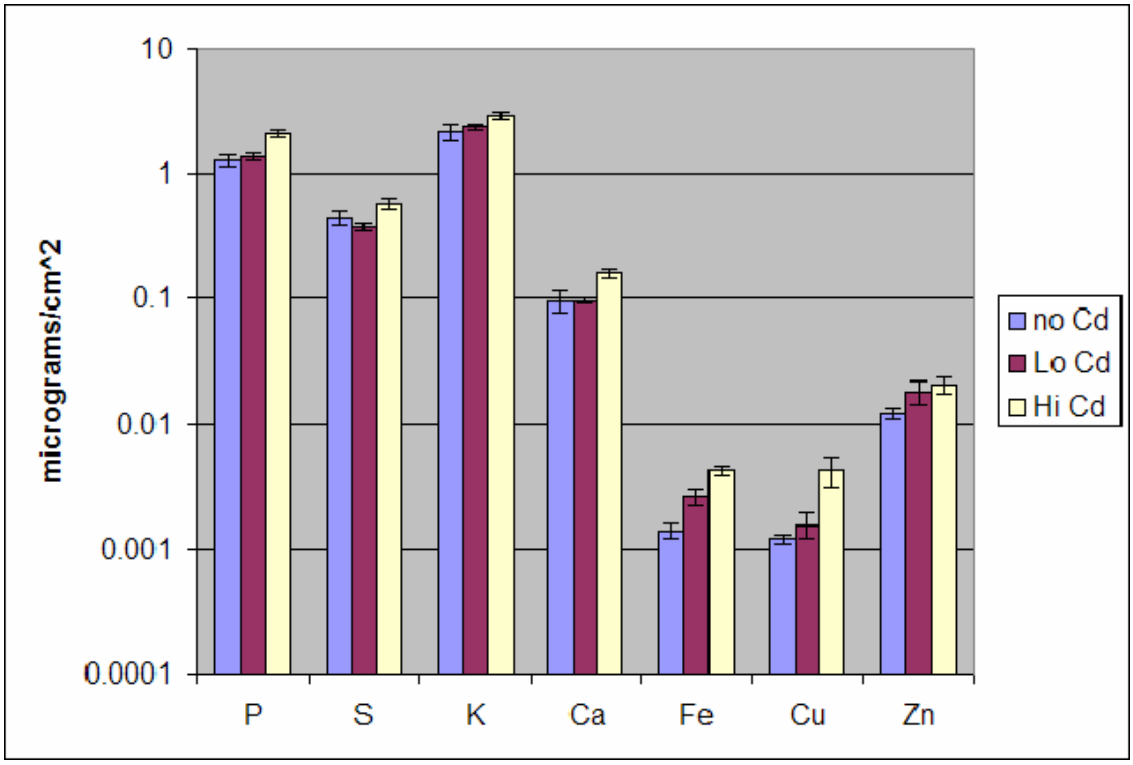

Figure 3.5. Average two-dimensional concentration of all yeast measured (budding and single cells), for all three cadmium concentrations. Low cadmium cells were exposed to 75 μM $CdCl_2$, while high cadmium cells were exposed to 250 μM $CdCl_2$.

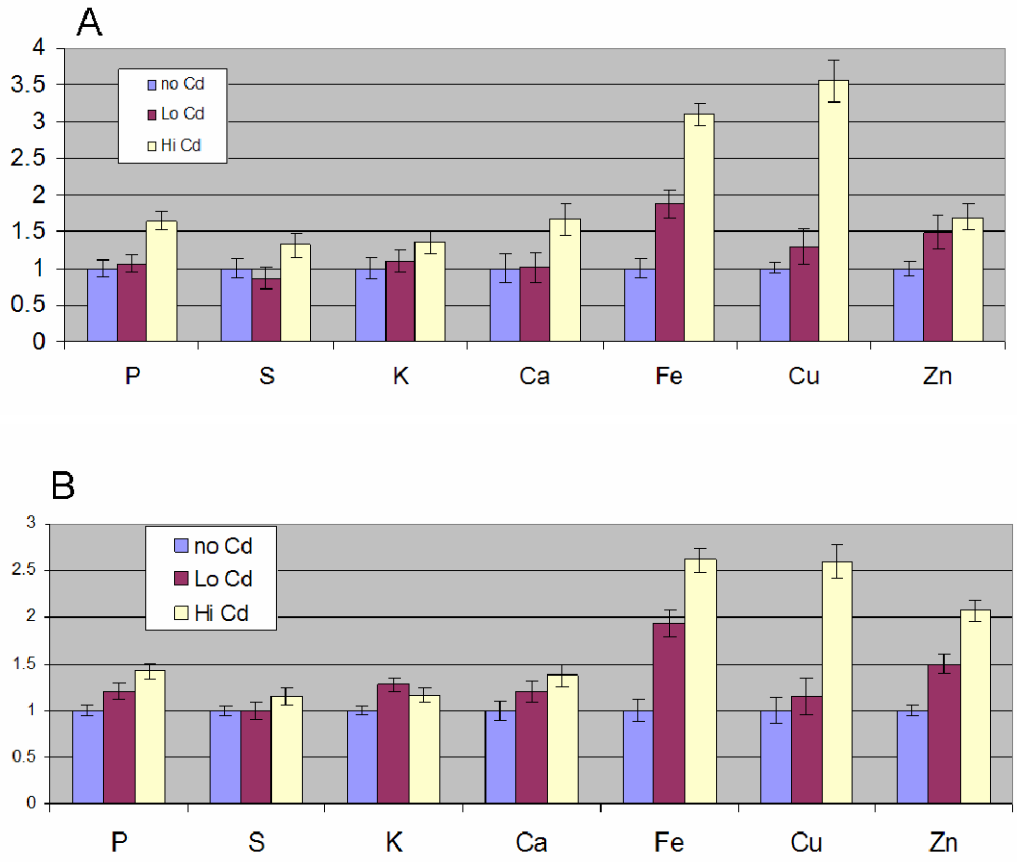

Figure 3.6. Figure 3.6a shows the total elemental content of all yeast cells measured, with all conditions normalized to the cells not treated with cadmium. Figure 3.6b, also normalized to the untreated cells, shows two-dimensional concentration.

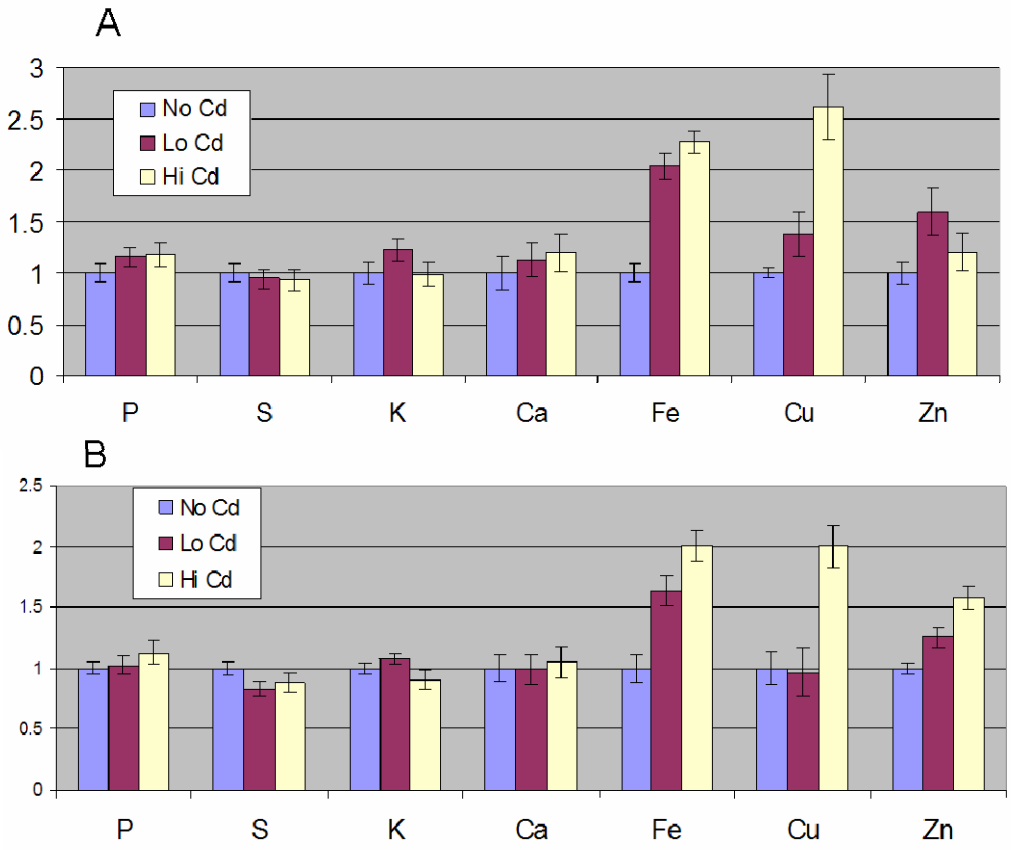

Figure 3.7. Figure 3.7a is the total elemental content of all yeast normalized to scatter, while Figure 3.7b is the normalized elemental content only the yeast with noticeable buds.

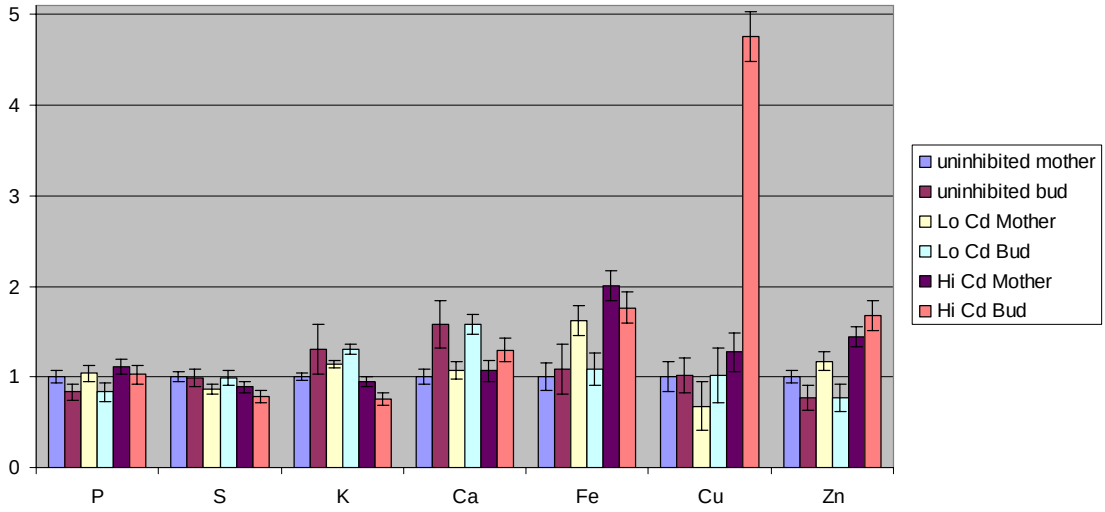

Figure 3.8. Elemental content normalized to scatter of the mother and bud cells for all three cadmium conditions. All cells are normalized to the mother cells of the uninhibited yeast.

A

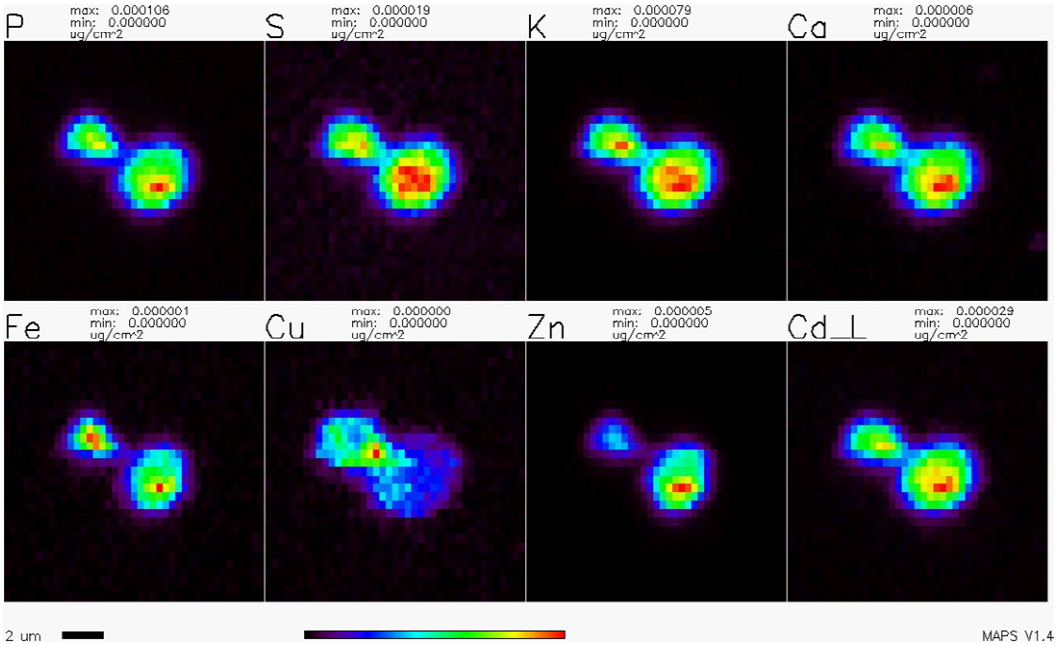

B

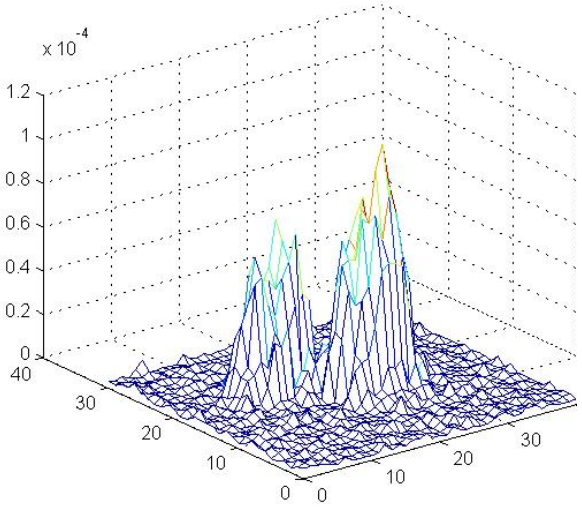

Figure 3.9. Figure 4.9a is a false-color image of a budding yeast treated with 250 μM $CdCl_2$, with the cadmium image included. Figure 4.9b is a surface plot of the cadmium fluorescence.

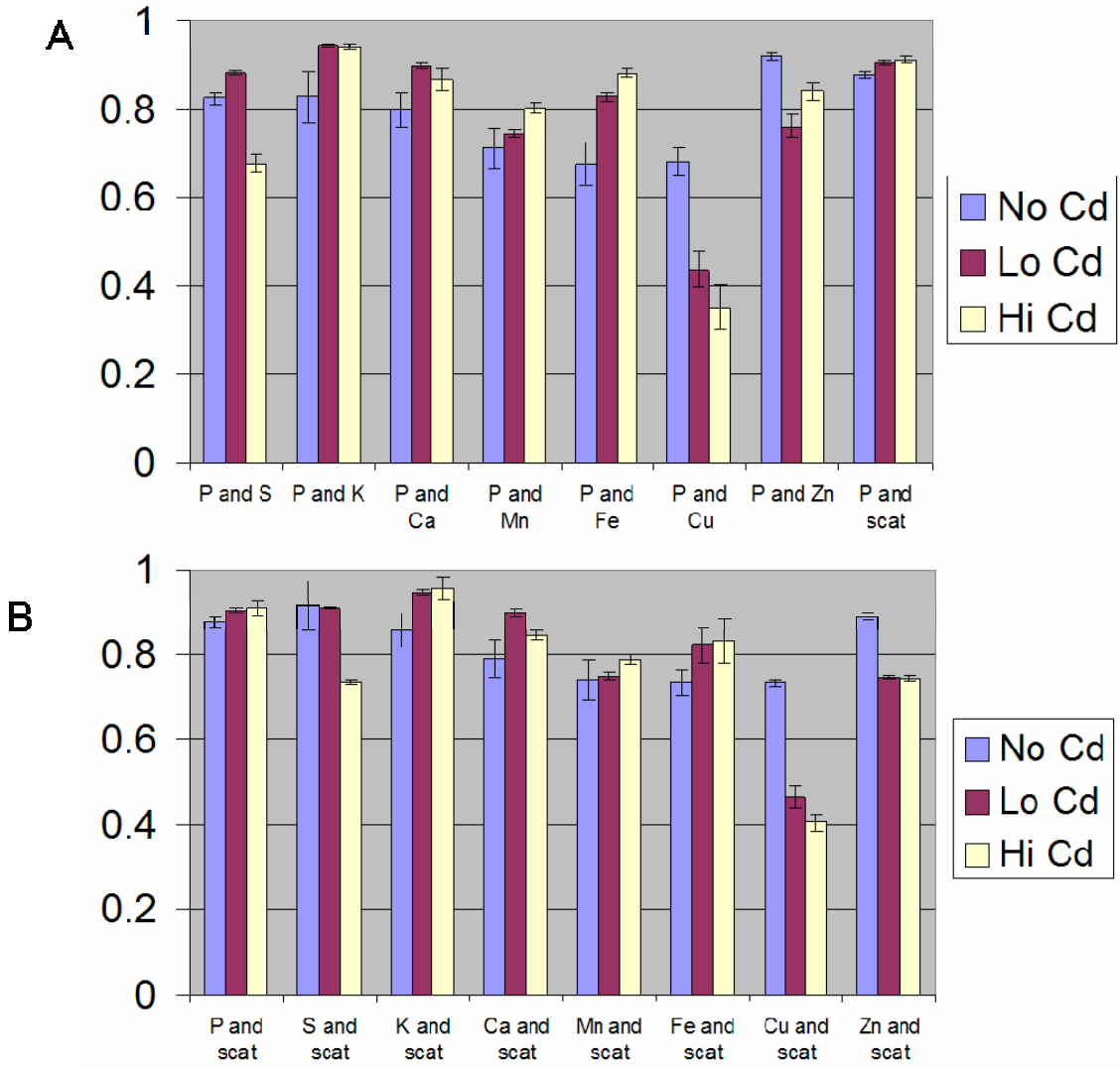

Figure 3.10. Correlation coefficients of cells grown under 0, 75, and 250 μM $CdCl_2$. These coefficients were calculated using both budding yeast and those with no apparent bud.

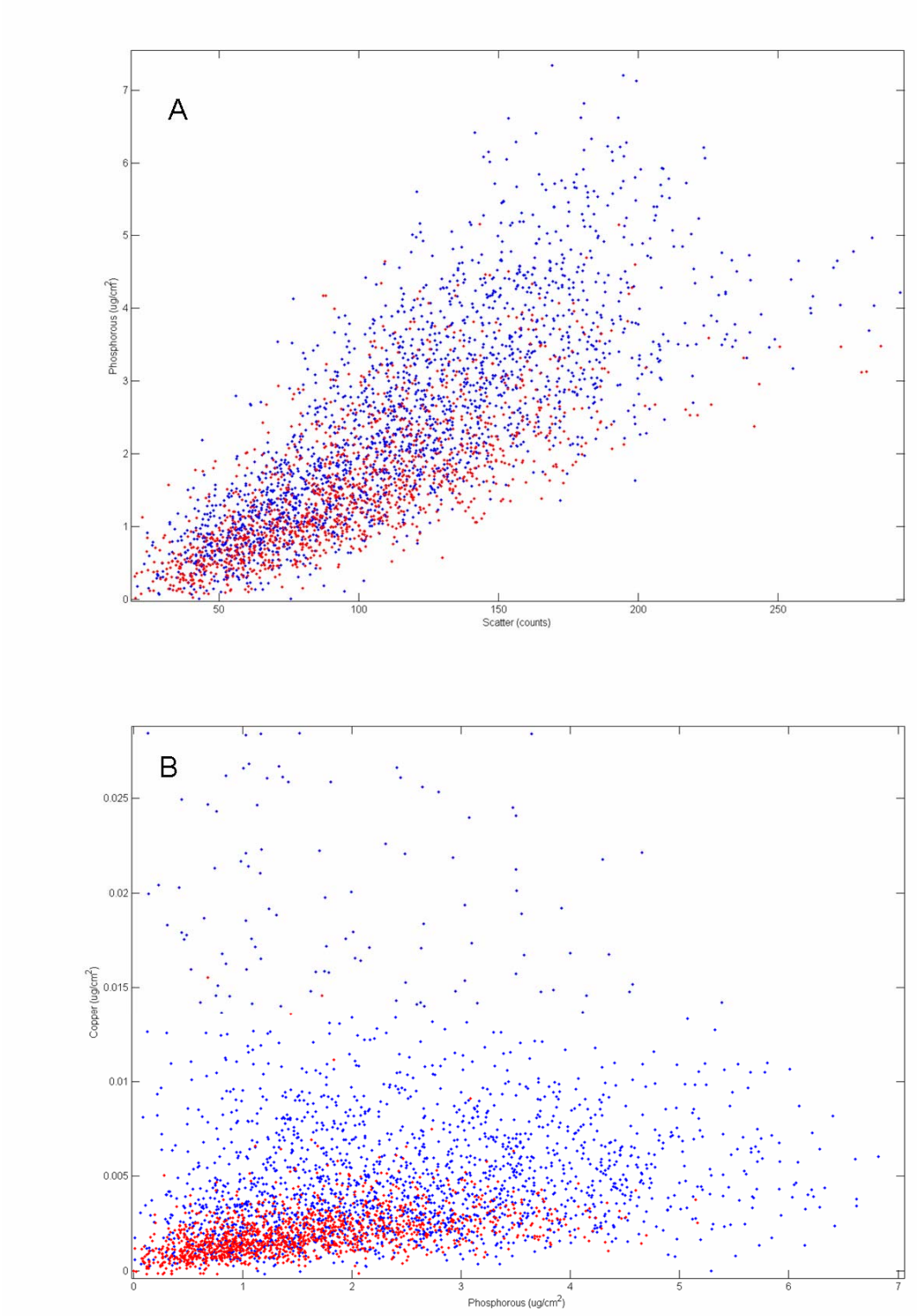

Figure 3.11. Figure 11a is phosphors plotted against scatter , while 11b is copper plotted against phosphorus for all cells,. This is the sum of all the cells measured. The red points represent yeast not exposed to cadmium; the blue points, yeast exposed to 250 μM $CdCl_2$.

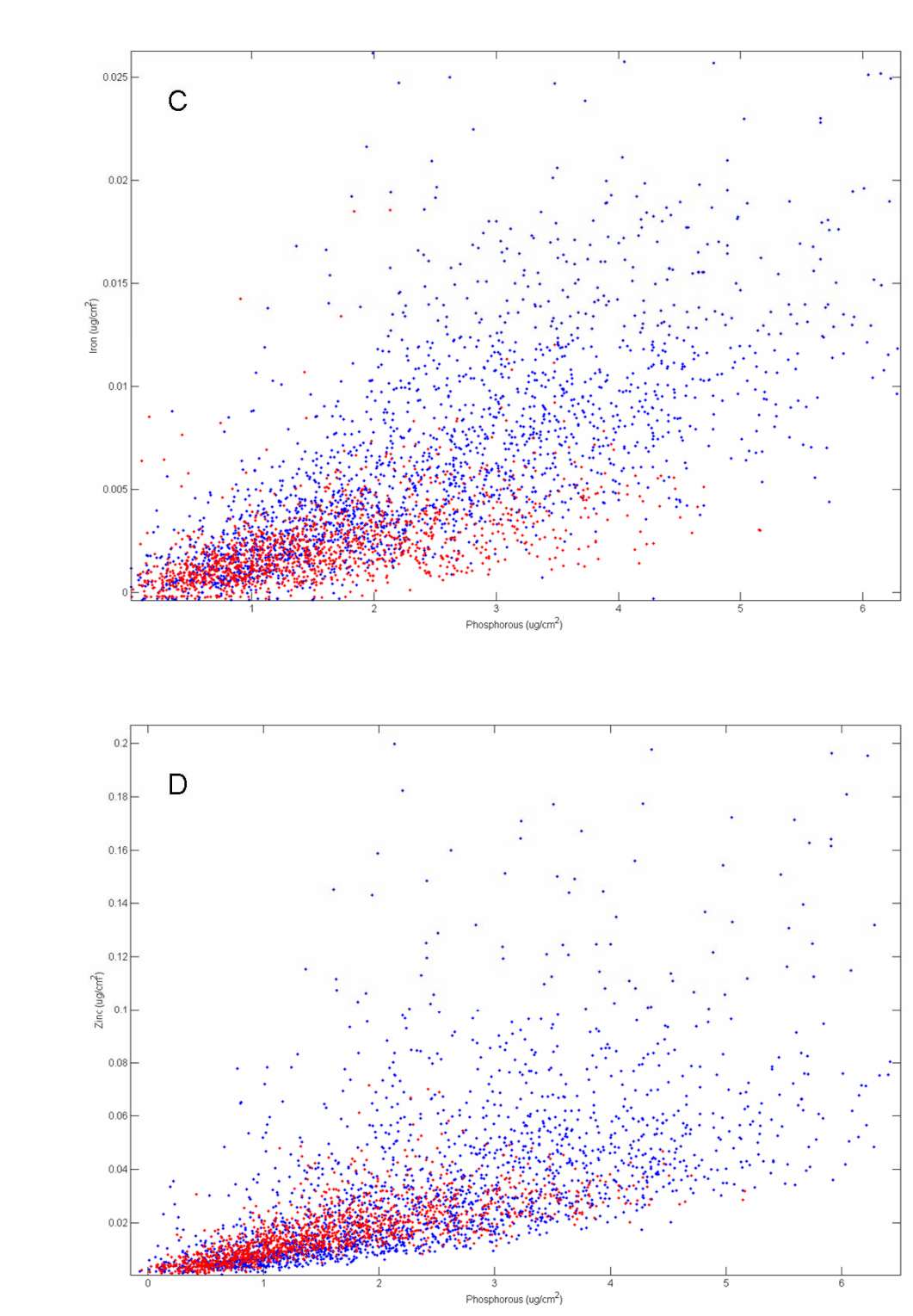

Figure 3.11 (cont). Figure 11c plots iron versus phosphorus, while 11d plots zinc versus phosphorus. Again, The red points represent yeast not exposed to cadmium; the blue points, yeast exposed to 250 μM $CdCl_2$.

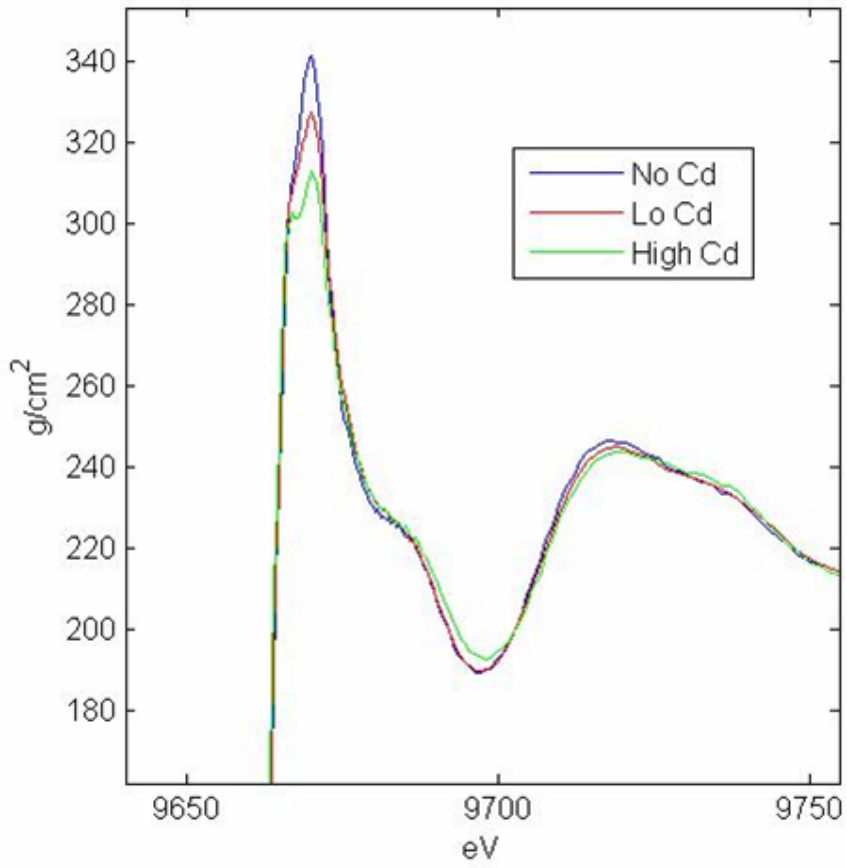

Figure 3.12. Close up of XANES region of whole cell XAS measured at beamline 9-3 of SSRL.

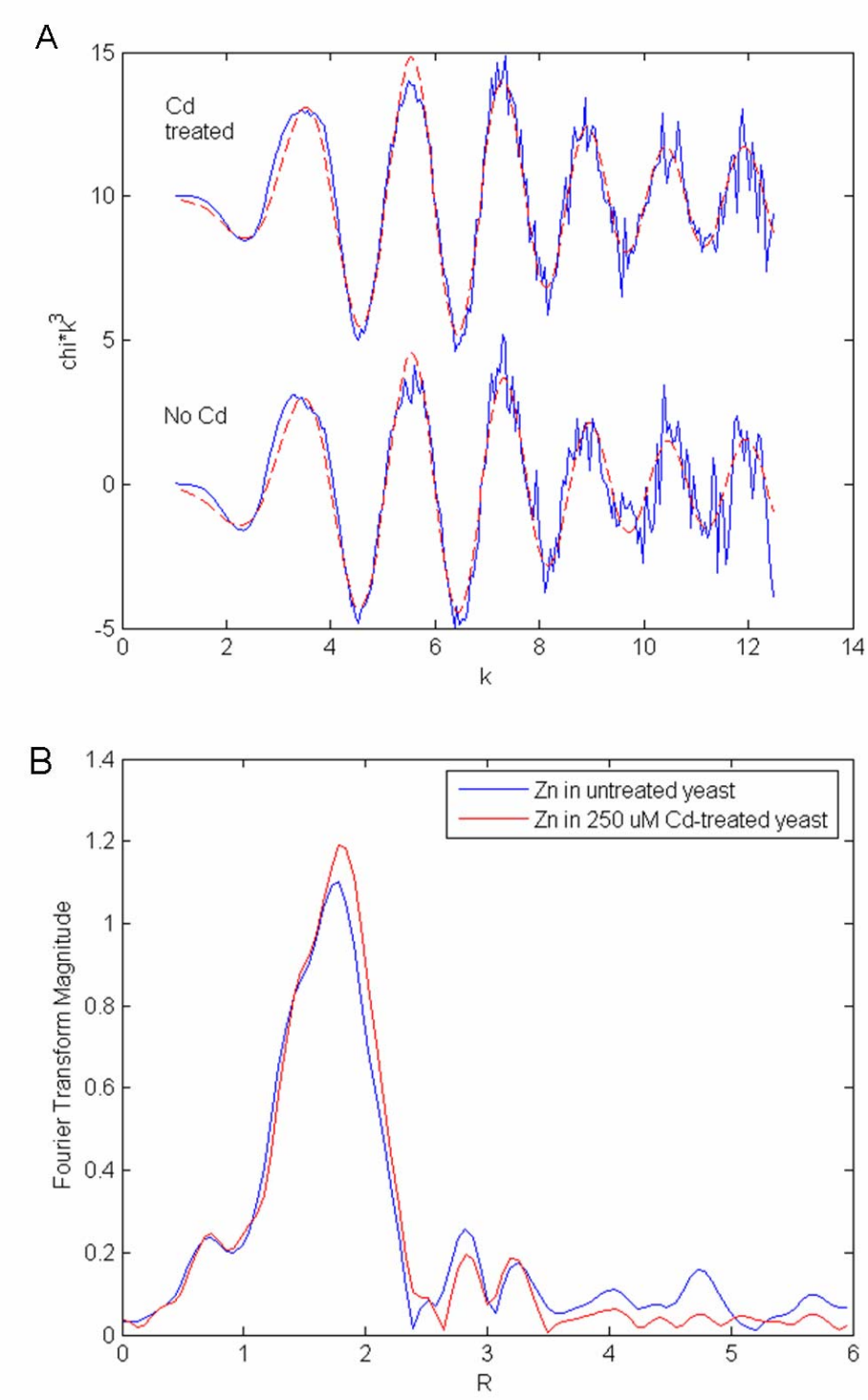

Figure 3.13. Whole cell zinc EXAFS of untreated and 250 μM $CdCl_2$ treated yeast. Figure 3.13a shows k^3-weighted EXAFS (blue) and fit (red) , and 3.13b shows the Fourier transform.

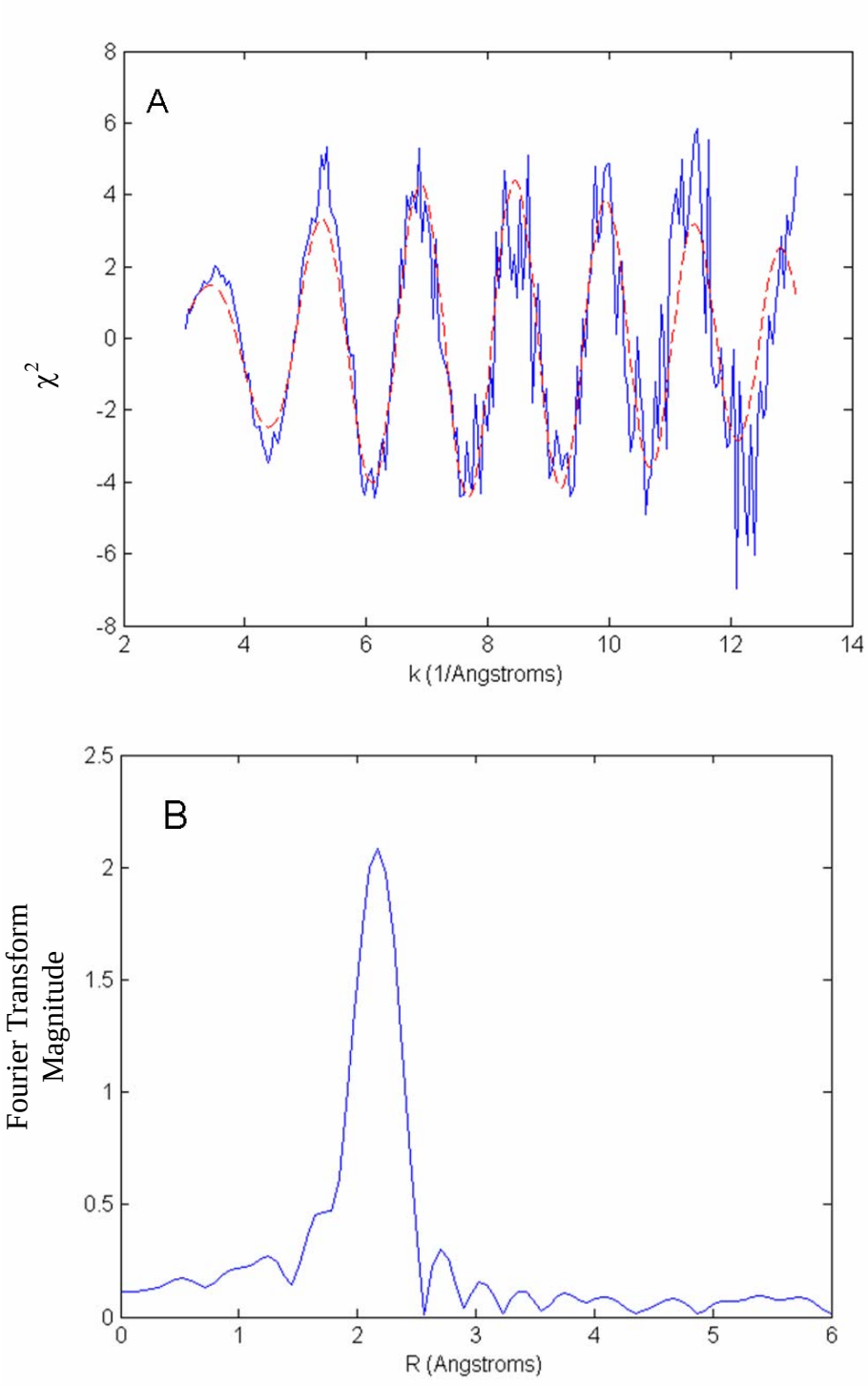

Figure 3.14. Figure 3.14a is the k^3-weighted Cd EXAFS (blue) and fit (red) of the 250 μM $CdCl_2$-treated yeast. Figure 3.14b is the Fourier transform of the same data.

Sample	absorber	Shell	N	R	DW
No Cd	Zn	O/N	3.3	2.04	0.006
	Zn	S	2.0	2.33	0.005
High Cd	Zn	O/N	2.4	2.04	0.006
	Zn	S	3.2	2.33	0.005
	Cd	S	4	2.52	0.004

Table 3.2. Fitting results of the cadmium-treated and untreated whole cell yeast EXAFS.

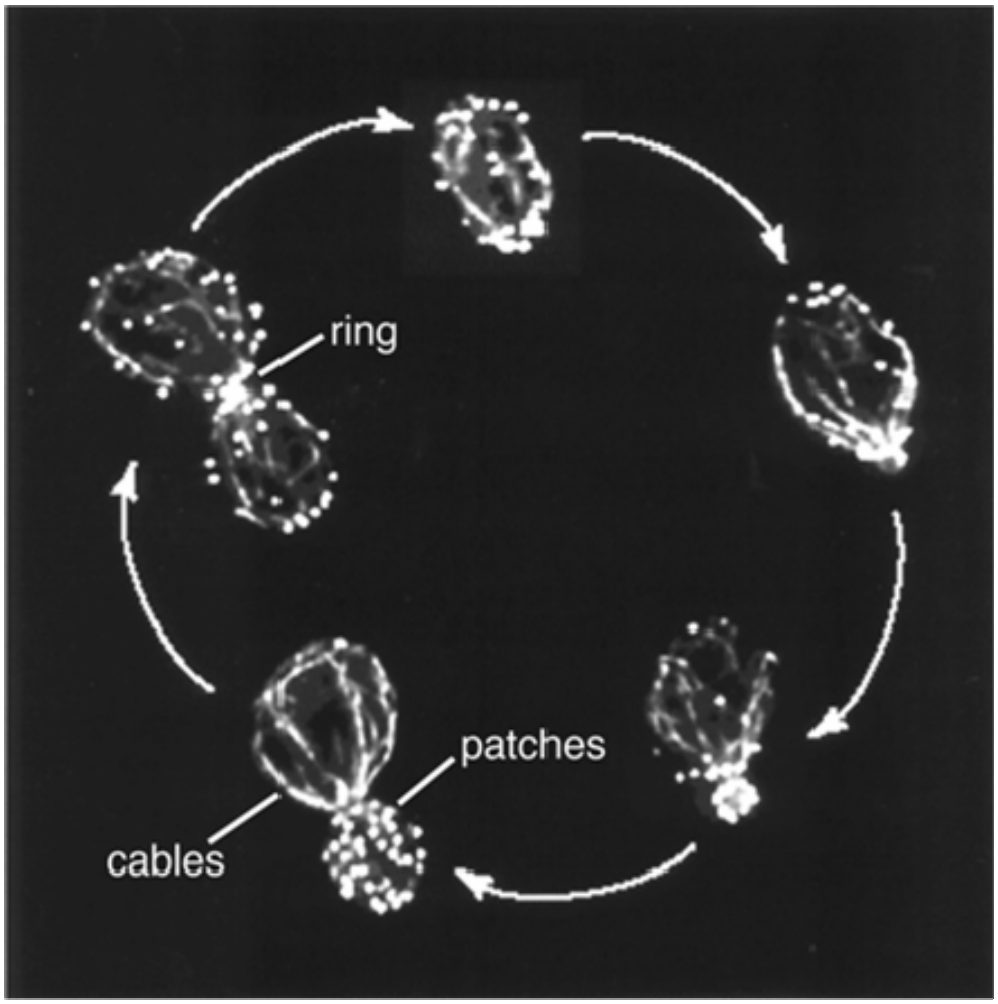

Figure 3.15. Typical distribution of actin cytoskeleton during the yeast cell cycle, as revealed by GFP-labeled actin. Taken from Shi, *et al*, JBC 278, 50309-15 [31].

References

1. Bertin, G., and Averbeck, D. Cadmium: cellular effects, modifications of biomolecules, modulation of DNA repair and genotoxic consequences. Biochimie (2006), 1549-1559.
2. Bernhard, D., Rossman, A., Wick, G. Metals in cigarette smoke. Iubm Life. (2005) 850-809.
3. Chiba, M., Masironi, R. Toxic and trace-elements in tobacco and tobacco-smoke. *Bulletin of the World Health Organization* (1992) 269-275.
4. Inaba, T., Kobayashi, E., Suwazono, Y., Uetani, M., Oishi, M., Nakagawa, H., Nogawa, K. Estimation of cumulative cadmium intake causing Itai-itai disease. *Toxicol Lett.* (2005) 192-201.
5. Jarup, L., Berglund, M., Elinder, C., Nordberg, G., Vahter, M. Health effects of cadmium exposure – a review of literature and a risk estimate. *Scand. J. Work Environ.* (1998) 1-52.
6. Jin, T., Kong, Q., Ye, T., Wu, X., Nordberg, G. Renal dysfunction of cadmium-exposed workers residing in a cadmium-polluted environment. *Biometals* (2004) 513-518.
7. Jin, T., Lu, J., Nordberg, M. Toxicokinetics and biochemistry of cadmium with special emphasis on the role of metallothioneins. *Neurotoxicology* (1998) 19, 529-535.
8. Nagy, Z., Montigny, C., Leverrier, P., Yeh, S., Goffeau, A., Garrigos, M., Falson, P. Role of the yeast ABC transporter Yor1p in cadmium detoxification. *Biochimie* (2006) 88, 1665-1671.
9. Gomes, D., Fragoso, L., Riger, C., Panek, A., Eleutherio, E. Regulation of cadmium uptake by *Saccharomyces cervisiae*. *Bichimica et Biophysica Acta* (2002) 1573, 21-25.
10. Waalkes, M., Poirier, L. In Vidro Cadmium-DNA Interactions: Cooperativity of Cadmium Binding and Competetive Antagonism by Calcium, Magnesium, and Zinc. *Toxicology and Applied Pharmacology* (1984) 75, 539-546.
11. Jin, Y., Clark, A., Slebos, R., Al-Refai, H., Taylor, J., Kunkel, T., Resnick, M., Gordenin, D. Cadmium is a mutagen that acts by inhibiting mismatch repair. *Nature Genetics* (2003) 3, 326-329.
12. Mehra, R., Tarbet, E., Gray, W., Winge, D. Metal-specific synthesis of two metallothioneins and γ-glutamyl peptides in *Candida glabrata*. *Proc. Natl. Acad. Sci.* (1988) 85,8815-8819.
13. Mendoza-Cozatl, D., Devars, S., Loza-Tavera, H., Moreno-Sanches, R. Cadmium accumulation in the chloroplast of *Euglena gracilis*. *Physiol. Plant.* (*2002*) 115, 276-283.
14. Chan, J., Merrifield, M., Soldatov, A., Stillman, M. XAFS Spectral Analysis of the Cadmium Coordination Geometry in Cadmium Thiolate Clusters in Metallothionein. *Inorganic Chemistry* (2005) 44, 4923-4933.
15. Li, Z., Lu, Y., Zen, R., Szczypka, M., Thiele, D., Rea, P. A new pathway for vacuolar cadmium sequestration in *Saccharomyces cervisiae*: YCF1-catalyzed transport of bis(glutathinato) cadmium. *Proc. Natl Acad Sci* (1997) 94, 42-47

16. Vido, K., Spector, D., Lagniel, G., Lopez, S., Toledano, M., Labarre, J. (2001). A Proteome Analysis of the Cadmium Response in *Saccharomyces cerevisiae*. The Jounal of Biological Chemistry, 276, 8469-8474.
17. Penner-Hahn, JE (2005). Characterization of "spectroscopically quiet" metals in biology. Coordination Chemistry Reviews 249, 161-177.
18. George, G.N. Stanford Synchrotron Radiation Laboratory, Menlo Park, CA, 1990.
19. Weng, T.C., Waldo, G.S., and Penner-Hahn, R.E. (2005). A method for normalization of X-ray absorption spectra. Journal of Synchrotron Radiation 12, 506-510.
20. Gladfelter, A.S., Pringle, J.R.,and Lew, D.J. (2001) The septin cortex at the yeast-bud neck. Current Opinion in Microbiology 4, 681-689.
21. Vido, K., Spector, D., Lagniel, G., Lopez, S., Toledano, M., Labarre, J. (2001) A Proteome Analysis of the Cadmium Response in *Saccharomyces cerevisiae*. The Journal of Biological Chemistry 11, 8469-8474.
22. Moseley, J.B., and Goode, B.L. (2006) The Yeast Actin Cytoskeleton: from Cellular Function to Biochemical Mechanism. Microbiology and Molecular Biology Reviews 3, 605-645.
23. Farah, M.E., Amberg, D.C. (2007) Conserved Actin Cysteine Residues Are Oxidative Stress Sensors That Can Regulate Cell Death in Yeast. Molecular Biology of the Cell 18, 1359-1365.
24. Charnock, J.M., Garner, C.D., Abrahams, I.L., Arber, J.M., Hasnain, S.S., Henehan, C. and Vasak, M. (1989), EXAFS Studies of Metallothionein. Physica B 158, 93-94.
25. Haldar, S. (2007). Determination of In Vivo Metal Loading, Distribution, Storage, and Enviornment in Biological Systems: Use of X-ray Synchrotron Light Source. PhD thesis.
26. Casero, E., Martin-Gago, J.A., Pariente, F., and Lorenzo, E. (2004). Metal release in metallothioneins induced by nitric oxide: X-ray absorption spectroscopy study. European Biophysical Journal 33, 726-731.
27. Waters, B.M., and Eide, D.J. (2002). Combinatorial control of yeast FET4 gene expression by iron, zinc and oxygen. Journal of Biological Chemistry 277, 33749-33757.
28. Hassett, R.F., Yuan, D.S., and Kosman, D.J. (1998). Spectral and kinetic properties of the Fet3 protein from Saccharomyces cerevisiae, a multinuclear copper ferroxidase enzyme. Journal of Biological Chemistry 273, 23274-82.
29. Santos, R., Dancis, A., Eide, D., Camadro, J.M., and Lesuisse, E. (2003). Zinc suppresses the iron-accumulation phenotype of Saccharomyces cerevisiae lacking the yeast frataxin homologue (Yfh1). Biochemical Journal 375, 274-254.
30. Wei, J.P., Srinvasan, C., Han, H., Valentine, J.S., and Gralla, E.B. (2001). Evidence for a novel role of copper-zinc superoxide dismutase in zinc metabolism. Journal of Biological Chemistry 276, 44798-44803.
31. Shi, X., Stoj, C., Romeo, A., Kosman, D.J., and Zhu, Z. (2003). Fre1p Cu2+ reduction and Fet3p Cu1+ oxidation modulate copper toxicity in Saccharomyces cerevisiae. Journal of Biological Chemistry 278, 50309-15.
32. Rebbeor, J.F., Connoly, G.C., Dumont, M.E., and Ballator, N. (1998). ATP-dependent Transport of Reduced Glutathione on YCF1, the Yeast Orthologue of

Mammalian Multidrug Resistance Associated Proteins. Journal of Biological Chemistry 275, 33449-33454.
33. Satarug, S. (2001). Changes in zinc and copper homeostasis in human livers and kidneys associated with exposure to environmental cadmium. Human and Experimental Toxicology 4, 205-213.

Chapter 4

X-ray Fluorescence Microscopy of Malaria-infected erythrocytes

Introduction

While malaria has largely been eliminated in wealthy countries, the disease has a tremendous impact on the developing world. Malaria is caused by one of four single-cell parasites of the genus *Plasmodium*, and is spread by the *Anopheles* mosquito; those infected suffer from fever, chills, nausea, and malaise – the disease is debilitating and in severe cases can be deadly. The CDC estimates that malaria is responsible for between one and two million fatalities – most of them children – and 300 million cases of acute illness every year. Malaria kills three times more children in developing countries than HIV/AIDS, and is one of the deadliest childhood diseases in sub-Saharan Africa [1]. The costs of malaria in sub-Saharan Africa account for around 1% of the region's GDP [2], and some argue that malaria is one of the main causes of the long-term economic stagnation in the region [3].

An understanding of the details of the life cycle of malaria is essential for the development of new ways to combat the disease. Subjecting the *Plasmodium* parasite to oxidative stress is one of the ways that both the immune system and many anti-malaria drugs act to combat the parasite [4], and transition metals such as Fe, Cu, and Zn are

critical cofactors in oxidative stress response [5,6]. For example, the commonly-used antimalarial chloroquine and quinine inhibit the detoxification of heme in the parasite, thus increasing the amount of oxidative stress in the parasite. A more complete picture of metal distribution, speciation, and homeostasis in the malaria parasite is therefore important for developing a detailed understanding of the infection of red blood cells by the *Plasmodium* parasite. The malaria parasite has a complex and well-characterized life cycle. Human infection begins with an infected female *anopheles* mosquito biting a human, injecting slender, infectious sporozoites into the bloodstream. These sporozoites invade liver tissue and mature into merozoites (cells roughly 2 microns in diameter), which in turn infect RBCs (biconcave discs 8 microns across). Having invaded the erythrocyte, the merozoite matures into a larger trophozoite, growing to be nearly as large as the host RBC. The trophozoite divides many times to form new merozoites, which rupture the host erythrocyte and infect other erythrocytes. Most merozoites repeat this cycle, while some mature into gametocytes, to be taken up by another anopheles mosquito and perpetuate the cycle outside of the human host [7]. A depiction of the malaria parasite's life is depicted in Scheme 4.1.

While the parasite matures within the red blood cell, it must acquire the nutrients required for growth, including transition metals such as iron, copper, and zinc. Iron metabolism presents a challenge in the malaria parasite due to the high iron content of the host's erythrocytes. Upon infecting an erythrocyte, the parasite's main source of protein is hemoglobin, and the heme released from digestion of hemoglobin is sequestered into the parasite's food vacuole as a hemozoin crystal [12]. The great lengths that the parasite takes to maintain an acceptable level of intracellular iron is not unique to

malaria; it has been shown that infectious bacteria take great effort to import iron from their host, and it is thought that the bacteria's struggle for iron is one of the limiting factors in its growth in human hosts [10-11]. The role of zinc acquisition in infectious diseases, on the other hand, has been less well characterized.

Previous work done on *P. falciparum* has shown that infected red blood cells accumulate zinc as infection progresses, more than doubling the initial zinc concentration of the host red blood cell, and concentrating zinc over the plama concentration of zinc roughly 40-fold [8]. This additional zinc must be actively imported by the parasite, as an erythrocyte has no nucleus and cannot express the machinery to import zinc. It has been shown that *Plasmodium* exports many proteins into the RBC cytoplasm – some of which interact with the RBC membrane – and extends membranous structures into the host RBC that are thought to aid the parasite in acquiring nutrients [9]. It is unclear what purpose the accumulated zinc serves. The rapid growth and replication of the parasite is one possible driving force for the accumulation of zinc – the invading merozoite replicates into 6-20 new meorozoites before rupturing the RBC [7]. Zinc is present in many regulatory zinc-finger proteins that play an important role in transcription; it is reasonable to assume that the production of as many as twenty new nuclei in a short time would require more such regulatory proteins, and thus more zinc. On the other hand, the accumulated zinc may play a role in merozoite invasion of the erythrocyte or evasion of the host's immune system. Spermatozoa are coated in a layer of zinc, and this zinc is proposed to play a role in destabilization of the membrane of the spermatozoa as well as the egg, allowing the sperm to fuse with the egg [13]. The zinc in the malaria parasite might play a similar role in readying the membranes of both the erythrocyte and the

merozoite, allowing the the parasite to enter the soon-to-be host erythrocyte. A third possibility is that the parasite takes up zinc from the blood in excess of its needs in order to suppress the immune system; zinc is essential to the proper function of the immune system [20]. If the malaria parasites are able to sequester enough plasma zinc to cause deficiency in the immune system, then the immune system response to the infection may be less robust, allowing for the more efficient continuation of the parasite's life cycle.

In this work we have measured the elemental content of infected and uninfected erythrocytes using X-ray fluorescence microscopy, and examined the chelatable zinc distribution in infected erythrocytes using zinc-sensitive fluorescent probes. By using these tools, we are able to cast light on certain aspects of the malaria life cycle.

Experimental Procedures

Culture methods. Asexual stages of *P. falciparum* 3D7 strain were cultured and synchronized by standard procedures [14].

Staining infected erythrocytes. *P. falciparum* were stained for bioavailable zinc with a 5 mM stock solution of Zinbo5 in DMSO. Dye was diluted to 15 μM in the malaria culture, which was imaged in the presence of the dye. Nucleic acids were stained with Syto85 (Invitrogen Corporation) at a final dilution of 500 μM. Cells were imaged with a Nikon E600 equipped with a cooled CCD camera (Cool SNAP HQ, Photometrics, Roper Scientific, Inc.). Fluorophores were excited with a mercury bulb. Images were collected with Metamorph software (Universal Imaging, Molecular Devices). With HRP-GFP overexpressing Plasmodia, infected erythrocytes were identified by fluorescence using a DAPI filter set (Chroma 61002m) with excitation at 403 nm and emission at 460 nm. Zinbo7 was excited using 380 nm excitation filters, and cells were imaged with a

465 nm emission filter, thus collecting signal from the zinc-bound probe only. Images were also collected with excitation at 340 nm or emission at 405 nm, settings appropriate for visualizing the apo probe. Signal present with microscope settings for the holo probe disappeared when settings were changed to filters for the apo probe, thus demonstrating that the holo image was not due to apo signal.

X-ray fluorescence microscopy. Schizont-infected erythrocytes were isolated through a Percoll gradient and were mounted on silicon nitride windows (Stilson, Ltd.). A drop of culture was placed on the window and let stand for approximately 10 seconds to allow the cells to settle. Excess cells were washed away by dipping the window in complete media. Cells were fixed by dipping the window in liquid nitrogen followed by washing with acetone chilled to its freezing point. The window was allowed to dry at room temperature. Scanning X-ray fluorescence data was collected on the X-ray Operation and Research beamline 2-ID-E at the Advanced Photon Source, Argonne National Laboratory. The incident beam was focused to a spot size of $0.50 \times 0.40\ \mu m^2$ and rastered across the sample with a step size of $0.4 \times 0.3\ \mu m^2$. The incident X-ray energy was 10 keV, and integration time was typically 2 seconds. X-ray fluorescence from the sample was collected with an energy-resolving germanium detector, and a full MCA trace was recorded for each spectrum. Samples were mounted in a helium-filled chamber in order to reduce absorption of low-energy fluorescent X-rays by the atmosphere. Data were collected at room temperature.

X-ray fluorescence images were processed with MAPS, a software package written by Stefan Vogt [15]. Using the MAPS software package, a region of interest was drawn around each cell; in budding cells separate regions were defined for the mother

cell and the budding cell. Integral XRF spectra were generated and fit using the spectrum for each pixel which was fit with the fitting routine included in the MAPS package. Elements were quantified by comparing the counts at each pixel to the metal levels in NIST X-ray standards 1832 and 1833, which contain a known amount of element per square centimeter.

Results and Discussion

We imaged 17 malaria-infected and 27 uninfected erythrocytes using X-ray fluorescence microscopy. The status of cells was established by examining the XRF micrograph subsequent to imaging; infected cells showed a lacuna in the distribution with iron. It was difficult to determine the infection status of erythrocytes prior to imaging, since Gimsea-staining the cells might cause a perturbation in metal content and localization. The average elemental content of the infected and uninfected erythrocytes is shown in Figure 4.1. The average zinc content of the infected cells increases more than 3-fold, slightly more than the doubling previously reported increase in zinc content [8]. Substantial increases are also shown in phosphorus, sulfur, and potassium. These results make sense given that the erythrocyte is not a typical cell, in that it has no nucleus and limited metabolism, thus it has a lesser need for phosphorus in nucleic acids and ATP, and sulfur in proteins. Iron shows a slight and likely significant ($p=0.06$) increase as well – the iron content of infected cells is 5% higher than in the uninfected erythrocytes. Given that no homologue of heme oxygenase has been identified in *P. falciparum,* this slight increase in iron content could be taken as evidence that the parasite must import its non-heme iron from outside the erythrocyte, in spite of the abundance of heme iron present in the red blood cell. Copper is the only element that shows a decrease in total

content upon infection, suggesting that the parasite actively exports copper that is liberated from metabolism of superoxide dismutase, which is where the bulk of copper is stored in a normal erythrocyte.

Figure 4.2 shows the elemental distribution of both an infected and uninfected erythrocyte. All of the iron images of the infected erythrocytes clearly show the intense localization of iron due to the hemozoin crystal, as well as the far lower concentration of iron in the region of the parasite. This lacuna of iron grows as the parasite expands, and the areas of high zinc and phosphorous were highest in the areas of low iron. Figure 4.3 shows elemental maps of three different erythrocytes in various stages of infection; in each case, the levels of high zinc and phosphorous are limited to the areas of lower iron. Additionally, in infected cells, there was always an area of high zinc – sometimes 3-4 times higher than the surrounding areas – that was located in close proximity to, but not exactly overlapping with, the areas of high iron associated with the hemozoin crystal, suggesting that this iron is stored in a separate compartment than the hemozoin. This distribution is demonstrated in figure 4.4, showing an overlay of iron and zinc concentration in a typical infected red blood cell. Phosphorus and other elements do not show localization within the parasite.

Figure 4.5 shows the total metal content of each cell measured, both infected and uninfected. The zinc shows a substantial increase in all infected cells; furthermore, the infected erythrocytes with lower zinc tend to be those with smaller regions of low iron, indicating parasites in the early stages of infection (either ring stage or early trophozoite). Some of the infected cells at the latest stages of infection show a fivefold increase in zinc; given that even the largest parasites do not fill the entire erythrocyte, this amounts to a

zinc concentration approaching 1 mM. The individual iron content of each infected erythrocyte, on the other hand, is not significantly higher than that of an uninfected cell. It is only in aggregate that the increase in iron becomes apparent. This fact makes it more likely that the increase in iron is significant, since it is not due to a single outlier.

While the XRF microscopy of the erythrocytes gives information on the total zinc distribution in the infected and uninfected cells, it tells us nothing about the localization of free zinc. We used the zinc-sensitive fluorescent probe Zinbo5 to examine the distribution of free and loosely-bound zinc in infected erythrocytes. Figure 4.6 shows typical fluorescence of infected and normal erythrocytes. Zinbo5 fluorescence appears to surround the hemozoin crystal that is seen in the transmitted light microscope image. To better localize this fluorescence, plasmodia were co-stained with nucleic acid dye, Syto-85, which does not require membrane permeabilization and fluoresces distinctly from Zinbo5. Although the fluorescent signals from the two probes occurred in close proximity, the fluorescent patterns differ; the nucleic acid stain appears as spots consistent with staining plasmodia nuclei, while Zinbo5 illuminates the majority of the parasite except for the food vacuole. This seems to imply that this free pool of zinc is not stored in the nucleus of the parasite. Also the fact that there is a lacuna of Zinbo5 fluorescence in the area of the hemozoin-containing vacuole suggests that this free zinc is localized within the cell membrane of the parasite. If the zinc were localized at the cell membrane, then we would not see a difference in the fluorescence in the area of the vacuole. The free zinc fluorescence images in general seems to have the same distribution as the zinc in the XRF images, in that the high zinc areas are generally localized in the area of the parasite. The Zinbo5 fluorescence, however, does not show

the high zinc localization near the hemozoin crystal that the XRF images show. This suggests that this area of zinc localization is not histologically-accessible, but rather tightly bound to protein ligands, or is otherwise inaccessible to zinc-sensing fluorophores.

One explanation of the observed accumulation of zinc in the malaria parasite is simply that this is the zinc that the parasites need to mature and replicate. We measured the average zinc content of an uninfected erythrocyte to be 1.2 (+/-0.05) fg; if the volume of the erythrocyte is assumed to be 75 μm^3 (7 μm diameter, 2.5 μm thickness), this translates into a concentration of 250 μM, which is close to the same level found in a variety of tissue. The average size of the parasite in the infected cells we imaged with XRF microscopy, as measured by the iron lacuna, was 17 μm^2, and the average amount of zinc in these infected erythrocytes was 3.9 (+/-0.3) fg, an increase of 2.7 fg relative to the uninfected cells. The average amount of zinc in the parasite (defined as the volume of the iron lacunae) was 2.2 (+/-0.2) fg, which accounts for the bulk of the increase in the zinc content of the infected erythrocytes. Assuming that the parasites are spherical, the average concentration of the areas of parasitic infection is 430 (+/-40) μM. While higher than the red blood cells, this is a zinc concentration that is typical in many types of eukaryotic cells, perhaps implying that this accumulated zinc may not be as dramatic as the Zinbo5 images may suggest; rather, this zinc accumulation may only be what the growing parasite needs to grow and replicate. Indeed, *in vivo*, addition of zinc chelators to the growth medium causes the parasites to arrest at the late trophozoite stage (Janet Wolford and Tom O'Halloran, Northwestern University, unpublished result).

That is not to suggest that the accumulation of this zinc does not have interesting implications in the asexual cycle of the malaria parasite. A typical plasma zinc

concentration in adult humans is around 12 μM [16], and in severe cases of malaria, parasitaemia – the percentage of red blood cells infected by parasites – can be 10% in severe cases of malaria [7]. Serum constitutes 55% of blood, and there are 5×10^{12} erythrocytes in a typical adult [17]. Assuming 5×10^{11} infected erythrocytes, with an average uptake of iron of 2.7 fg (the amount of iron taken up by infected erythrocytes in this work), the infected red blood cells would have taken up 1.4 mg of zinc from the serum. The average adult has 5 L of blood, and 2.75 L of serum; assuming 12 μM as an average value of serum zinc, there is 2.1 mg of serum zinc available in a typical adult, so up to 60% of the total serum zinc is needed for these parasites to reach maturity. Indeed, this number may be even greater, since the parasites we measured were not synchronized as the parasites *in vivo* are. The most developed parasites measured by XRF had the highest amount of zinc required, with some infected erythrocytes containing up to 6 fg zinc. These parasites are presumably in the shizont stage, preparing to exit the host red blood cell to infect other erythrocytes. Serum zinc levels often drop during periods of infection, and some have hypothesized that this is a result in the body lowering the availability of zinc to the infectious organism in order to limit it's growth [18]. The present work suggests that, at least for malaria infection, this decrease in serum zinc could be a consequence of infection rather than a reaction to it.

The work in this chapter was primarily undertaken in order to examine the relationship between free zinc measured by the Zimbo5 fluorophore and the total zinc distribution that is measured by XRF microscopy. We found that the distributions are identical; both the free and total zinc images showed sizable increases in zinc levels. While this is not a surprising result, this is the first time that free and total zinc levels

have been compared in such a way, and it provides the groundwork for similar future studies contrasting the free metal distribution and the total metal as measured by XRF microscopy. For example, as mentioned in chapter 3, it would be interesting to examine the relationship between free copper levels and the XRF microscopy images of cadmium-treated yeast, in order to see if cadmium treatment does result in an increase in free copper. These sorts of experiments would slowly begin to reveal under what circumstances cells tightly bind transition metals, and under what conditions the metal levels of cells are more loosely bound.

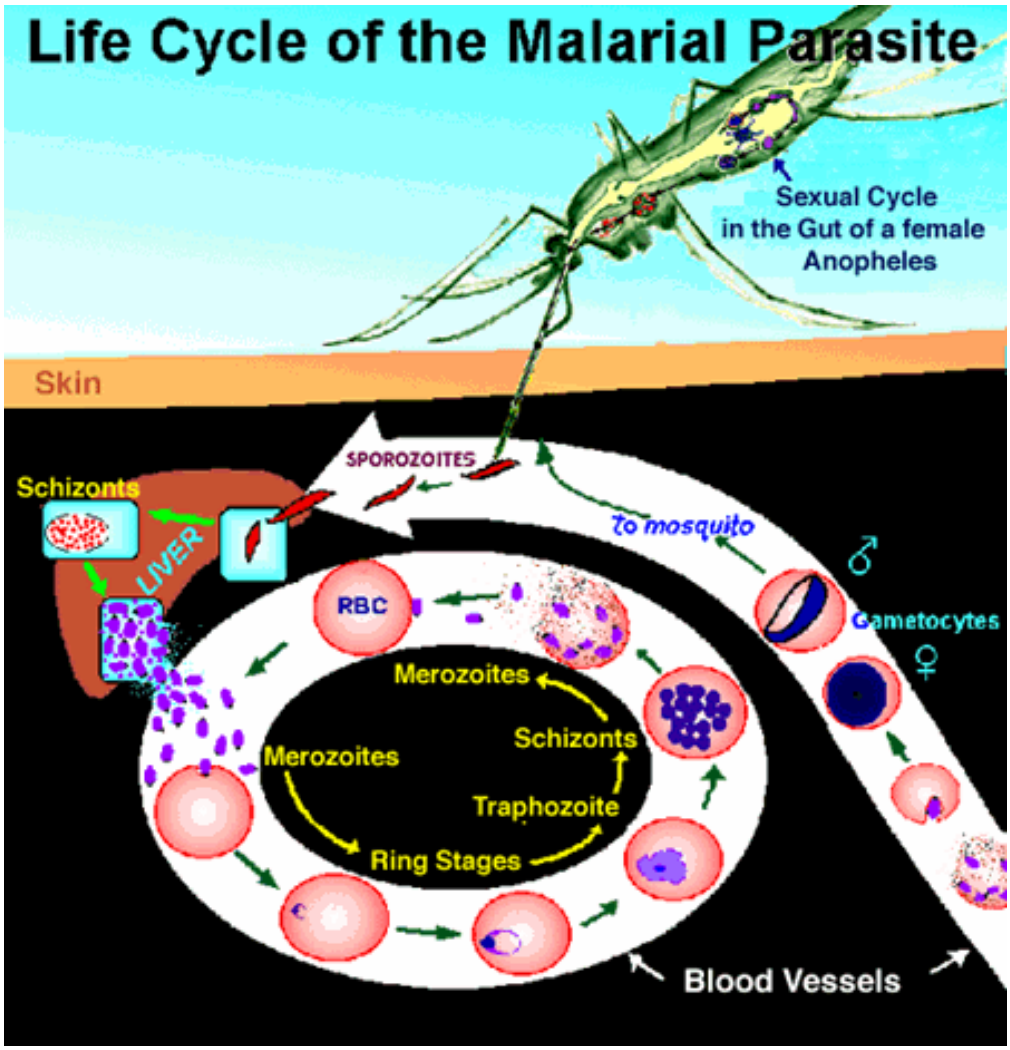

Scheme 4.1. Depiction of the lifecycle of the malaria parasite. Taken from www.cdc.gov/malaria

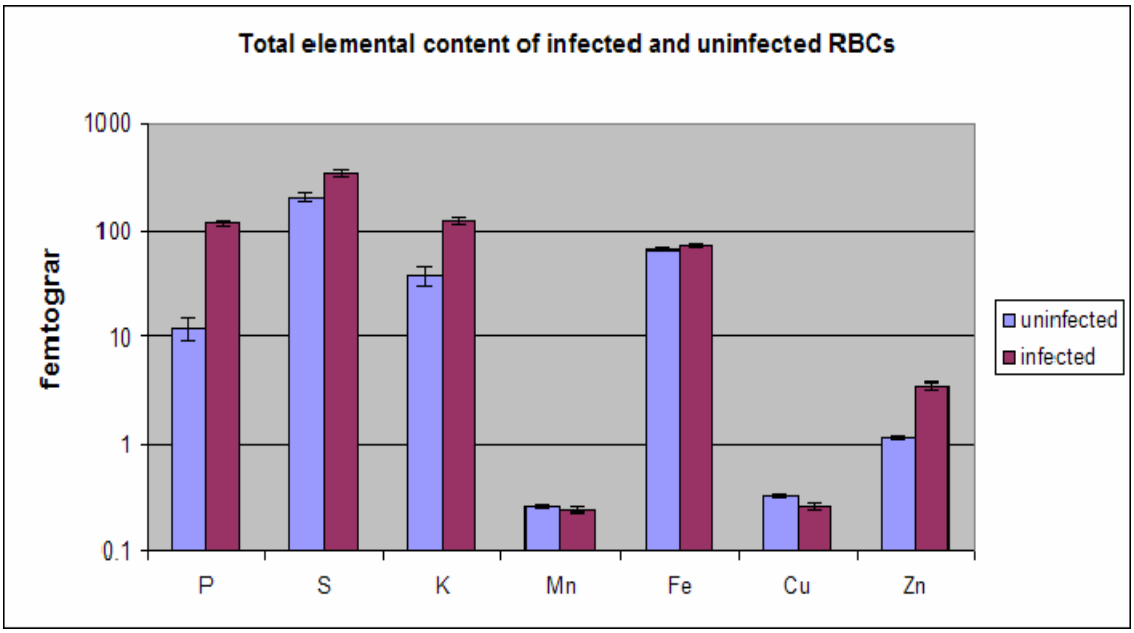

Figure 4.1. Total elemental content in femtograms of infected (n=17) and uninfected (n=27) erythrocytes.

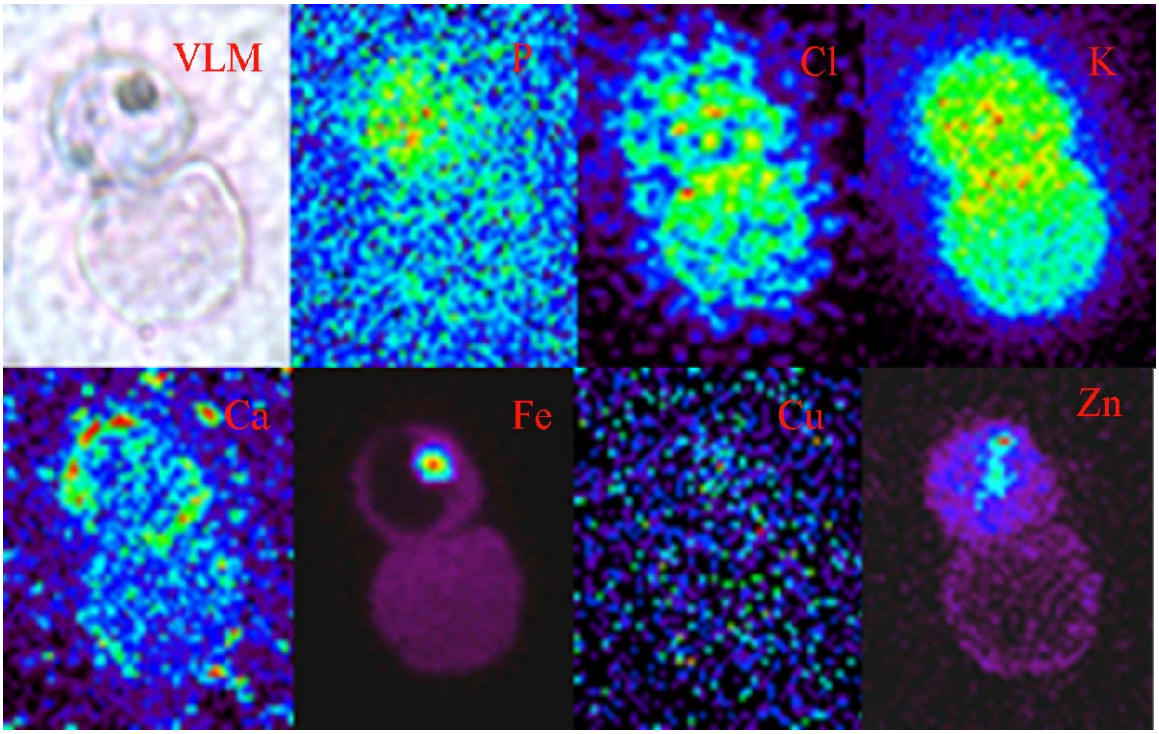

Figure 4.2. False-color XRF images of an infected erythrocyte (top cell) and uninfected cell (bottom cell).

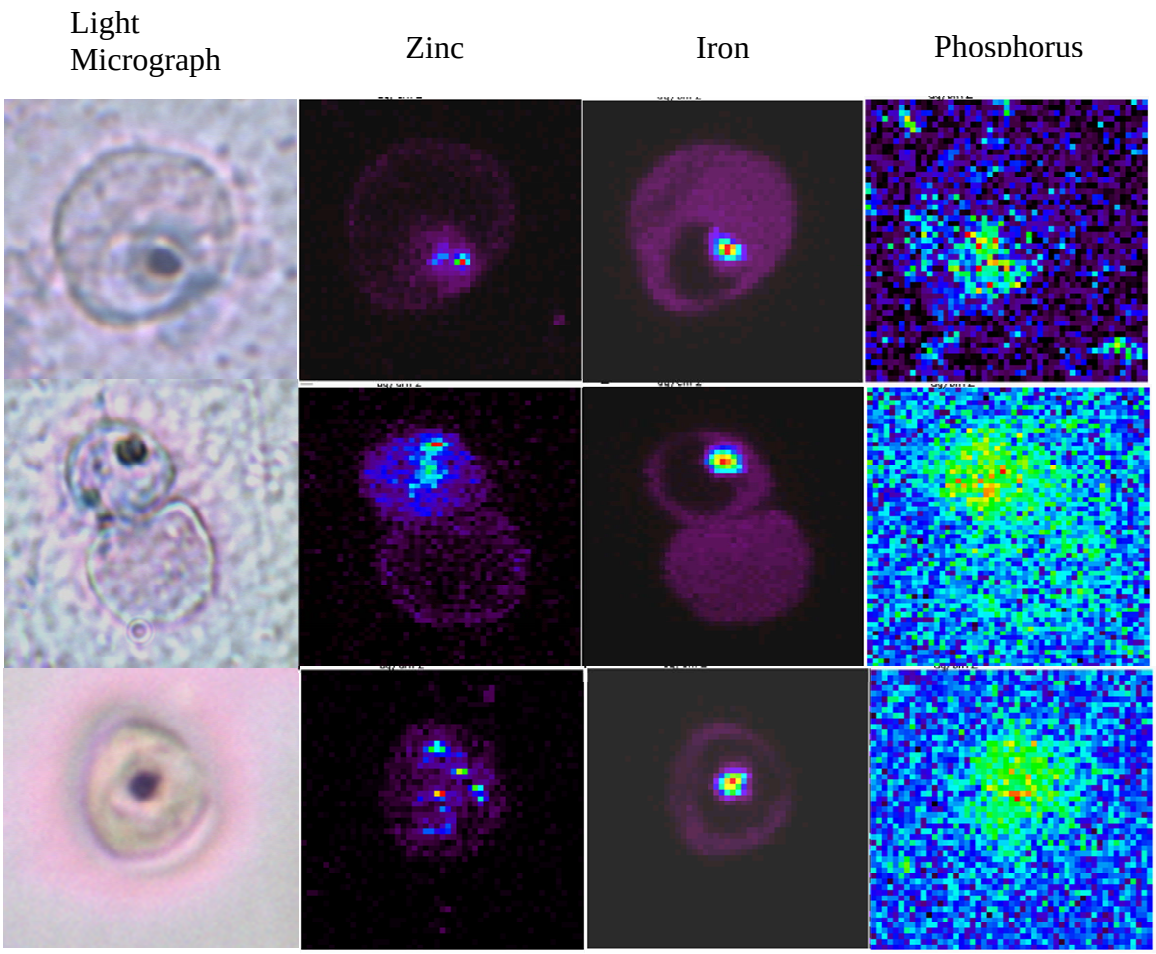

Figure 4.3. Light micrographs (first column), and false-color XRF images of zinc (second column), iron (third column), and phosphorous (fourth column).

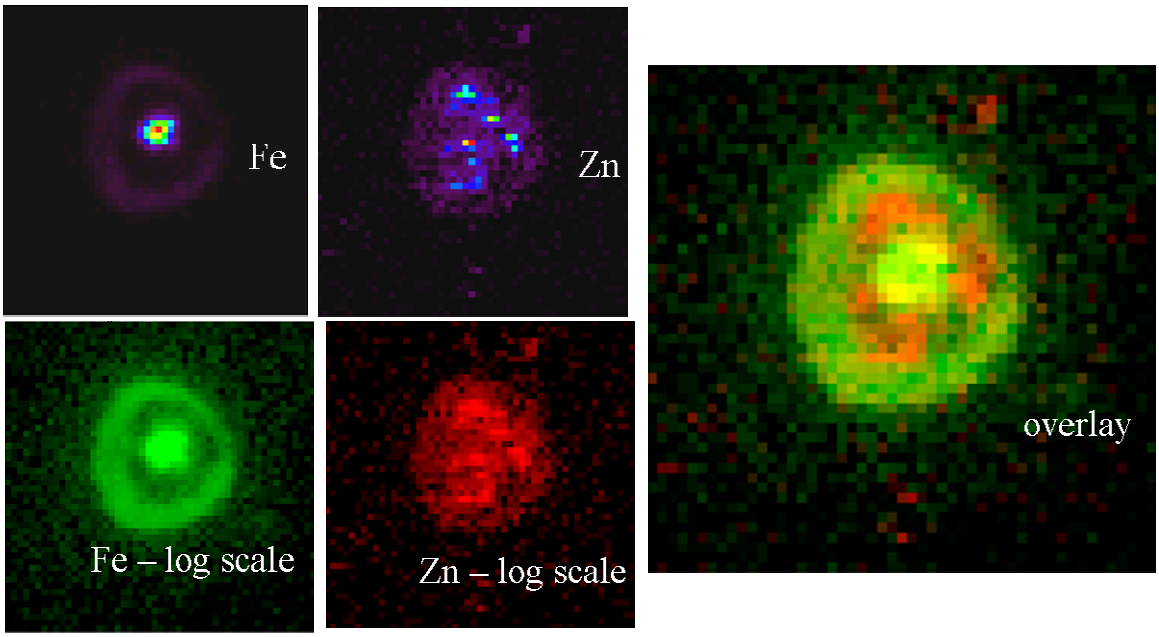

Figure 4.4. False color log scale images of XRF fluorescence in an infected erythrocyte. Typically, the areas of high zinc are close to, but not overlapping with, the high iron of the hemozoin crystal.

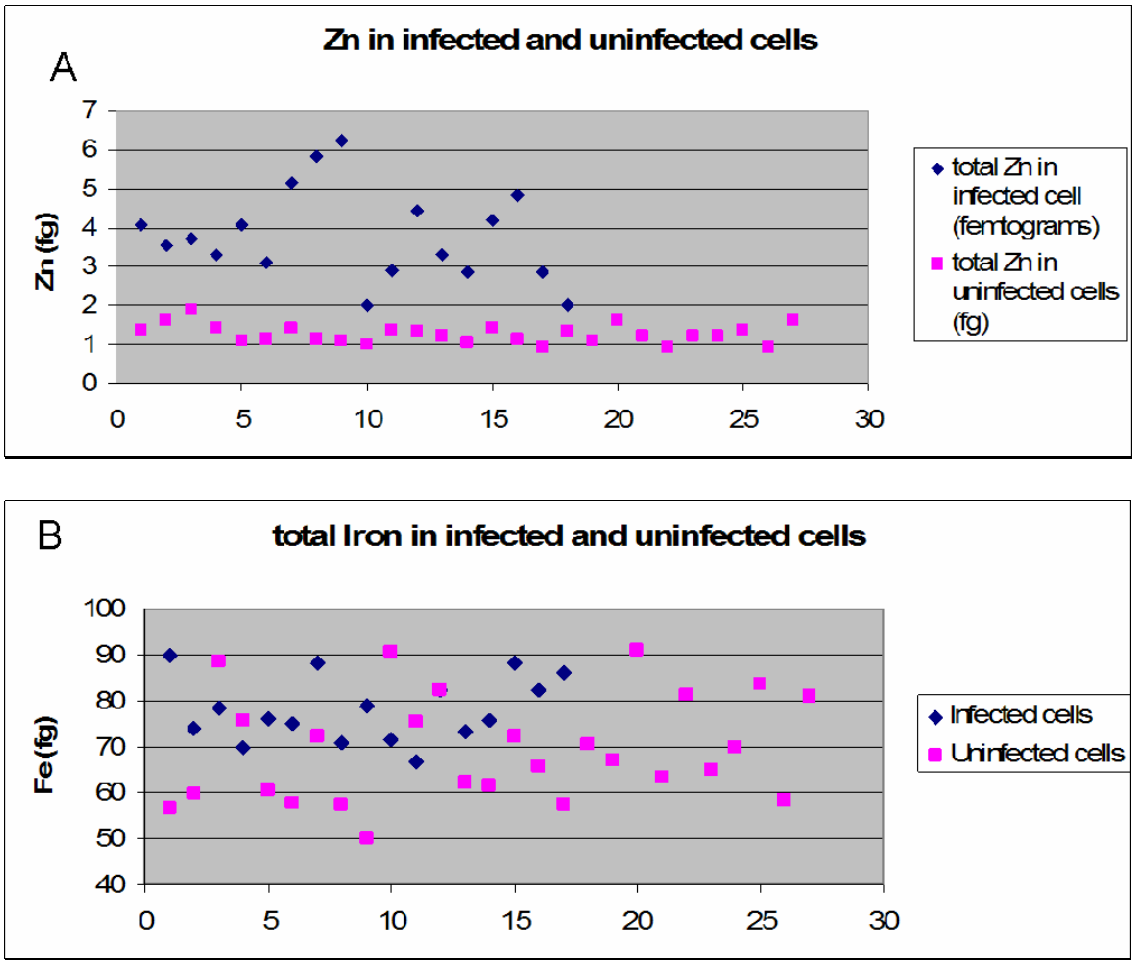

Figure 4.5. Figure 4.5a is the total zinc in infected and uninfected erythrocytes; 4.5b is the total iron in infected and uninfected erythrocytes.

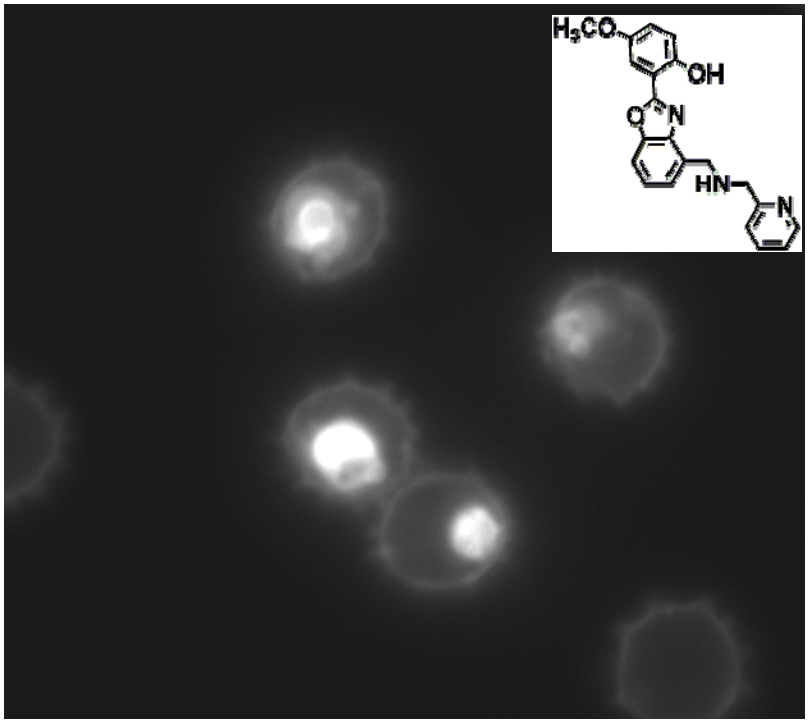

Figure 4.6. Zinbo7 fluorescence of infected erythrocytes. The free zinc is localized to the parasite. The structure of Zinbo7 is shown in the inset.

References

1. Centers for Disease Control website: http\\www.cdc.gov/malaria/
2. Chima, R.I., Goodman, C.A., Mills, A. (2003). The economic impact of malaria in Africa: a critical review of the evidence. Health Policy 63, 17-36.
3. Gallup, JL., Sachs, J.D. (2001). The Economic Burden of Malaria. American Journal of Tropical Medicine 34, 85-96.
4. Becker, K., Tilley, L., Vennerstrom, J.L., Roberts, D., Rogerson, S., Ginsburg, H. (2004). Oxidative stress in malaria-parasite-infected erythrocytes: host-parasite interactions. International Journal for Parasitology 34, 163-189.
5. De Freitas, J., Wintz, H., Kim, J., Poynton, H., Fox, T., Vulpe, C. (2003). Yeast, a model organism for iron and copper metabolism studies. Biometals 16, 185-197.
6. Liochev, S., Fridovich, I., (1999). Superoxide and Iron: Partners in Crime. IUBM Live 48, 157-161.
7. Bogitsh, B., Chen, T. Human Parasitology. (1998). Academic Press.
8. Ginsburg, H., Gorodetsky, R., Krugliak, M. (1986). The status of zinc in malaria (Plasmodium falciparum) infected human red blood cells: stage dependent accumulation, compartmentation and effect of dipicolinate. Biochim Biophys Acta. 886, 337-344.
9. Cooke, B., Mohandas, N., Coppel, R. (2004). Malaria and the Red Blood Cell Membrane. Seminars in Hematology 41, 172-188.
10. Skaar, E.P, Humayun, M., Bae, T., DeBord, K.L., and Schneewind, O. (2004). Iron-Source Preference of *Staphylococcus aureus* Infections. Science 10, 1626-1628.
11. Kemna, E., Pickkers, P., Nemeth, E., vander Hoeven, H., and Swinkels, D. (2005). Time-course analysis of hepcidin, serum iron, and plasma cytokine levels in humans injected with LPS. Blood 106, 1864-1866.
12. Pagola, S., Stephens, P.W., Bohle, D.S., Kosar, A.D., and Madsen, S.K. (2000). The structure of malaria pigment β-haematin. Nature 404, 307-310.
13. Andrews, J.C., Nolan, J.P., Hammerstedt, R.H., Bavister, B.D. (1994). Role of zinc during hamster sperm capacitation. Biology of Reproduction 51, 1238-1247.
14. Trager, W., and Jensen, J.B. (1977). Human Malaria Parasites in Continuous Culture. Science 193, 673-675.
15. Vogt, S. (2004). MAPS: A set of software tools for analysis and visualization of 3D X-ray fluorescence data sets. Journal de Physique IV 104, 635-638.
16. Kazemi-Bajestani, S., Ghayour-Mobarhan, M., Ebrahimi, M., Moohebati, M., Esmaeili, H.A., Parizadeh, M., Aghacizadeh, R., and Ferns, G. (2007). Serum copper and zinc concentrations are lower in Iranian patients with angiographically defined coronary artery disease than in subjects with a normal angiogram. Journal of Trace Elements in Medicine and Biology 21, 22-28.
17. Martini, F. (2006). Human Anatomy, 5th edition. Page 529. San Francisco, Californai: Pearson Education, Inc.
18. Clohessy, P.A., and Golden, B.E. (1995). Calprotectin-Mediated Zinc Chelation as a Biostatic Mechanism in Host Defence. Scandinavian Journal of Immunology 42, 551-556.

19. Solomons, N.W. (1998). Mild human zinc deficiency prduces an imbalance between cell-mediated and humoral immunity. Nutritional Review 56, 27-28.

Chapter 5

X-ray Fluorescence Microscopy of the Hippocampus

Introduction

The brain, like all other tissues, requires zinc for metabolism and normal functions. While it is estimated that 90% or more of the zinc in the brain is in its usual biological role, tightly bound to metalloproteins [1], the remaining pool is unusual in that it appears to be free or loosely bound. It has long been known that staining a cross-section of the hippocampus with the Timm's silver-sulfide stain, a divalent cation-sensitive histochemical stain, reveals pools of free or loosely-bound divalent cation in the brain, particularly in the hilus and CA3 regions of the hippocampus [2]. More recently, it has been shown using zinc-specific fluorescent probes that the identity of this pool of histochemically-accessible divalent cation is zinc [3]. A cross-section of a rat brain stained with Timm's stain is shown in Figure 5.1; the areas of most intense staining are found in the hippocampus.

The hippocampus is important in memory formation – patients who suffer injury to the hippocampus often lose the ability to form new memories [4], and it is often the first area affected by Alzheimer's disease [5]. The hippocampus is comprised of three anatomical divisions: the entorhinal cortex, the dentate gyrus, and the Cornu Ammonis. Memory formation is thought to occur as signals pass through these divisions through

three pathways: the perforant pathway conducts signals from the entorhinal cortex to the granule cells of the dentate gyrus, the mossy fiber pathway connects the granule cells of the dentate gyrus to pyramidal cells of the Cornu Ammonis (CA3), and the Schaffer collateral fiber pathway connects cells in CA3 to the pyramidal cells in CA1 (Figure 5.2) [6]. The histochemically-stainable zinc in the hippocampus is found in the hilus of the dentate gyrus and the stratum lucindum of CA3, specifically within pre-synaptic boutons full of zinc-containing vesicles [7]. The fact that this pool of free or loosely-bound zinc is located in vesicles in pre-synaptic boutons – in the same fashion as other neurotransmitters – suggests a possible role for zinc in the transmission of nerve impulses. Zinc is actively pumped into these vesicles by the zinc transporter ZnT-3, which localizes on the membrane of the zinc-containing vesicles [8]. Rats that have had their ZnT-3 gene knocked out do not have any stainable zinc in their presynaptic vesicles.

While the localization of this free pool of zinc in the brain is well-characterized, the functional role that this zinc plays is not as well understood. While this pool of vesicular zinc seems to always be present in the hippocampus and other parts of the brain, knocking out the ZnT-3 gene in mice is not fatal – in fact, the ZnT-3 knockout mice show no strong phenotype due to the deletion of the gene and the subsequent lack of the vesicular zinc pool [9]. On the other hand, this pool of zinc has been shown to have a role in epilepsy [10], neurogenerative disease, and ischemic injury [5]. Release of the vesicular zinc pool upon ischemia seems to cause neuron damage, and rats that lack the vesicular zinc pool are less prone to epileptic seizures than those with normal levels of vesicular zinc. Given the dangers that seem to be associated with the pool of

histologically-stainable zinc, and that this zinc pool is common among mammals, it seems likely that there is a significant biological role for the pool of vesicular zinc.

In this work, we have directly measured the zinc concentrations in the various regions for the hippocampus with X-ray fluorescence (XRF) microscopy. While others have used histochemical stains and zinc-sensitive fluorescent probes to identify regions rich in free or loosely-bound zinc, XRF microscopy has the advantage of being sensitive to all of the zinc in the sample, not just the loosely-bound pool of zinc. While the vesicular pool of histochemically-acessible zinc has been estimated to be 5-10% of the total zinc pool in the hippocampus [12,13], this pool of zinc has never been measured directly, as XRF microscopy is able to.

Experimental

General. Analysis was performed on transverse brain slices from 50-60 day old male Wistar rats. Halothane-anesthetized rats were perfused through the heart with chilled artificial cerebral spinal fluid (ACSF), thus removing the iron-rich blood from the brain. The brain was removed and sectioned in ice-cold ACSF. ACSF (in mM) 125 NaCl, 25 glucose, 25 $NaHOC_3$, 2.5 KCl, 1.25 NaH_sPO_4, 2 $CaCl_2$, and 1 $MgCl_2$ (pH 7.4, bubbled with 95% O_2-5% CO_2). The brain was mounted at a 60° angle to the horizontal plane, and slices (300 μm thick) were cut using a Vibratome (Leicha Vt 100, Nussloch, Germany).

Epifluorescent microscopy using Zinbo7. Hippocampal slices were taken immediately from the vibratome and placed in fresh ice-cold 4% formaldehyde for 1 hour. Slices were then rinsed with PBS and then stained in 15 μM of Zinbo7 for 20 minutes at room temperature. Samples were rinsed with PBS and imaged on a Nikon

E600 epifluorescent microscope equipped with a cooled CCD camera (CoolSNAP HQ, Photometrics, Roper Scientific, In., Tucson, AZ) and a probe specific filter set (Chroma Technology Corp., Rockingham, VT). The filter set for imaging Zimpo7 included a D365/10x excitation filter and an HQ460/30m emission filters for holo-probe detection.

X-ray fluorescence microscopy. Hippocampal slices from the vibratome were placed in 35°C ACSF bubbled with 95% O_2-5% CO_2 for 45 minutes to recover. Slices were then placed in ice-cold 4% formaldehyde for one hour. Slices were quickly rinsed with ice-cold PBS and mounted between polypropylene film and Kapton tape. PBS and formaldehyde solutions were freshly made, chelex-treated, filtered, and pH-tested prior to use. X-ray fluorescence (XRF) data was collected at beamline 18-ID-D at the Advanced Photon Source, Argonne National Laboratory. The sample was illuminated with a 50×50 μm^2 10 keV X-ray beam focused with Kirkpatrick-Baez mirrors. Fluorescence data was collected using a Si drift detector, and single channel analyzers (SCAs) were set for iron, copper, and zinc. Calibration curves were measured for each element using aqueous solutions of known metal concentration. The cuvettes holding the standards were 2 mm thick, and would therefore absorb a much greater fraction of the fluorescent X-rays. Since the absorption coefficients for both the incident X-rays and the fluorescent X-rays are known, it is a simple matter to calculate how much of the measured signal is due to the first 300 μm of the sample (the thickness of the hippocampus sections), and use that adjusted value for the calibration curve. The XRF data were processed using programs written in MATLAB. Colored images, overlays, and ratio images of zinc and iron signals were created using ImageJ (National Institutes of Health, USA).

X-ray absorption spectroscopy. Hippocampus sections were prepared in the same fashion as described for those prepared for XRF microscopy. Spatially-resolved XAS was measured at beamline 18-ID-D at the Advanced Photon Source, Argonne National Laboratory. An XRF image was measured of the hippocampal section, and XAS were measured at the coordinates that corresponded to the hilus of the dentate gyrus, which was the area of highest zinc concentration. These measurements were taken with using the Kirkpatrick-Baez optics, again using a 50×50 μm^2 beam size. Scans were measured out to k=10, using 0.5 eV steps and 0.1 s dwell times for the entire energy range; 60 scans were averaged. Spectra of a zinc foil were measured using two nitrogen-filled ion chambers placed behind the sample for calibration purposes. Fluorescence was measured using a Si drift detector, and the sample was measured at 25°C. These data were reduced and fit using the GIFEFFIT data analysis program [14], using an E_0 of 9664 eV.

In order to determine if the samples suffered radiation damage that affected the average zinc environment, XAS of frozen samples was measured at beamline 9-3 of the Stanford Synchrotron Radiation Laboratory. Sections of rat hippocampus were prepared as described above. The region of the hippocampus containing the hilus of the dentate gyrus (the area with the highest zinc concentration) was excised and rapidly frozen in liquid nitrogen. Several hili were pooled in one XAS cuvette. For calibration purposes, the EXAFS spectrum of a zinc foil was measured simultaneously by placing the foil downstream of the sample between two nitrogen-filled ion chambers. EXAFS were measured using a step size of 10 eV with 1 second integration time in the pre-edge region, 0.4 eV with 1 second integration time in the edge region, and 0.05 A^{-1} eV steps with k^3-weighted integration times from 1-15 seconds in the EXAFS region. The data

from each detector channel were checked for glitches and the edge energy was calibrated by assigning the first inflection point of the zinc foil as 9659 eV. Bad channels were removed and the data were averaged using the EXAFSPAK suite of programs [15], and the data were background subtracted and normalized [16]. The data were converted to k space using an E_0 of 9664 eV and the data were fitted with the EXAFSPAK suite of programs.

Results and Discussion

Figure 5.2 shows a schematic diagram of the hippocampus, as well as typical fluorescence image of Zinbo7, an analogue of the zinc-specific fluorophore Zinbo5 [17]. Consistent with the literature, Zinbo7 fluorescence illuminates the zinc-enriched mossy fiber boutons of the hilus and the stratum lucidum of the CA3. Figure 5.3 shows the iron and zinc distributions of a typical hippocampus slice as determined by XRF microscopy. As can be seen, the zinc distribution revealed by XRF microscopy is similar to the distribution that is shown with fluorescent probes or Timm's staining. In contrast to the zinc distribution, the highest iron concentrations are found in the cell body layers of both the dentate gyrus and the Ammon's Horn. Overlays of the iron and zinc maps of four different representative hippocampus slices are shown in Figure 5.4. These overlays make clear the striking pattern of the areas of highest iron concentrations in the areas just surrounding the areas rich in histologically-stainable zinc.

Since the highest concentrations of ferritin, the principal iron storage protein in the brain, are found in the hilus and the mossy fiber system [18], and in oligodendrocytes and astrocytes [19], it is somewhat surprising to find the levels of highest iron in the cell layers of the dentate gyrus and Ammon's Horn. However, while iron distributions do not

correlate with those of ferritin, the localizations of mitochondrial proteins show a good correlation with the XRF maps of iron [20,21]. This suggests that the bulk of the iron in the hippocampus is involved in respiration, localized in the active sites of metabolic enzymes in the mitochondria.

The average iron and zinc content of various regions of the hippocampus as measured by XRF microscopy is shown in Figure 5.5. The average zinc concentration of the entire hippocampus was found to be 250 (+/-30) μM, and the average iron concentration was 220 (+/-20) μM. The values for zinc are within the range of literature values for the zinc content of the hippocampus, which range from 136-290 μM [12, 13, 22]. While our iron values are lower than some in the literature [12], this is likely due to the perfusion of the rat prior to dissection, which will remove the iron-rich blood from the rat's brain. In studies that perfused the rat prior to elemental analysis, iron and zinc concentrations are found to be roughly equivalent [13,22], which is consistent with these results.

Using the areas of high zinc as a marker for mossy fibers and high iron concentrations as a marker for cell bodies, the average iron and zinc concentrations for the following areas was determined: the hilus of the dentate gyrus, the suprapyramidal region of CA3, the suprapyramidal region of CA1, and the iron rich granule layer of the dentate gyrus. The concentration of zinc in the hilus was found to be 470 (+/-35) μM, more than double the average of the whole slice. The stratum lucidum of CA3 was found to have lower zinc concentration than the hilus at 330 (+/-20), but still showed a substantial increase of over the rest of the hippocampus. These results show that the histologically-stainable zinc in the hippocampus represents a substantial increase over the

average zinc content of the hippocampus, representing a substantial fraction of hippocampal zinc.

It is thought that the pool of histochemically-accessible zinc can be released upon electrical stimulation, potentially acting as a neurotransmitter [1]. We tested the effects of KCl depolarization on hippocampus sections to see if depolarization has any effect on the bulk distribution of zinc. Figure 5.6 shows the iron and zinc distribution of a hippocampus section depolarized by KCl treatment; as can be seen, the zinc and iron both show distributions identical to those of untreated slices, suggesting that depolarization does not have a significant effect. On the other hand, slices that were treated with KCl showed a 23% decrease in zinc concentration in the hilus compared to adjacent slices (460 (+/-60) for untreated versus 360 (+/-15) for KCl depolarized slices). This result suggests that the histologically-stainable pool of zinc is released and then subsequently taken back up by the cell, but the process is not completely efficient, and some of the zinc is lost to the surrounding buffer.

Figure 5.7 shows the EXAFS and fit of spatially-resolved (beam size $50\times50\mu m^2$) XAS data collected on the hilus of the dentate gyrus of a hippocampus slice. These data are fit with one shell of O/N at 1.96 Å, with a Debye-Waller factor of 0.004 $Å^2$, a coordination number of 4, and a ΔE_0=-4.2. The spatially-resolved EXAFS were measured at room temperature; in order to determine if the sample suffered radiation damage because of this, low temperature EXAFS were done on excised hili from several brain slices. Unfortunately, due to the very small amount of material present in the sample cell, the background signal was large compared to the zinc signal from the sample. The background signal is most likely due to zinc impurities in various metal

components of the cryostat, and is therefore dominated by high-intensity metal-metal interactions. Due to the fact that the contamination is composed of metal-metal interactions, the first – shell which consists of O/N – should not be affected. This is the case, as Figure 5.9 shows that the first shells of the flash-frozen sample and the room temperature micro-EXAFS are in good agreement. The fitting parameters used for the micro-EXAFS also do a good job fitting the first shell of the flash-frozen EXAFS.

The Zn-O distance of 1.96 Å is quite short (while EXAFS cannot distinguish between an oxygen and a nitrogen scatterer, such a short distance is unlikely to come from Zn-N). One interesting aspect of neurons that have pools of vesicular zinc is that these neurons contain vesicular glutamate, and the glutamate and zinc are thought to be compartmentalized together [23]. However, if the zinc were coordinated to the glutamate, one would expect to see a Zn-O distance closer to 2.05 Å [24]. On the other hand, the fitting parameters of EXAFS taken of the zinc imbedded in multilayers of phospholipids are an almost exact match for those reported above [25]. Thus, it seems possible that the zinc is located at the periphery of the vesicles, bound to the phosphate heads of the phospholipids. It should be noted, however, that ligation to glutamate cannot be ruled out.

XRF microscopy has revealed unanticipated variations in metal levels in the hippocampus of rat brain. While the work in this chapter represents a good start in using XRF microscopy to image bulk tissue samples, some improvements should be made doing similar work in the future. Thinner samples of tissue might be used, which would improve the resolution of the images and allow for more precise determinations of metal localizations. Additionally, electrical stimulation of hippocampus sections may be

valuable in determining if and how zinc localization changes upon depolarization of the synapses.

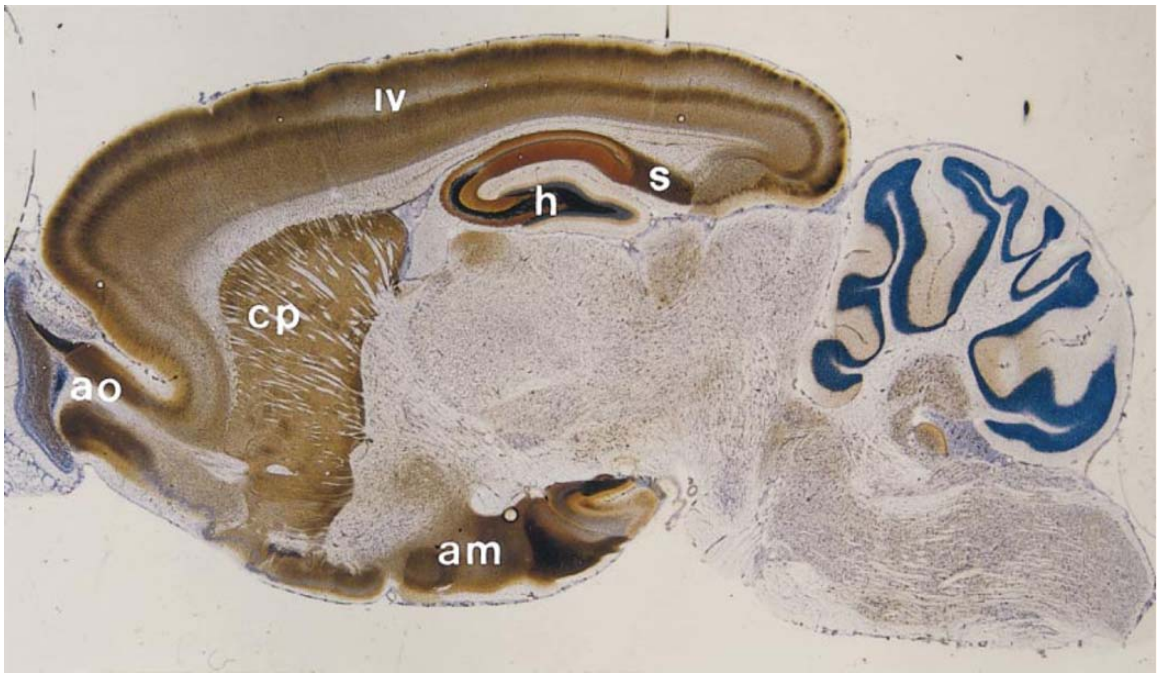

Figure 5.1. Cross section of a rat brain stained with Timm's silver sulfide stain. Taken from Fredrickson *et al* [1].

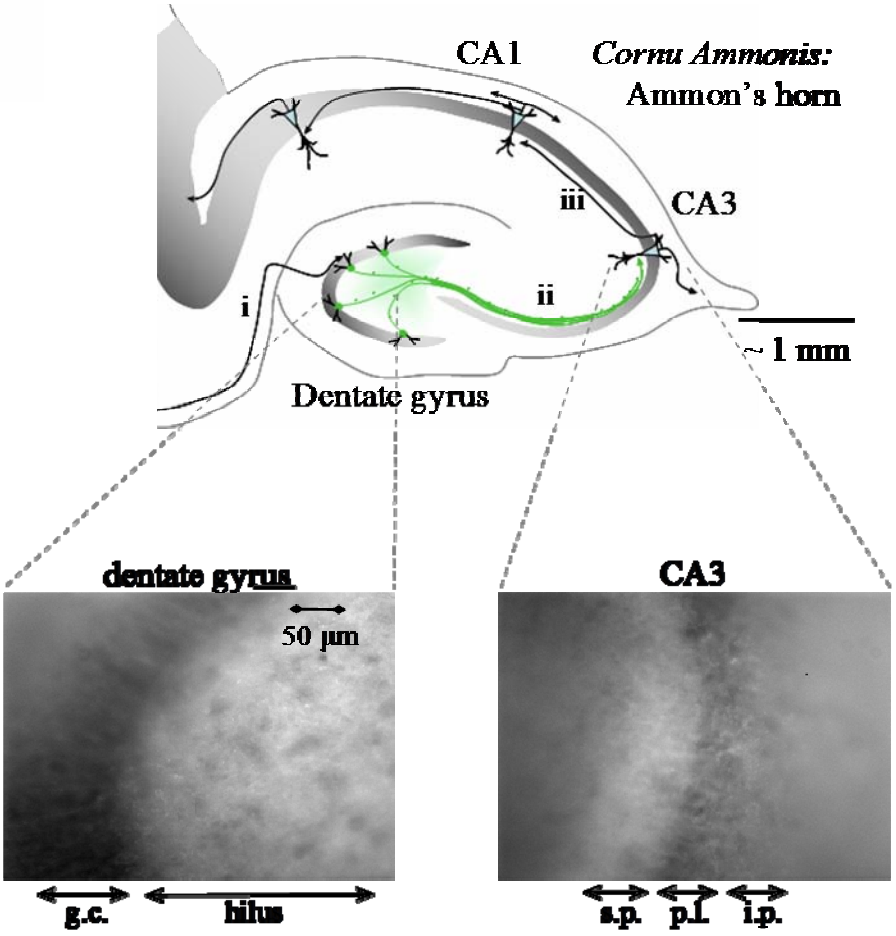

Figure 5.2. Schematic of hippocampus. The insets show Zinbo7 fluorescence of regions of high zinc in the dentate gyrus and CA3 region of the hippocampus. These data were measured by Janet Wolford, Northwestern University.

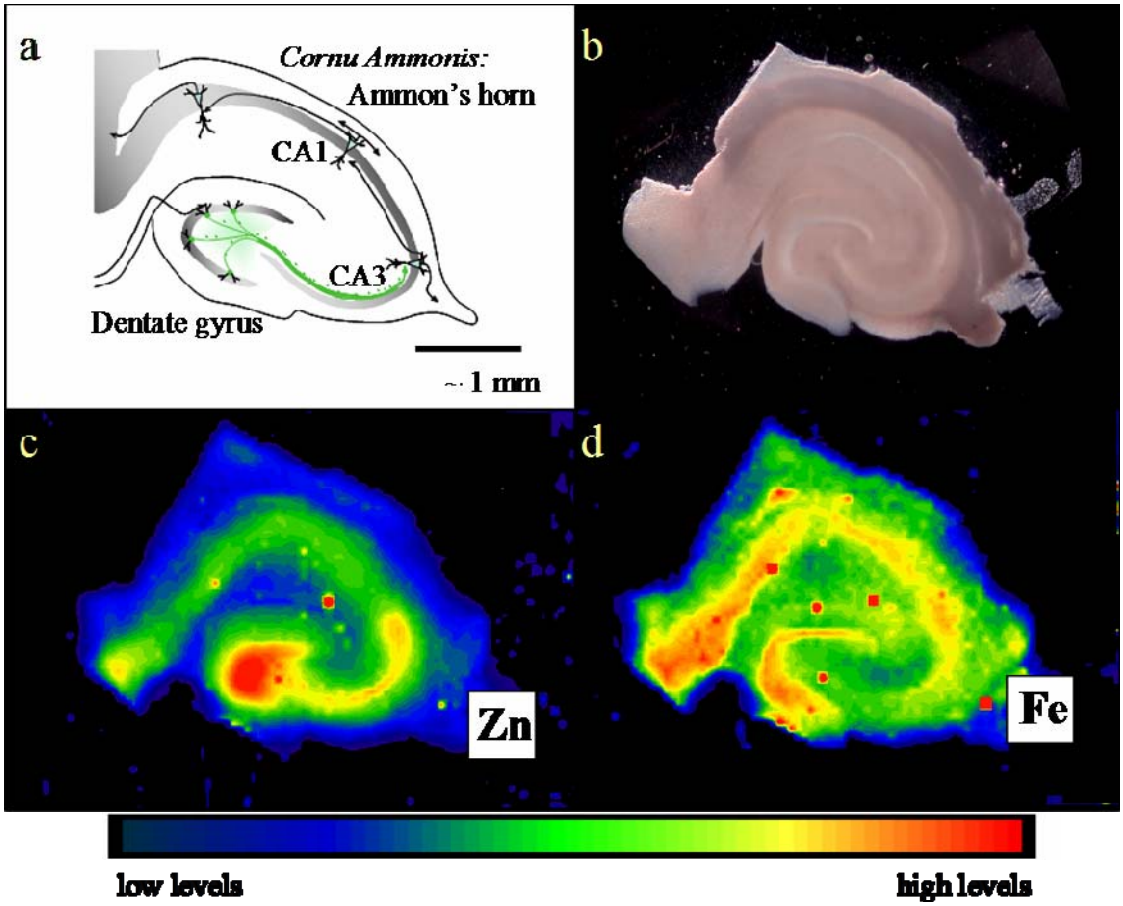

Figure 5.3. Figure 5.3a is a schematic of the hippocampus, 5.3b is a photograph of a rat hippocampus slice, and 5.3c is the zinc XRF image, and 5.4d is the iron XRF image.

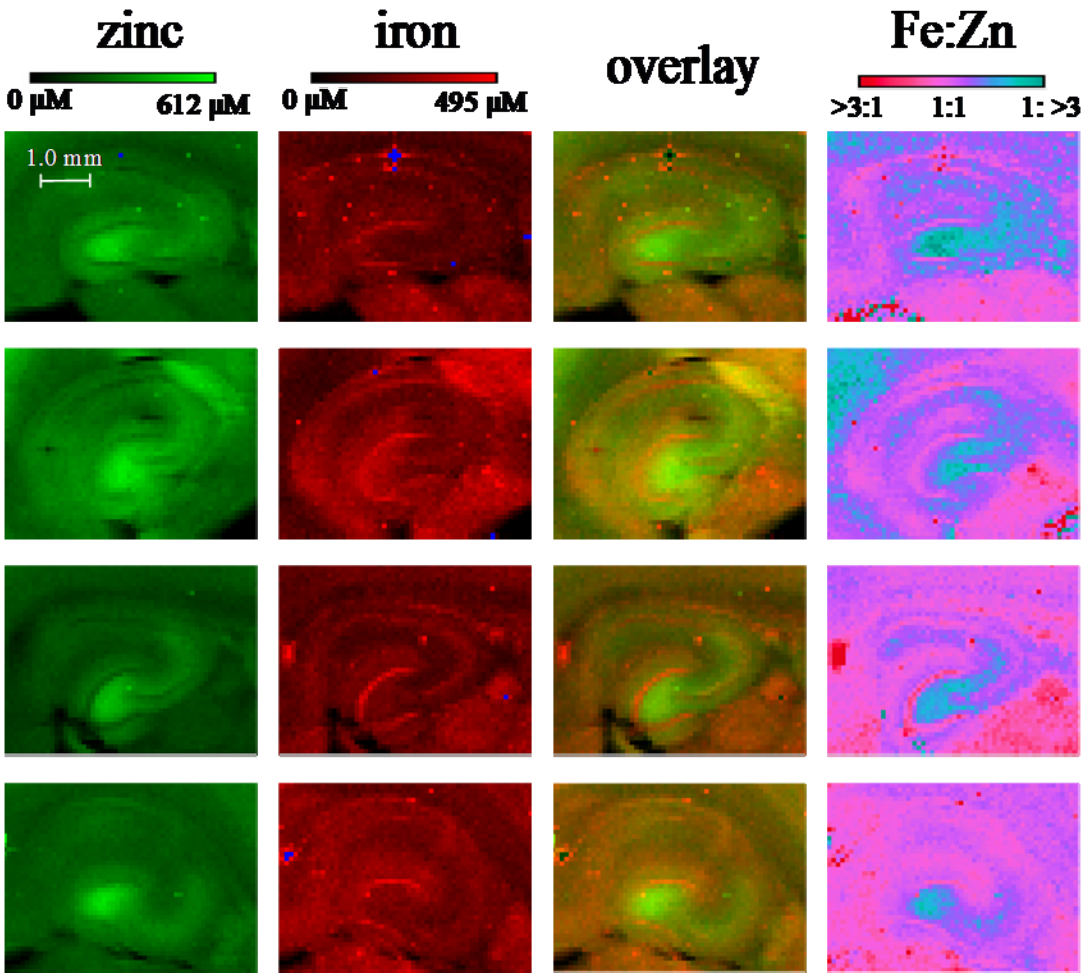

Figure 5.4. The first two columns are of zinc and iron, and the third is an overlay of the two. The fourth column is a ratio of iron to zinc, rather than an overlay. More red corresponds to more iron, while more green corresponds to an excess of zinc.

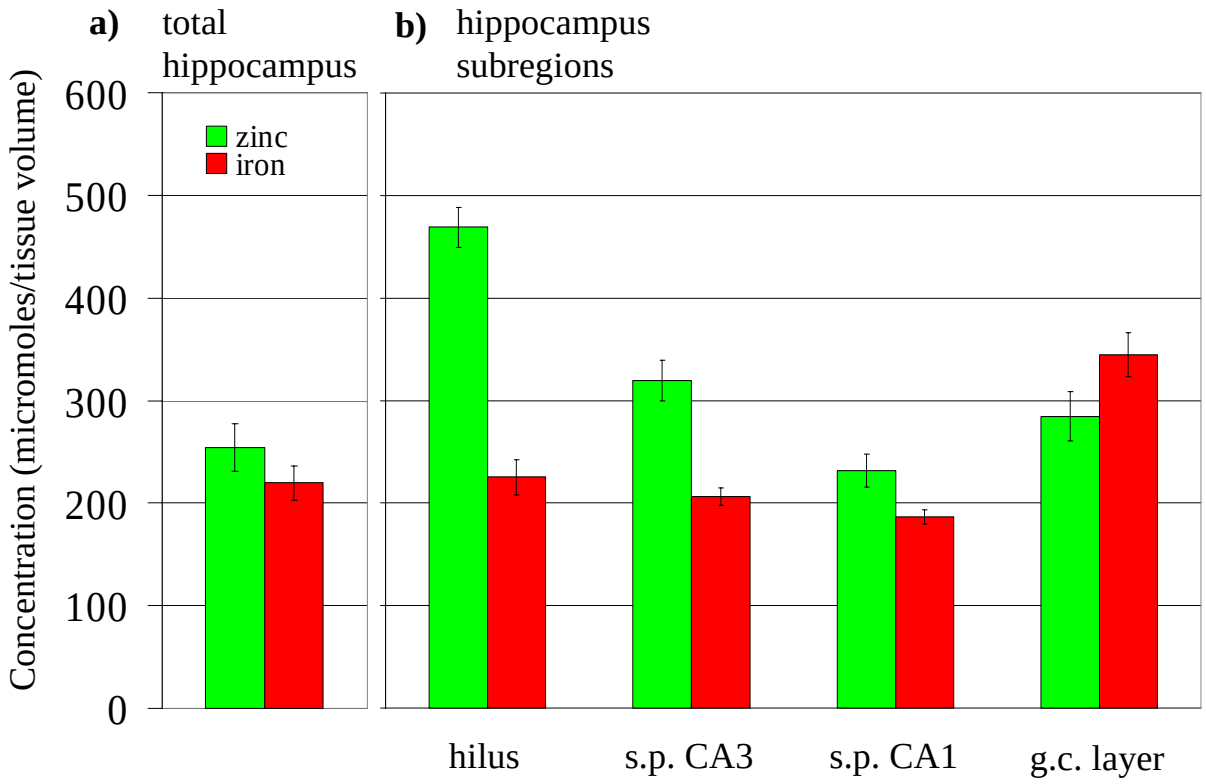

Figure 5.5. Figure 5.5a is the average iron and zinc concentrations of the entire hippocampus, and Figure 5.5b shows the subregions of the hilus, the suprapyramidal region of CA3, the suprapyramidal region of CA1, and the granule cells of the dentate gyrus. The error bars represent the statistical uncertainty in the mean of the 5 slices measured.

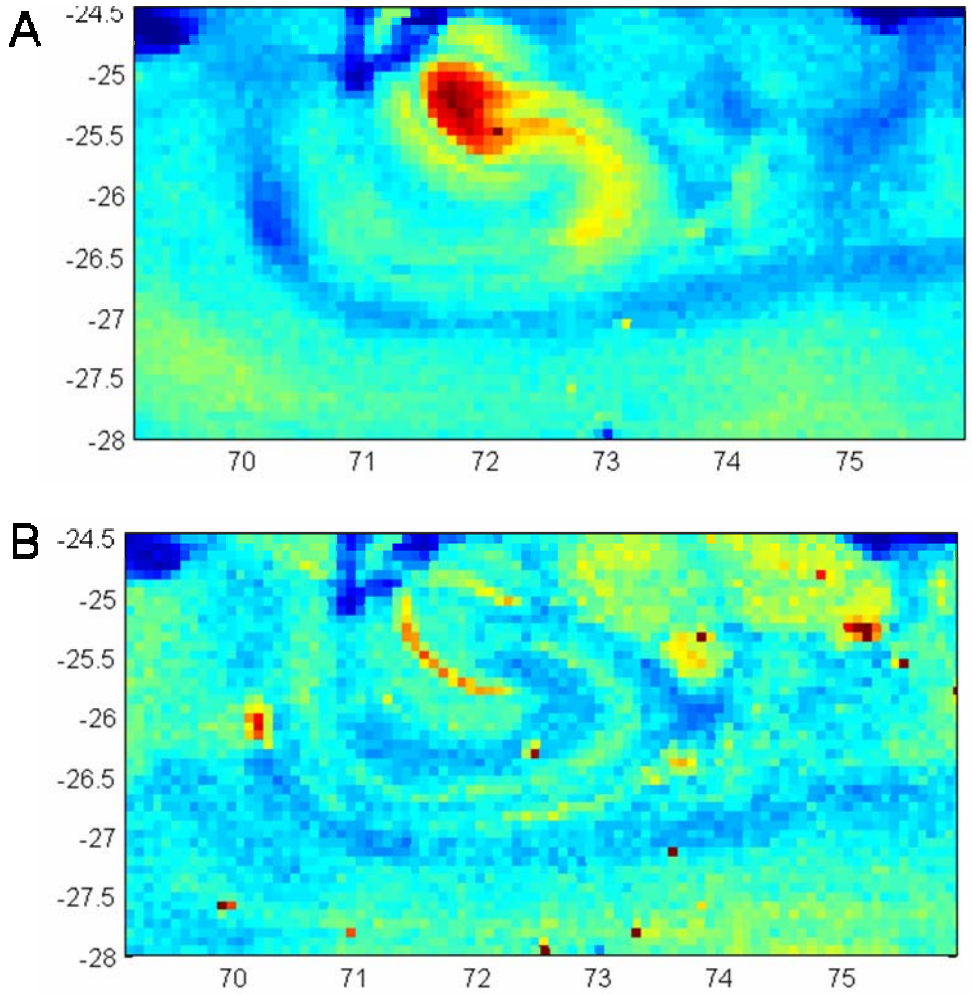

Figure 5.6. Figure 5.6a shows the zinc distribution in a hippocampus slice treated with KCl, and figure 5.6b shows the distribution of iron in the same slice.

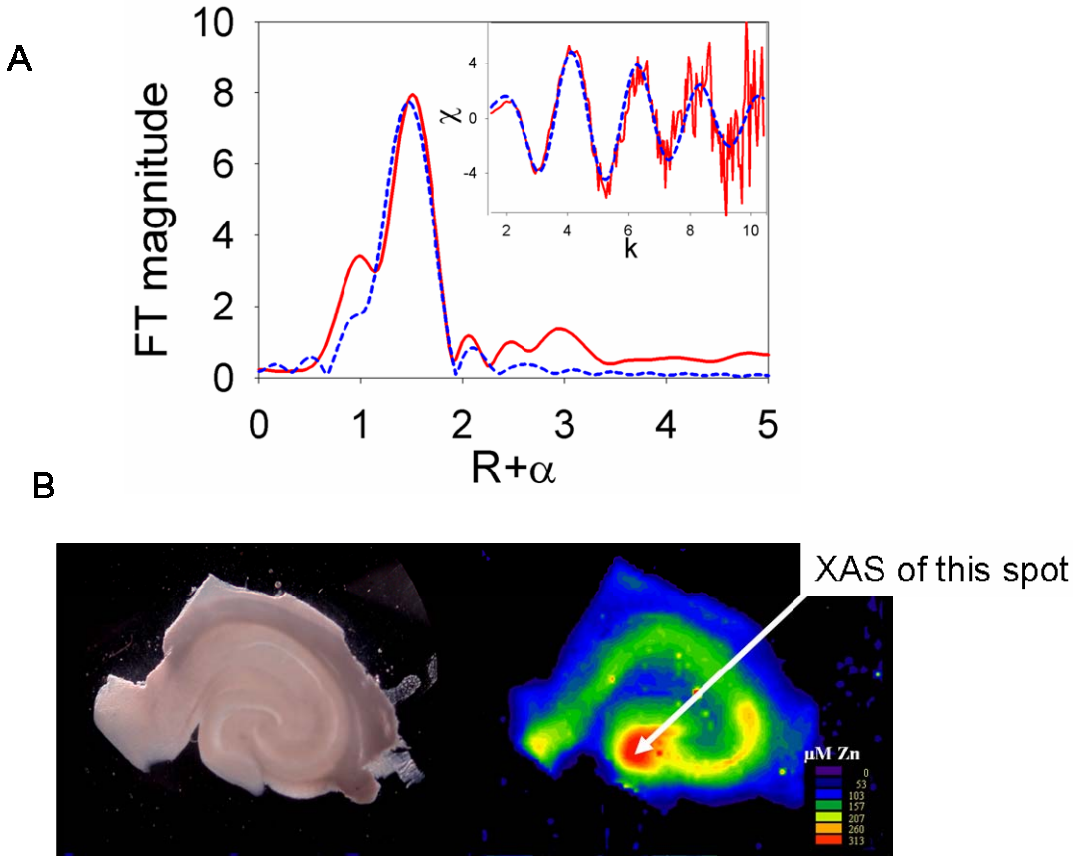

Figure 5.7. Figure 5.7a shows the spatially-resolved zinc EXAFS taken at the hilus of the hippocampus slice depicted in figure 5.7b.

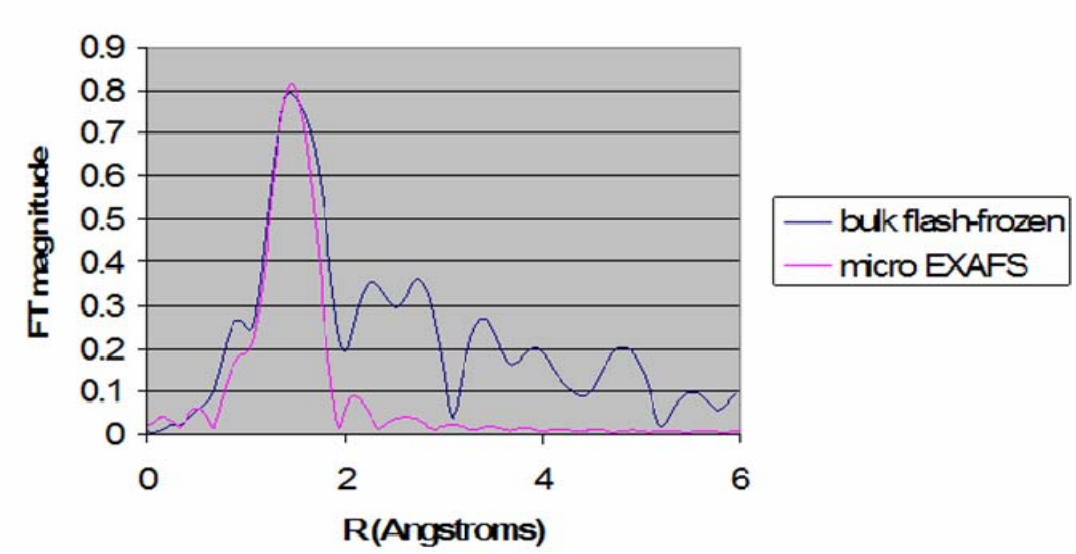

Figure 5.8. Overlay of bulk flash-frozen and spatially-resolved micro EXAFS. While the flash-frozen sample suffers from cryostat contamination, the first shell is consistent with the micro EXAFS of the hilus shown in Figure 5.7.

References

1. Frederickson, C.J. (1989) Neurobiology of zinc and zinc-containing neurons. International Review of Neurobiology 31, 145-238.
2. Timm, F (1958) Zur Histochemie des Ammomshorngebietes. Zeitschrift fur Zellforschung Und Mikroskopische Anatomie 48, 548-555.
3. Fredrickson, C.J., Kasarskis, E.J., Ringo, D., and Fredrickson, R.E (1987) A quinoline fluorescence method for visualizing and assaying the histochemically reactive zinc (bouton zinc) in the brain. J. Neurosci. Methods 20, 91-103.
4. Scoville, W., and Milner, B. (1957) Loss of recent Memory after Bilateral Hippocampal Lesions. Journal of Neurology, Neurosurgery and Psychiatry 20, 11-21.
5. Choi, D.W., and Koh, J.Y. (1998) Zinc and Brain Injury. Annual Review of Neuroscience 21, 347-375.
6. Rolls, E.T., and Kesner, R.P. (2006) A computational theory of hippocampal function, and empirical tests of the theory. Progress in Neurobiology 1, 1-48.
7. Franco-Pons, N., Casanovas-Aguilar, C., Arroyo, S., Rumia, J., Perez-Clausell, J., Dansher, G. (2000) Zinc-rich synaptic boutons in human temporal cortex biopsies. Neuroscience 98, 429-435.
8. Palmiter, R.D., Cole, T.B., Quaife, C.F., Findley, S.D. (1996) ZnT-3, a putative transporter of zinc into synaptic vesicles. Proceeds of the National Academy of Sciences 93, 14934-14939.
9. Cole, T.B., Martyanova, A., Palmiter, R.D. (2001) Removing zinc from synaptic vesicles does not impair spatial learning, memory, or sensorimotor functions in the mouse. Brain Research 891, 253-265.
10. Flynn, C., Brown, C.E., Glasso, S.L., McIntyre, D.C., Teskey, G.C., Dyck, R.H. (2007) Zincergic innervation of the forebrain distinguishes epilepsy-prone from epilepsy-resistant rat strains. Neuroscience 144, 1409-1414.
11. Adlard, P.A., and Bush, A.I. (2006) Metals and Alzheimer's disease. Journal of Alzheimer's Disease 10, 145-163.
12. Frederickson, C.J., Klitenick, M.A., Manton, W.I., and Kirkpatrick, J.B. (1983) Cytoarchitectonic distribution of zinc in the hippocampus of man and the rat. Brain Research 273, 335-339.
13. Wensink, J. and Lenglet, W.J. (1987) The effect of dietary zinc-deficiency on the mossy fiber zinc content of the rat hippocampus – a microbeam PIXE study. Histochemistry 87, 65-69.
14. Newville, M. (2001) IFEFFIT: interactive XAFS analysis and FEFF fitting. Journal of Synchrotron Radiation 8, 322-324.
15. George, G.N. Stanford Synchrotron Radiation Laboratory, Menlo Park, CA, 1990.
16. Weng, T.C, Waldo, G.S., and Penner-Hahn, J.E. (2005). A method for normalization of X-ray absorption spectra. Journal of Synchrotron Radiation 12, 506-510.
17. Taki, M., Wolford, J.L, and O'Halloran, T.V. (2004). Emission ratiometric imaging of intracellular zinc: Design of a benzoxazole fluorescent sensor and it's

application in two-photon microscopy. Journal of the American Chemical Society 126, 712-713.
18. Shoham, S., and Youdim, M. (2002). The effects of iron deficiency and iron and zinc supplementation on rat hippocampus ferritin. Journal of Neural Transmission 109, 1241-1256.
19. Connor, J.R., Menzies, S.L., St Martin, S.M. and Mufson, E.J. (1990). Cellular Distribution of Transferrin, Ferritin, and iron in normal and aged brains. Journal of Neuroscience Research 27, 595-611.
20. Manczak, M., Jung, Y., Park, B.S., Partovi, D., and Reddy, P.H. (2005). Time-course of mitochondrial gene expression in mice brains: implications for mitochondrial dysfunction, oxidative damage, and cytochrome c in aging. Journal of Neurochemistry 92, 494-504.
21. Pettus, E.H., Betarbet, R., Cottrell, B., Wallace, D.C., Madyastha, V., and Greenamyre, J.T. (2000) . Immunocytochemical characterization of the mitochondrially encoded ND1 subunit of complex I (NADH: uniquinone oxireductase) in rat brain. Journal of Neurochemistry 75, 383-392.
22. Kemp, K. and Danscher, G. (1979). Multi-element analysis of the rat hippocampus by prton-induced X-ray emission spectroscopy (phosphorous, sulfur, chlorine, potassium, calcium, iron, zinc, copper, lead, bromine, and rubidium.) Histochemistry 59, 167-176.
23. Wenzel, H.J., Cole, T.B., Born, D.E., Schwartzkroin, P.A., and Palmiter, R.D. (1997). Ultrastructural localization of zinc transporter-3 (ZnT-3) to synaptic vesicle membranes within mossy fiber boutons in the hippocampus of mouse and monkey. Proceedings of the National Academey of Sciences of the United States of America 94, 12676-12681.
24. Grammaccioli, C.M. (1966). Cystal Structure of Zinc Glutamate Dihydrate. Acta Crystallographica 21, 600.
25. Nuzzo, S., Meneghini, C., Mobilioo, S., Hass, H., Riccio, P., Fasano, A., Cavatorta, P., and Morante, S. (2002). An X-ray absorption spectroscopy study of the zinc environment in Langmuir-Blodgett phospholipids multilayers. Biophysical Journal 83, 3507-3512.

Chapter 6

Conclusions and Future Directions

The purpose of this chapter is to discuss the broad conclusions that can be drawn from the previous chapters, as well as to discuss other works that might be undertaken in the future that are logical continuations of this work. There are two separate, but related, directions in which work can proceed. First, XRF microscopy can continue be used to examine the distributions of single cells, in order to determine what sort elemental localizations and distributions can be expected in a cell under a certain type of condition. The second direction is to use XRF in a more high-throughput application in order to determine the distributions of entire populations of cells.

In chapter two of this work, we developed a method where we were able to determine the relative positions of the vacuole and nucleus of a yeast cell, and then image the same cell and determine the distribution of elements using XRF microscopy. In this manner, we were able to determine which elements localized to which compartment. For example, we made the surprising discovery that iron tended to localize to the nucleus of the cell, as well as to the vacuole. In the future, similar studies might be done on other organelles, or on different organisms, or both. In this work, we were unable to determine which elements localize to the mitochondria, because we were not able to visually i

dentify the mitochondria in the light micrographs. Stains similar to those used to identify the vacuole and nucleus are available, and in the future, one might be able to determine how elements localize to the mitochondria under certain conditions. This would help provide a more complete picture of how the cell regulates and makes use of metals.

In Chapter 3, we examined yeast cells treated with cadmium, and observed a drastic change in the localizations of copper, with a fraction of the cell's copper relocalizing to either the bud or the bud neck of the dividing yeast. This result could inspire several different future experiments. Firstly, one could use copper-sensing fluorphores to examine the distribution of free copper in a cadmium-treated cell, and then compare those data with the XRF microscopy data measured in Chapter 3. This experiment would show how tightly the copper in the cell is, and if the copper localized to the bud neck is tightly or loosely bound – if the localizations determined by copper-sensing fluorphore is similar to those shown in the XRF data, one could conclude that cadmium is in fact increasing concentration of free copper in the cell; this result would go a long way in explaining the mechanism by which cadmium causes cellular damage. Another experiment that might be useful is to continue examining yeast and other organisms under varying conditions, and see how the localizations of elements to different compartments change.

More specifically, there are several experiments that could be done to continue with the work discussed in Chapter 3, where we examined the cellular effects of cadmium poisoning on yeast. Similar toxicity studies might be done on other toxic xenobiotic heavy metals such as lead, mercury, gold, or arsenic, and also on toxic does of biologically important metals like copper, iron, or zinc. If these metals cause cellular

damage by a similar mechanism as cadmium, one would expect to see similar copper relocalization in cells treated with these metals. These similarities and differences between the effects of different toxic metals would provide important insight into how these metals cause cellular damage, and would help develop insight into what sorts of treatments might be most effective to combat heavy metal poisoning in humans.

The second area in which more study might be warranted is the development of a more high-throughput means of determining the total elemental content of single cells. As mentioned in Chapter 2, it might be possible to develop a flow-cytometer device to use in conjunction with an XRF microprobe, and thus be able to rapidly measure both the elemental content of cells, as well as measuring the intensity of some fluorophore associated with the cell. In this matter, we could measure the size of the cell, the amount of DNA, and other properties of the cell. Flow cytometers generally measure cells very rapidly, often measuring thousands of cells every second. Of course, with this rapid of a flow rate, it would be impossible to quantify the elemental composition of each cell, as analysis by XRF would take a minimum of 5 seconds. So, in order to couple a flow cytometer-like device with an XRF microprobe, the flow rate would have to be slowed down significantly. Careful consideration will have to be given to determining what sort of material should be used for the X-ray window, where the cell will be illuminated by the X-ray beam. The most difficult aspect of designing this device will be minimizing scatter and maximizing repeatability of the measurement.

While it will be difficult to design an instrument that will measure the XRF signal of a constantly-flowing stream of live cells, such an engineering task may be unnecessary. It might be easier to use a flow cytometer to count, sort, and measure

properties of cells, then drop the cells at predetermined spots on a thin, X-ray transparent surface, such as a silicon nitride window, which is the same surface that cells were mounted on for XRF microscopy measurement in this work. So, with the cells dropped in specific spots of the silicon nitride surface, we will then be able to rapidly measure each cell, provided that a mechanism is fabricated to mount and translate the silicon nitride wafer in a highly reproducible manner. If the tolerances for both the placement of cells, and then the movement of the mounted slide are small enough, this would be a very fast method for determining the total elemental content of a population of cells. This would, for the first time, allow for the determination of the distributions of populations of cells, which could provide valuable insight into how single cell organisms regulate the concentrations of essential elements.